POLITECNICO DI TORINO

SCUOLA DI DOTTORATO
Dottorato in Dispositivi Elettronici – XXVIII° Ciclo

Tesi di Dottorato

Smart Devices and Systems for Wearable Applications

Matteo Stoppa

Tutore
Prof. Fabrizio Candido Pirri

Co-Tutore
Prof. Danilo Demarchi
Prof. David Andrew Green

Coordinatore del corso di dottorato
Prof. Giovanni Ghione

Marzo 2016

Acknowledgements

This Thesis is not only the result of work at the keyboard, but it also encloses the most important milestones of these last few years.

Ever since the first period of my PhD programme, I faced the scientific challenges with passion and dedication, collecting the results in this Thesis, however, without a number of people, to whom I am greatly indebted, it might not have been written at all.

To Professor David Andrew Green, co-supervisor of this/Thesis dissertation, mentor and source of inspiration for my current and future experiences. Thanks to him, I had the chance to tackle new challenges within an international professional group with the precious scientific support of the ESA's Medical Projects and Technology Team Lead, Jonathan Scott, coupled with the smart skills of the KCL technicians Tony Christopher and Lindsey Marjoram. I cannot forget two great KCL researchers, Julia Attias and Phil Carvil, who were able to convey passion in their pioneering activities and share this feeling with other people. Working with them, I enjoyed every aspect of my work. Within the same context, I would also like to thank my office mates/colleagues, Dana Maki, Melanie Fleming and Julie Bieles, with whom I shared thoughts, activities and cold beers. Finally, of this great group, my gratitude goes to the King's College CHAPS Director, Professor Steve Harridge, who has made my participation on the course possible in the first place.

Thanks go to the Istituto Italiano di Tecnologia and Politecnico di Torino for the academic support, the technical facilities and for the confidence that they showed in me.

To my crazy and brilliant PhD friends and colleagues, Giuseppe Airò Farulla, Francesco Brundu, Luigi Colangelo and Pierlugi Freni. Together, we spent many unforgettable moments inside and outside of the Politecnico, as proved by our successful international expedition to the final European PhD competition in the Netherlands (ESA Headquarters).

For Pierluigi, I would like to say something more. Thanks to him, I have had the amazing chance to discover a parallel working environment in which the world of scientific research meets the world of competitive entrepreneurship. Together, we have learnt how to get involved in national and international contexts, showing our hard work,perseverance and dedication, with a touch of madness. I am pleased to present in part of this dissertation the most important results that we achieved, which would not have been reached without Pierluigi.These results are not the end of our journey together, and this is the most important thing.

To my best friend Stefano, who, despite the distance, international experiences and different pathways, is always ready to help me to face new challenges and overcome engaging issues. A bond of friendship and admiration for twenty years that has always given me strength.

To my parents, who have always supported me with patience and wisdom, encouraging me to overcome the hardest situations.

Lastly, to my soulmate and girlfriend, Silvia. I cannot consider this thesis without her and her constant support. She helped me to believe in myself and taught me how to tackle the hardest challenges in the right way. Thanks to her precious/wise advice I was able to survive my PhD experience, and I will be eternally grateful for her patience and trust in me.

Contents

List of Figures

List of Tables

List of Abbreviations

ADC	Analog to Digital Converters
AOA	Angle-Of-Arrival
ARED	Advanced Resistive Exercise Device
AST	Active Smart Textiles
ASTP	Apollo-Soyuz Test Project
BER	Bit-Error Rate
BLE	Bluetooth Low Energy
BMD	Bone Mineral Density
BPSK	Binary Phase Shift Keying
CADET	CApture Deorbiting Target
CEVIS	Cycle Ergometer with Vibration Isolation and Stabilization
CPC	Conductive Polymer Composites
CR	Cognitive Radio
CT	Computed Tomography
CVI	Chronic Venous Insufficiency
DE	Dielectric Elastomers
EAP	ElectroActive Polymer
ECG	ElectroCardioGram
EMG	Electromyogram
ESA	European Space Agency
EVA	External Vehicular Activities
FCC	Federal Communications Commission
FM	Frequency Modulation
FP	Framework Programs
FSR	Force-Sensing Resistor
F-to-F	Face-to-Face
GLCS	Gravity Loading Countermeasure Skinsuit
GPIO	General Purpose Input/Output
GUI	Graphic User Interface
HBF	Hyper-Buoyancy Flotation
IC	Integrated Circuit
ICP	Intrinsically Conductive Polymer
IoT	Internet of Things
IPMC	Ionic Polymer-Metal Composite
IR-UWB	Impulse Radio - UltraWide Band
ISS	International Space Station
IVA	Intra Vehicular Activities
KCL	King's College London
LDO	Low-DropOut
LEO	Low Earth Orbit
Li-Po	Lithium-Polymer
LM	Load Monitoring
LOS	Line-Of-Sight

LVDS	Low-Voltage Differential Signaling
MCU	Micro Controller Unit
MEMS	Micro-Electro-Mechanical Systems
MIT	Massachusetts Institute of Technology
MRI	Magnetic Resonance Imaging
MW-CNT	Multi-Walled Carbon Nanotube
NASA	National Aeronautics and Space Administration
NLOS	Non Line-Of-Sight
OOK	On-Off Keying
PAM	Pulse Amplitude Modulation
PAN	Personal Area Network
PCB	Printed Circuit Board
PER	Pulses Per Second
PFM	Pulse Frequency Modulation
PPM	Pulse Position Modulation
PRF	Pulse Repetition Frequency
PSD	Power Spectral Density
PST	Passive Smart Textiles
PTF	Polymer Thick Film
PVDF	PolyVinyliDene Fluoride
QFN	Quad Flat No-leads
RFID	Radio-Frequency IDentification
RMIT	Royal Melbourne Institute of Technology
RO	Ring Oscillator
ROC	Read-Out Circuit
RSSI	Received Signal Strength Indicator
SEM	Spinal Elongation Monitoring
SM	Stretch Monitoring
SNR	Signal-Noise Ratio
SoA	State-Of-the-Art
SS	Signal-Strength
TDoA	Time Difference of Arrival
THD	Total Harmonic Distortion
TOF	Time-of-Flight
ULP	Ultra-Low Power
USB	Universal Serial Bus
UST	Ultra Smart Textiles
VCO	Voltage Controlled Oscillator
WBAN	Wireless Body Area Network
WLAN	Wireless Local Area Network

Abstract

Doctor of Philosophy

Smart Devices and Systems for Wearable Applications

by Matteo Stoppa

Wearable technologies need a smooth and unobtrusive integration of electronics and smart materials into textiles. The integration of sensors, actuators and computing technologies able to sense, react and adapt to external stimuli, is the expression of a new generation of wearable devices. The vision of wearable computing describes a system made by embedded, low power and wireless electronics coupled with smart and reliable sensors - as an integrated part of textile structure or directly in contact with the human body. Therefore, such system must maintain its sensing capabilities under the demand of normal clothing or textile substrate, which can impose severe mechanical deformation to the underlying garment/substrate. The objective of this thesis is to introduce a novel technological contribution for the next generation of wearable devices adopting a multidisciplinary approach in which knowledge of circuit design with Ultra-Wide Band and Bluetooth Low Energy technology, realization of smart piezoresistive / piezocapacitive and electro-active material, electro-mechanical characterization, design of read-out circuits and system integration find a fundamental and necessary synergy. The context and the results presented in this thesis follow an "applications driven" method in terms of wearable technology. A proof of concept has been designed and developed for each addressed issue. The solutions proposed are aimed to demonstrate the integration of a touch/-pressure sensor into a fabric for space debris detection (CApture DEorbiting Target project), the effectiveness of the Ultra-Wide Band technology as an ultra-low power data transmission option compared with well known Bluetooth (IR-UWB data transmission project) and to solve issues concerning human proximity estimation (IR-UWB Face-to-Face Interaction and Proximity Sensor), wearable actuator for medical applications (EAPtics project) and aerospace physiology countermeasure (Gravity Loading Countermeasure Skinsuit project).

To Silvia

Chapter 1

Introduction

It is spread opinion today that in order to provide people with personalized healthcare, support, and information, technological advances should be brought closer to the subject by means of easy-to-use wearable interfaces between devices and humans (De Rossi, Della Santa, and Mazzoldi, 1999). This can be achieved through multifunctional fabrics, commonly referred to as electronic textiles (e-textiles) or smart textiles (these terms will be interchangeable in this paper), capable of making daily life healthier, safer, and more comfortable (Binkley, 2003; De Rossi et al., 2003; Lorwongtragool et al., 2014; Robson et al., 2016; Page, 2015). Smart textiles can be mainly described as textile materials that "think for themselves", for example through the incorporation of electronic devices or smart materials (Stoppa 2014). Such fabrics are conceived as innovative and high knowledge content garments, integrating sensing, actuation, electronic, and power functions (De Rossi et al., 2002; Hui et al., 2006; Khan et al., 2013; Majidi, 2014).

According to their functional activity (Stoppa and Chiolerio, 2014), smart textiles can be classified in three different categories:

- **I° generation** ⇒ able to sense the environment/user, based on sensors (Passive Smart Textiles, PST);
- **II° generation** ⇒ reactive sensing to stimuli from the environment, integrating an actuator function and a sensing device (Active Smart Textiles, AST). The actuators act upon the detected signal either directly or from a central control unit;
- **III° generation** ⇒ able to sense, react and adapt their behaviour to the given circumstances (Ultra Smart Textiles, UST).

The Ultra Smart Textiles is the cutting edge frontier of the innovation in this field. Through a successful marriage of the textile technology with other branches of science like materials science, structural mechanics, biology, sensor and actuator technologies, etc. Due to their multifunctional interactivity, enabled by wearable devices that are flexible and conformable to the human body, e-textiles are considered relevant promoters of a higher quality of life (Park and Jayaraman, 2003) and progress in biomedicine, as well as in several health-focused disciplines, such as biomonitoring, rehabilitation, telemedicine, teleassistance, ergonomics, and sport medicine (Najafi, Armstrong, and Mohler, 2013; Warach et al., 2015; Patel et al., 2012; Shishoo, 2005; Bonato, 2005).

The new frontier of the wearable technology refers to a textile structure which embeds electronics and physically behaving as a textile, at the same time. In general, the development of electronic textiles supports the idea of wearable computing, or electronic devices into garment designs (Van Langenhove, 2007).

Wearable technologies aim to solve challenges in several fields such as medical, sport, and artistic communities, the military and aerospace. The early European Commission's 6th and 7th Framework Programs (FP) provided significant research and development funding for personal health monitoring through smart wearable systems and for projects targeting the integration of sensors, energy sources, processing, and communication integrated within a fabric. Table 1.1 lists the projects funded by the European Commission's 6th and 7th Framework programs that have focused on smart fabrics and interactive textiles.

Moving beyond the bio-signal sensing, several type of sensors based on textiles can be used for others purposes, such as: temperature sensing (Laukhina et al., 2014) hosting conductive fibers into a fabric that responds to a temperature variation; biophotonic sensing (Tao et al., 2012) using luminescent elements integrated within a normal fabric; sensing movements (Grillet et al., 2008) or strain events using shape-sensitive fabrics; gas detection (Windmiller and Wang, 2013) adopting fibers able to change their electrical properties when a particular chemical agent is presented near the sensor.

Sensors provide a nervous system to detect signals, thus in a passive smart material, the existence of sensors is essential. The actuators act upon the detected signal either autonomously or from a central control unit; together with the sensors, they are the essential element for active smart materials. Sensors and actuators used in textiles can be electrically powered and controlled by power and electronic devices advantageously embedded in the fabrics. The integration of active electronic components would enable the implementation of closed-loop controls of the system.

1.1 Challenges and Research Objectives

The next generation of wearable devices will include the following components:

- smart sensors able to detect body and environmental parameters;
- low power, miniaturized and performing electronics able to collect and rapidly process data;
- "soft" and wearable actuators able to generate a physical feedback;
- data and power interconnections embedded within a textile structure;
- ultra low power and reliable wireless communication systems able to stream data with nearby receivers;
- compact power supply of the overall system;
- fully and seamless integration of different technologies.

The objective of this thesis is to introduce a novel technological contribution for the next generation of wearable devices. Several challenges have to be addressed in the field of materials science, electronics and system integration.

Taking into account the different technological areas, the main objectives of this research work are presented as follows:

- CHAPTER 2 → to design, develop and characterize a sensorized belt with a fully integrated pressure-touch sensors for aerospace application. A low-power, reliable and integrated read-out circuit coupled with a custom piezo-capacitive polymeric material has been designed, tested and integrated within a fabric;
- CHAPTER 3 → to design, develop and characterize an ultra-low power wireless data communication system for short-range application based on Impulse Radio - UltraWide Band (IR-UWB). The objective is to demonstrate the effectiveness in terms of reliability, power consumption and signal quality of the IR-UWB technology compared with well known Bluetooth, technology widely used by the wearable devices;
- CHAPTER 4 → to design, develop and characterize an ultra-low power proximity sensor based on IR-UWB technology for medical application. The objective is to evaluate the Face-to-Face (F-to-F) interaction and proximity between doctor and patients during the hospitalization phase, controlling the spread of infectious diseases. The IR-UWB technology has been exploiting as low-complexity ultra-low power and portable/wearable proximity sensor.
- CHAPTER 5 → to design and demonstrate a novel bio-inspired wearable soft actuator based on ElectroActive Polymer. Mimicking the muscle anatomy a concept modelling of a active fiber and a proof-of-concept of the working principle are detailed.

TABLE 1.1: Smart Textile projects — EU FP6 and FP7

Project Title	**Description**
WEALTHY Sept 2002–Feb 2005 (*Wealthy*)	Pioneering research to develop and test comfortable smart fabrics for biological monitoring–ECG and respiration.
OFSETH Mar 2003–Jun 2009 (*OFSETH*)	Focused on how silica and polymer optical fibers can be used for sensing vital parameters while being compatible with a textile manufacturing process.
MyHeart Jan 2004–Oct 2007 (*MyHeart*)	Development of Intelligent Biomedical Garments for monitoring, diagnosing and treatment of medical conditions.
WearIT@Work Jun 2004–Nov 2008 (*WearIT@Work*)	Aimed to prove the applicability of computer systems integrated to clothes, creating wearable interfaces for various industrial environments.
BIOTEX Oct 2005–Feb 2008 (*BIOTEX*)	Sought to develop biochemical-sensing techniques that could integrate into textiles. Project aimed to develop textile sensing patches to target bodily fluid sensing.
PROETEX Feb 2006–Jan 2010 (*PROETEX*)	Developed smart wearable garments for emergency disaster intervention personnel to improve safety, coordination, and efficiency.
STELLA Feb 2006–Jan 2010 (*STELLA*)	Sought to develop flexible and stretchable textile substrates with electrical interconnects.
CONTEXT Jan 2006–Jun 2008 (*CONTEXT*)	Focused on development of contactless sensors in textiles for monitoring ECG and EMG.
DEPHOTEX Nov 2008–Oct 2011 (*DEPHOTEX*)	Research and development of flexible photovoltaic textiles based on novel fibers.
MICROFLEX May 2008–May 2012 (*MICROFLEX*)	Development of flexible materials in the form of high added value smart fabrics/textiles which are able to sense stimuli and react or adapt to them in a predetermined way.
PLACE-it Feb 2010–Jun 2013 (*PLACE-it*)	Development of a technology platform for lightweight, thin and conformable opto-electronic systems interconnect technology.

- CHAPTER 6 → to turn the Gravity Load Countermeasure Skinsuit (GLCS) from a passive to an active wearable aerospace physiology countermeasure device for the astronauts. Custom adjustable stretch mechanism and load/stretch monitoring sensor has been designed, developed, tested and integrated within the GLCS. Finally, an ultimate wearable device able to monitor the astronaut's spinal elongation during the spaceflight based on an ultra-low power wireless data communication system and a custom piezo-resistive stretch sensor is presented.

The thesis aims to tackle with the aspects mentioned above with an "application driven" approach. For each solution, a proof-of-concept has been designed and developed.

Chapter 2

Pressure/touch sensor system – CADET project

This chapter presents a sensorized belt with four fully integrated pressure-touch sensors. A very-low complexity sensor able to measure a pressure variation (up to 4 MPa) and to identify with accuracy a contact event at around 10 kPa is proposed. The overall pressure/touch sensor integrates a transducer, based on piezo capacitive material, coupled with a read-out circuit designed around a ring-oscillator. This converts the capacitance variation of the transducer into a quasi-digital signal characterized by a frequency range of 36.3 - 270 kHz with a very low standard deviation (2.3 kHz) and a sensitivity of 2.2 Hz/Pa. The tight integration of the electronics with the transducer results in a very compact all-in-one sensor system (overall size is $20\,mm \times 20\,mm \times 10\,mm$). Further, a major benefit of a low complexity design is the low power consumption, measured to be $\sim 370\mu W$. Based on a quasi-digital approach (event-driven), the system is well suited for impulse-based wireless communication.

2.1 Introduction

Smart touch and pressure sensor technologies are experiencing a fast diffusion since they are suitable for manifold applications in biomedical, aerospace, industrial, automotive and robotic sectors (Almassri et al., 2015). By touching an object, we can tell if it is sharp or smooth; by holding it, we can estimate its weight. Recently, with the development of wearable computing, the need for a wide extended pressure sensor has increased. Such sensors have to be elastic and possibly extendable to cover a three-dimensional surface, robust to work in harsh environment and reliable to supply accurate measurements. Finally, they must be produced at low-cost to not affect the overall product cost. It becomes evident how a wearable computing concept is challenging. It requires new solutions that enable electronic components to fit into clothes. Different architectures have been proposed to resolve the contrasting needs for unobtrusive devices using the computing power supplied by more traditional electronics. A major issue of this new perspective is researching new materials to use as a support for electronics. In this case, a fabric substrate is very appealing: it is elastic and extendable (Lumelsky, Shur, and Wagner, 2000), supported by a well known technology and produced at low-cost. Some smart pressure-sensors interfacing with a flexible substrate have been developed, but they are either based on electro-optical fabric (Xu et al., 1993) which is not suitable for the low cost market, or they need expensive PCB electronics (Cannata et al., 2008).

In order to tackle these issues, sensors made with CMOS-MEMS technology are able to sense pressure variation with high accuracy in different conditions, where the overall sensor, including electronics and transducers, occupies a very small area ($< 500\mu m^2$) (Dai et al., 2009). Many micro capacitive pressure sensors have recently been manufactured by using MEMS technology. For instance, Habibi et al., 1995 used a surface micromachining process to fabricate a capacitive pressure sensor array on a glass substrate. The array consisted of electrically parallel individual sensors with composite $SiO - Cr - SiO_2$ diaphragms and vacuum-sealed cavities underneath, and the cavities were formed by etching an aluminum sacrificial layer. Thick film screen-printing technique was used from Sippola and Ahn, 2006 presenting a ceramic capacitive pressure sensor fabricated with a pressure sensitivity of $9.2\,fF/psi$. Otherwise, a capacitive pressure sensor with a sandwich structure was fabricated by Zhou et al., 2005 using a three-mask process and an anodic bonding, which the sensitivity of the sensor was $0.2\,pF/kPa$.

Despite these promising approach, pressure sensors based on CMOS-MEMS technology shows a high sensitivity to the detriment of a wide pressure range; further they need sophisticated and high cost manufacturing process. Notwithstanding the high performance, cost and complexity reduction is very important, and the proposed solution addresses these issues with sensors based on polymeric materials showing a great opportunity in order to be suited for diverse applications (Vaganov, 2010), such as polymeric sensor embedded with flexible fabric surface. They can change their physical and electrical properties as a response to an external stimulus and this variation needs to be converted in an electrical signal through a dedicated Read-Out Circuit (ROC)(Mandal and Sarkar, 2010).

The technology based on polymeric conductors is growing since they exhibit electromechanical transduction properties suitable for smart fabrics implementation. Recent developments of polymer-based devices are directed toward active electronic components (transistors) (Garnier et al., 1994) and batteries (Schoch and Saunders, 1992) providing essential instrumental functions (power supply, sensor, actuator, and processor) which can be implemented into fabric substrates. In particular, polymeric conductors are prepared in the form of fiber coatings and spun fibers so as to be incorporated into distributed strain and temperature sensors (Scilingo et al., 2003). The combination of smart materials, read out electronic circuits and robust communication systems in a compact, reliable and low cost sensing device is one of the greatest challenges. This is particularly true in the case the device has to be space grade, low power consumption, suitable for wireless communication and integrated with a flexible fabric substrate, where the transmission line interference is a common issue (Harsányi, 2000). Generally, to address these requirements, current pressure sensor solutions present a partially or absent integration between the sensing material and the specific conditioning circuitry in a unique and compact device, resulting often bulky, too complex, with high power consumption and unsuitable to be interfaced with a fabric substrate (Vaganov, 2010).

From a ROC point of view, with the proper mixed analog-digital approach it is possible to encode the analog information in the time-domain with a robust, reliable periodic digital signal and a small and low power consumption circuit. The quasi-digital approach is able to preserve the original information with high accuracy. Main advantages are high noise immunity and signal to noise ratio, high output signal power, ease of interface (and cabling) with digital systems (Monkman et al., 2005). In comparison, common Analog to Digital Converters (ADCs) are more susceptible to interference from the surrounding noisy environment, e.g., through cables wired in a textile structure, also they are more power hungry solution. All the attractive properties of a quasi-digital systems, make them a well suited candidate for sensor in the aerospace application, solving the just mentioned problems, or more in general in a noisy environment, up to the point that a standard has already been proposed (Yurish, 2007).

This paper presents four fully integrated low complexity pressure sensors embedded on a belt, designed to identify with accuracy a contact event with a space debris. The R&D project has the objective to perform preliminary development of enabling technologies required for Active Debris Removal from LEO orbits. The project focuses in particular in-space capture concepts for large space debris, such as upper stages of elderly launchers or decommissioned satellites. The sensorized belt, coupled with a grasping system of the satellite, performs the task of monitor the contact and then the pressure with a de-orbital target. Figure 2.2 depicts a system using simulation. Each pressure sensor is constituted by an advanced polymeric material with piezo capacitive properties, a quasi-digital ROC, a power supply

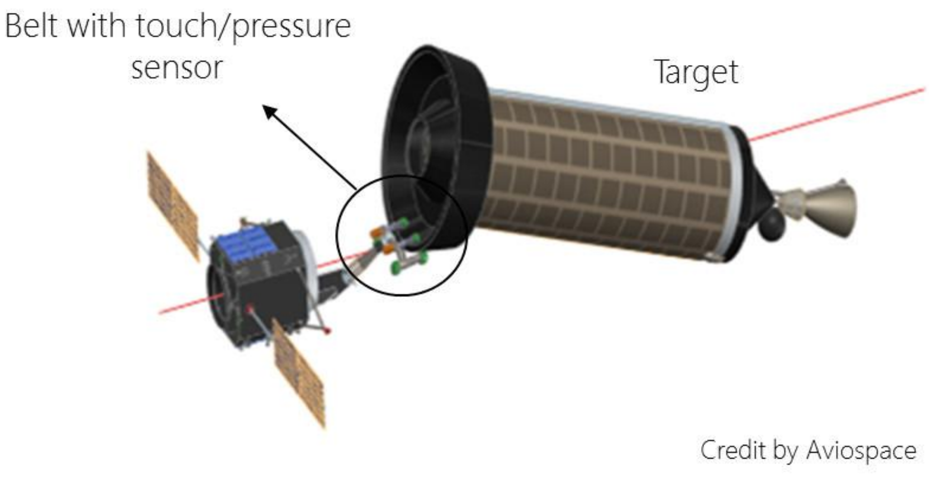

FIGURE 2.1: CADET system using simulation

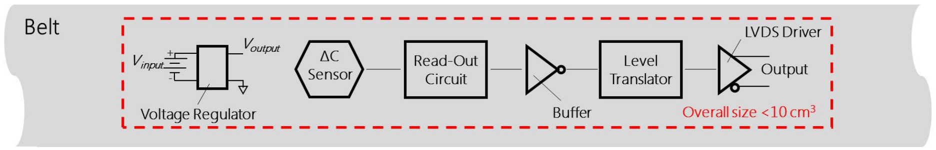

FIGURE 2.2: Sensorized belt system architecture

and a robust communication system. Consistently with multi-node pressure sensors, a wireless approach enables more flexible and portable systems, but (if not properly designed) it could have a strong weight in terms of power consumption. The system is arranged for wireless communication and, in particular, the Impulse-Radio Ultra-Wide Band (IR-UWB) technology would allow an ultra-low power data transmission with a small size transceiver (Crepaldi et al., 2012).

Paragraph 2.2 reports the circuit architecture, the transducer design and fabrication are detailed in Paragraph 2.3. System integration of the system with a fabric belt and experimental results are shown in Paragraph 2.4 2.5 and the State-Of-the-Art (SoA) discussion in Paragraph 2.6 concludes this Chapter.

2.2 System Architecture

Figure 2.2 shows the overall system architecture in which the sensing material, connected an ad-hoc ROC convert the analog information into a quasi-digital signal. Then a buffer and a level translator condition the signal for the LVDS driver, ensuring a robust differential, serial communications protocol and simple interface with other digital system. Current realization has a size of $17\,mm \times 15\,mm$ that is fully comparable with the transducer

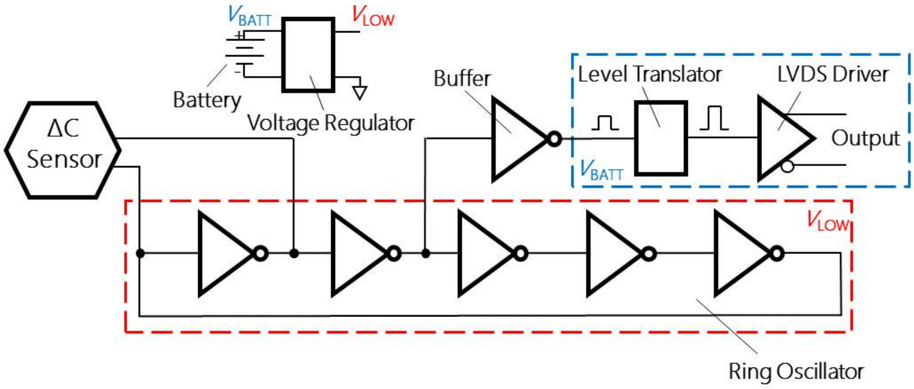

FIGURE 2.3: Read-out circuit architecture comprising the ring-oscillator in low-voltage supply domain, the piezo capacitive transducer across the first inverter terminals of the chain, the output buffer, the level translator and the LVDS driver.

size (20 mm×20 mm)(Mandal and Sarkar, 2010). The core of the circuit is the Ring Oscillator (RO). It is used to convert the capacitance variation due to the pressure exerted on sensor into a frequency shift of the output signal. The RO has some attractive features suitable for our purposes:

- it presents a low-complexity fully-digital implementation and design with state-of-art integrated circuit technology (CMOS);
- it works with low voltage supply without requiring any external or specific tuning;
- it is a very low power consumption circuit (a key point in a future wireless perspective).

Figure 2.3 shows the RO circuit design in which an odd cascade of digital inverters, connected in a closed loop chain and thereby oscillating at a frequency proportional to the chain length and the intrinsic gate delays. The linear relation between the inverter delay and the frequency oscillation (f_{osc}) is given by Eq. 2.1

$$f_{osc} = \frac{1}{T_{osc}} = \frac{1}{2 \cdot n \cdot t_{inv}} \tag{2.1}$$

where t_{inv} is the delay of each inverter and n is the number of inverter elements. A five-stage ring oscillator is adopted as the sensing circuit owing to the fact its phase noise is smaller than of three-stage ring oscillator ensuring a stable output signal(Mandal and Sarkar, 2010). The piezo-capacitance sensing material is connected across the first inverter of the chain and following the Eq. 2.1, the frequency oscillation become

$$f_{osc} = \frac{1}{2(5 \cdot t_{inv} + t_s)} = \frac{1}{2(\frac{5C_l \cdot \Delta V}{I_a} + \frac{C_s \cdot \Delta V}{I_a})} \tag{2.2}$$

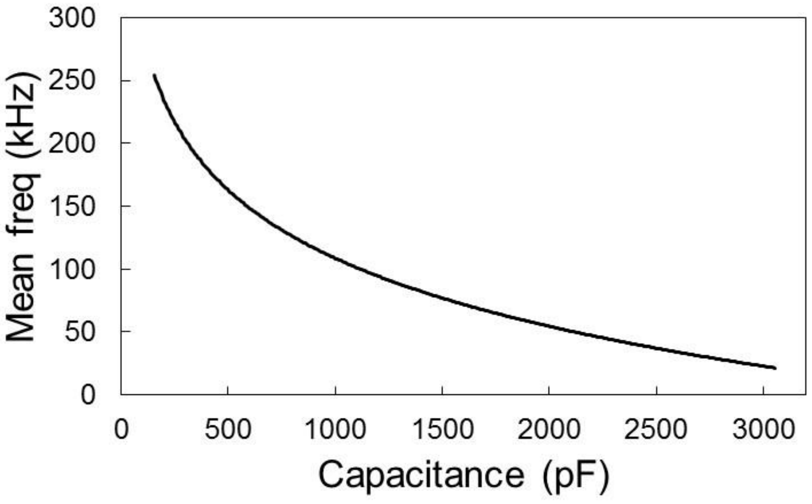

FIGURE 2.4: Simulated results of the capacitive pressure sensor.

where t_{sens} is the delay time associated to the capacitive pressure sensor, C_l the intrinsic load capacitance of each inverter, C_s the sensor capacitance, and Δ V and I_a are the threshold voltage and average current, respectively. According to the Eq. 2.2 a pressure variation, and then a capacitance shift, changes the frequency oscillation of the ROC. The commercial 74HC04 IC hex inverter is the component selected to design the RO architecture. Considering the CMOS parameters of the 74HC04 IC, the RO was simulated with National Instrument Multisim, as depicted in Figure 2.4 shows the results which the pressure sensor capacitance varies from 150 pF, nominal value capacitance when a pressure is not applied, to 3,000 pF range, according to the final application. The voltage supply affects the performance (mainly the frequency accuracy) of the output signal; to meet the desired frequency variation and accuracy we set the supply voltage at 1.05 V. This voltage value, obtained using a low-dropout linear regulator in an adjustable configuration, had been determined after an extensive experimental measurement analysis minimizing the standard deviation of the output signal.

The buffer inverter is connected through a level shifter to the LVDS driver able to convert the RO output into a robust signal. This choice ensures a standard electrical level, that is easy to interface with an external systems. Furthermore, it makes the communication more robust with respect to the transmission line interference that would eventually lead to incorrect measurements.

2.3 Transducer

A relevant part of the work was the realization of the transducer able to achieve the project's constraints. The proposed piezo-capacitive transducer is based on concepts and materials that are suitable for space applications, tackling more challenge requirements/constrains with respect to the former. In particular, a crystalline-semiconductor-based approach was avoided, to guarantee radiation hardness, working on the nanocomposite approach. Functional fillers (Multi-Walled Carbon Nanotubes, MW-CNTs) were added to a polymer matrix with superior proposed earlier, based on other piezoresistive materials (Oliva-Avilés, Avilés, and Sosa, 2011). MW-CNTs (Nanocyl 7000) were mixed in a ratio of 90:1 with a polydimethylsiloxane matrix (Wacker Chemie RTV-S691), adding also the curing agent in a ratio 9:1 and finally performing a thermal curing at $60°C$ in 4 h. The nanocomposite material was cured in a hexagonal prismatic mold and then contacted for the electrical characterization/functional tests using metalized Kapton® foils.

2.4 System Integration

Figure 2.5 (a) shows the overall system in which the sensing material, placed above the belt, used as a support, is wired with the electronics on the other side (Figure 2.5 (b)). The piezo-capacitive transducer, with a sensitive surface of $4\,cm^2$, is combined with an electronic board whose size is $17\,mm \times 15\,mm$. Figure 2.5 (c) depicts the PCB designed developed according to the system architecture and using the commercial 74HC04 IC hex inverter soldered on the top layer and the reminder of remainder of the components have been routed on the bottom layer (Figure 2.5 (d)).

2.5 Experimental Results

The CADET project aims to develop a complex system of removal of debris from business orbits through the development of enabling technologies in their capture. The project requirements to follow were in detail,

- small size of the overall system (within $10\,cm^3$);
- high touch sensitivity (less than 120 kPa);
- wide pressure range (up to 1 Mpa);
- to be integrated with a flexible fabric surface.

These features, in particular the wide pressure range, make it suitable for several applications, for instance to enhance the handling of a robotic

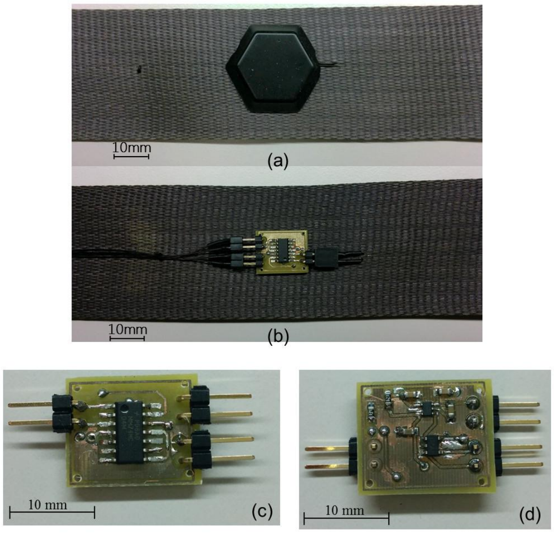

FIGURE 2.5: Prototype of a sensorized belt for CADET project: (a) piezo capacitive polymeric material on the top side, and (b) the small read-out circuit PCB on the bottom side with proper wiring across the textile structure for power supply and input/output signal. The belt was provided by Aerosekur

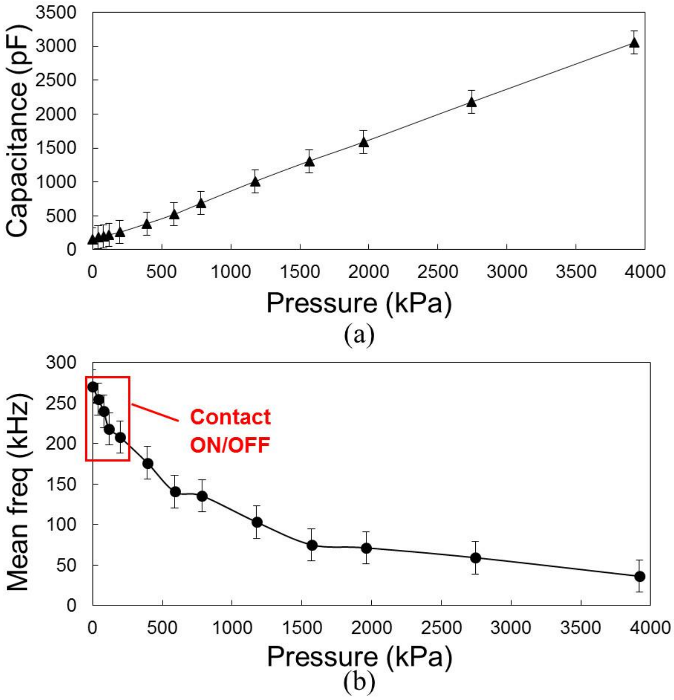

FIGURE 2.6: (a) Sensing material characteristic measured with a high accuracy digital impedance meter at different calibrated weights. (b) Experimental results in which the mean frequency shows a steep variation during a contact event with pressure <120 kPa. While with higher pressure the frequency decrease more softly.

arm or to monitor the breath ratio in a wearable system (Cannata and Maggiali, 2005; Hoffmann, Eilebrecht, and Leonhardt, 2011) application fields where the accuracy and the low impact integration are essentials. The thermomechanical preliminary analyses performed on the samples allowed to conclude that the degradation temperature is $396°C$ in air, which make the nano-composite suitable for external space application too where the temperature of the sun-facing side can reach 250°C (Senesky et al., 2009).

From an electrical property point of view, Figure 2.6 shows a perfect linear capacitance variation at different pressure level of the nanocomposite material. The characterization has been carried out using calibrated weights, within a range of 0 to 10 kg, placed on the top of the sensor, with a sensing area of 400 mm^2. The capacitance variation was measured with the Agilent precision impedance analyzer 4294A.

As explained in Paragraph 2.1, when a pressure is applied on the top of the sensor, the RO frequency shifts. As the pressure varies from 0 to 3,920 kPa, the frequency changes from 270 to 36.3 kHz at room temperature. According to the Figure 2.6, the experimental result shows a sharply decrease at low pressure (<120 kPa) followed by a steadily decrease at higher pressures. The wide frequency variation at low pressure is suitable for contact sensing and, at the same time, a smoother change of the frequency allows to expand the pressure range without reaching higher values. Following the requirements of the project, a pressure detection within 0−250 kPa range (Contact ON/OFF detection range) is suitable to observe a contact event with an orbital debris and in addition to measure the amount of the contact. The frequency standard deviation has a steady trend for all measurements and a very low value, around 2.3 kHz, with respect to the frequency value (low relative error of 1%). This result is significant in terms of read-out accuracy with a maximum sensitivity of 2.2 Hz/Pa, considering the narrower pressure interval (ΔP) measured of $1\,N/cm^2$ obtained with 100 g calibrated weight placed on the top the pressure sensor. Furthermore, the sensor responds reactively to a pressure, with $\sim 10\,ms$ relaxation time. The overall system consumes $\sim$ $100\,\mu A$ 3.3 V, and this corresponds to $\sim 370\,\mu W$ power consumption.

2.6 Discussion and Conclusion

Table 2.1 compares the integrated sensor system, sensing material plus ROC, w.r.t. other similar pressure (or force) sensors, specifically used to be coupled with a fabric substrate. A relevant benefit of the sensor system proposed in this paper in comparison with the State-of-the-Art is the presence of a high pressure range combined with a high sensitivity and the change to integrate the overall system (transducer plus ROC) in a small place. This

TABLE 2.1: Comparison with the State-Of-the-Art and Commercial products.

	This work	Dai et al., 2009	Shu et al., 2015	Hoffmann et al.,2011	ALmassri et al., 2014	*Kistler*
Approach	$\Delta C to \Delta f$	$\Delta C to \Delta f$	$\Delta C to \Delta V$	CDC	$\Delta R to \Delta V$	$\Delta R to \Delta V$
Output ROC signal	Quasi-digital	Quasi-digital	Analog	Digital	Analog	Analog
Range(kPa)	$0 - 4,000$	$0 - 500$	$0 - 15$	$0 - 80$	$0 - 10$	$0 - 50,000$
Sensitivity	2.2 Hz/Pa	7 Hz/Pa	50 mV/kPa	N.a.	0.4 V/Pa	5 mV/Pa
Power consumption (mW)	0.37	N.a.	N.a.	185	N.a.	25
Size (cm^2)	0.4	0.06	~ 20	~ 30	~ 50	~ 15
Sensor-ROC integrated	Yes	Yes	No	No	No	Yes
Application	Wearable/Aerospace	N.a.	Biomedical	Biomedical	Robotic	Automation

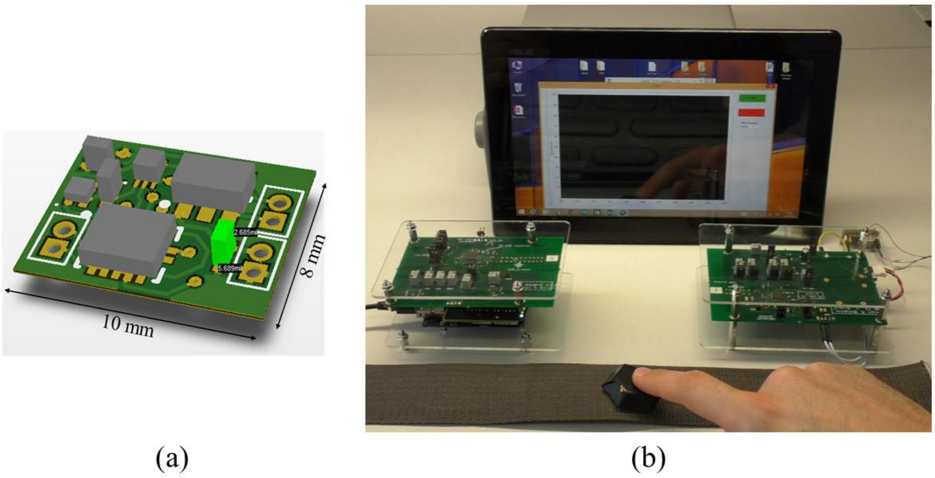

(a) (b)

FIGURE 2.7: (a) 3D model of the tiny ROC version. (b) Sensorized belt coupled with the IR-UWB system and the real time results plotting.

can ensure a reuse of the system for further applications. Technology approach, type of ROC, sensing performance, size and power consumptions are meaningful metrics to figure out the real potential of the prototype in this paper. Furthermore, the sensor system can be significantly improved in terms of integration through the PCB re-design proposed in Figure 2.7 (a). Choosing smaller components package, a size reduction of the overall system is obtained and this would allow an incorporation of the circuit directly inside the transducer. Figure 2.7 (b) depicts the implementation of the sensorized belt with a ultra-low power IR-UWB wireless transmitter. Then the information transmitted to a IR-UWB receiver is elaborate and streamed via WiFi technology in real time on a custom user interface wrote in C# with Microsoft Visual Studio (see source code in Appendix). The receiver is coupled with a MCU in which the firmware code (see source code in Appendix) allows to encode the information of the quasi-digital signal received. This demonstrator allows to show the easy interface of the sensorized belt with a very low power wireless communication based on IR-UWB, a promising technology for wearable application thorough and detailed in Chapter 3.

Chapter 3

Ultra-Low Power Wireless Data Transmission Impulse Radio UltraWide Band (IR-UWB)

Wearable and wireless technology has been developing fast for years and is spreading to new areas of everyday life. Interest in Wireless Body Area Networks (WBANs) has increased significantly thanks to the advances in microelectronics and wireless communications of the wearable technologies. Owing to the very stringent application requirements, in terms of reliability, energy efficiency and low device complexity, the Impulse-Radio Ultra-Wide Band shows a promising solution for the next generation of wearable devices. This chapter introduces and analyzes an ultra-low power and low-complexity analog IR-UWB radio system able to stream in analog mode and with a high quality a complex information, such as audio signal. At the TX, signal is modulated using a VCO which generates pulses with variable rate (PRF modulation), for an average of 600 kHz. At the RX an asynchronous and interference-robust detector regenerates the modulated signal at half frequency without requiring phase-locking, which is successively processed by a passive FM detector. The obtained demodulated signal is filtered using a fourth order Sallen-Key cell. The TX and RX systems based on commercial components demonstrate a very low power consumption with a power consumption of 6.8 mW and 36 mW, TX and RX respectively. Both systems include RF-CMOS chipset technology which operate at 3.5 GHz center frequency and 1.2V supply. The demonstrator of the solution proposed, transmits an audio signal with a $THD < 1\%$ for a continuous play time of 50 h (TX) and 12 h (RX), and 2.5 m radio range.

3.1 Introduction

Wearable and wireless sensor-based systems have drawn increasing attention from the scientific community and the industry world. Wireless communication for wearable sensor systems, compared to wired ones, is more convenient for the user. Systems with wireless communications is more likely to be unobtrusive and user friendly. Recent developments in wireless networking (Otis and Rabaey, 2003), micro-fabrication (Ghovanloo and Najafi, 2002), and integration of physical sensors, embedded microcontrollers and radio interfaces on a single chip (Jovanov et al., 2005), promise a new generation of wireless sensors suitable for many applications (Raskovic, Martin, and Jovanov, 2004). However, the existing telemetric devices either use wireless communication channels exclusively to transfer raw data from sensors to the monitoring station, or use standard high-level wireless protocols such as Bluetooth that are too complex, power demanding, and prone to interference by other devices operating in the same frequency range. These characteristics limit their use for prolonged wearable monitoring.

The solving of the short-range wireless communication issue for wearable applications requires deep power consumption awareness solutions, provide so far limited continuous operation time, which may hinder usefulness and attractiveness as users need to frequently replace or recharge batteries. The main issues to be accounted to design a wireless wearable device are:

- the human body radio wave interference;
- battery life;
- coexistence with other wireless networks.

Furthermore, the reliability of the wireless transmissions is another relevant factor, especially for medical applications. The reliability of transmissions is extremely important since wrong data can cause wrong conclusions, for instance in the case of wearable devices for physiological parameters monitoring.

Within the wearable field, particular interest in Wireless Body Area Networks (WBANs) is growing significantly in recent years thanks to the advances in microelectronics and wireless communications. A WBAN is a network with its communications devices in very close proximity to the human body (Jovanov et al., 2006). A wearable device used for WBAN application typically consists of a collection of low-power, miniaturised, invasive or non-invasive, lightweight devices with wireless communication capabilities that operate in the proximity of a human body. These devices can be placed in, on, or around the body, and are often wireless sensor nodes that can monitor the human body functions and characteristics from the surrounding environment and/or physiological parameters. Wireless communication for wearable sensor systems, compared to wired ones, is more convenient for the user. Systems with wireless communications is more likely to be unobtrusive and user friendly. Started from more than 15 years ago, the Internet of Things (IoT) theorized objects and people would connect "wirelessly".

Bluetooth technology is one of the wireless technologies frequently used for wearable applications, however the next generation of wearable devices are seeking an average power consumption of a RF chipset reduced below $100\,\mu W$. Bluetooth modules for instance require encoding and decoding with significant latency at source and sink ends (Moon et al., 2015) (codecs are also proprietary, see $Bluetooth^{®}$) which significantly increases system complexity and power consumption. For instance a Bluetooth codec alone requires 7 mW power both at the TX and RX (Hermann et al., 2004). Moreover, packet-based communication has typically several symbols of overhead besides payload which impacts on the transmitter consumed energy.

The emerging UWB technology promises to satisfy the average power consumption requirement for RF interface, which cannot be achieved by using narrowband radio communication, improving the lifetime of the battery. In particular, Impulse-Radio Ultra-Wide Band (IR-UWB) technology is becoming increasingly popular in WBAN application (Yang and Yacoub, 2006; Latré et al., 2011), thanks to its low-complexity and low energy consumption (Ryckaert et al., 2005). IR-UWB is indeed based on the transmission of nanosecond-order duration pulses enabling aggressive duty cycling at the transmitters (TX), e.g. 0.1% at 1 Mbps raw data rate, permitting ultra-low power (ULP) transmission in portable, wearable and implantable medical devices (Pomalaza-Ráez and Taparugssanagorn, 2012).

The solution proposed is an low-complexity and ultra-low power analog IR-UWB system operating in the $3.1 - 5\,GHz$ band where the transmitter can be aggressively duty cycled ($< 1\%$ pulse duration) achieving significantly lower energy consumption compared to standard packet-based wireless systems (Stoppa, Demarchi, and Crepaldi, 2015). The input signal triggers the generation of TX UWB pulses, without a continuous transmission but only on UWB spiking with an average energy of 30 pJ/pulse. This approach allows a drastic power savings and lifetime of the battery. Then, an asynchronous and interference-robust RX modules regenerates the modulated signal without requiring phase-locking or further network infrastructure. The results proposed aims to demonstrate a real chance of a future replacement of the current short-range wireless system for wearable applications.

3.2 UWB Technology

Ultra WideBand (UWB) has emerged as a technology which offers a huge potential to satisfy the ever increasing demand for low-cost, low-power and

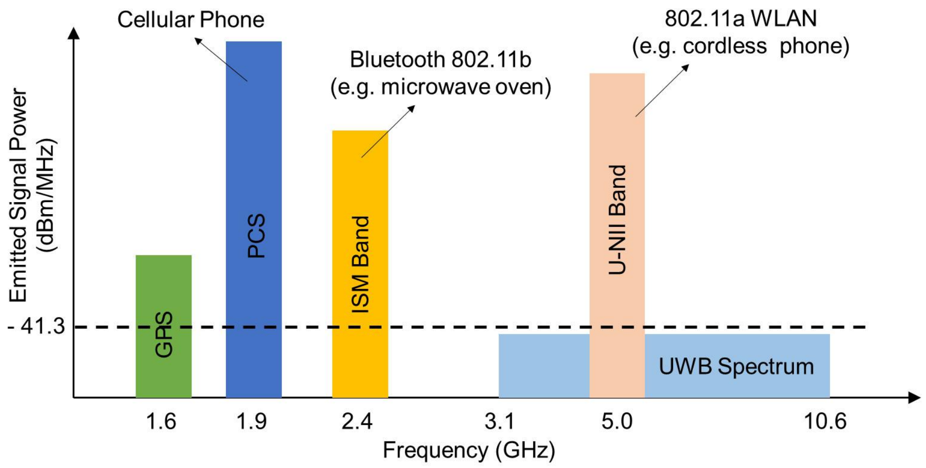

FIGURE 3.1: UWB spectrum overlaying with other existing narrowband systems.

miniaturized device. UWB is based on the transmission of digital data over a wide frequency spectrum (Figure 3.1) with very low energy and at high data rate (Nikookar and Prasad, 2008). The large bandwidth offers several advantages including low power consumption, low-cost implementation, resistance to interference, coexistence with narrowband systems, covert transmission and high data rate(Choi et al., 2004).

In February 2002, Report and Order by the Federal Communications Commission (FCC) authorizes the unlicensed use of UWB in 3.1-10.6 GHz with the power spectral density (PSD) satisfying a specific spectral mask (*UWB Federal Communications Commission*). UWB transmits information spread over a large bandwidth, ($> 500\,MHz$), with an antenna transmission for which emitted signal bandwidth exceeds the lesser of 500 MHz or 20% of fractional bandwidth. This is intended to provide an efficient use of scarce radio bandwidth while enabling both high data rate personal-area network (PAN) wireless connectivity as well as longer-range, low data rate applications as well as radar and imaging systems. For wireless communications, the power levels regulated by the FCC are extremely low (i.e., $-41.3\,dBm/MHZ$), which allows the UWB technology to overlay with existing services such as GPS and WLAN (Lansford and Shoemaker, 2007).

Since the low power spectral density of UWB, its interference can not be considered by many existing system occupying the same frequency bands. This property enables the unlicensed operation of the USB devices. Multipath interference occurs when a modulated signal arrives at a receiver from different paths. However, the short pulses of UWB provide robust performance even in dense multipath environments due to their fine time resolution.

The low complexity and low cost of UWB system arises from carrier-free nature of the signal transmission. Specifically, due to its ultra-wide bandwidth, the UWB signal may span a frequency normally used as a carrier frequency. This allows to not consider additional radio-frequency (RF) mixing stage as required in conventional radio technology. Furthermore, the absent of carrier modulation of pulse-based UWB, helps in reducing the size and cost of UWB devices compared to conventional narrowband systems (Christopher, 2005).

3.2.1 Impulse Radio UWB

Impulse radio principles date back to the early days of wireless technology, with experiments of the German physicist H.R. Hertz in the 1880's and with impulse transmission made by the Italian-born radio pioneer G. Marconi. Nevertheless, impulse radio is being considered as a potential technology for some next generation wireless network (Chong, Watanabe, and Inamura, 2006). UWB is currently the basis of one of the physical layers specified by the IEEE 802.15.4a standard (PISCATAWAY, 1996) and encounters applications in cognitive radio (CR) systems (Zhang et al., 2006).

A UWB system transmits pulses of very short duration with a low duty cycle. This means that the ratio between the pulse transmission instant and the average time of two consecutive transmissions is kept small. Such pulse based UWB signalling scheme is called Impulse Radio. Impulse radio communicates with baseband pulses of very short duration, typically on the order of a nanosecond, thereby spreading the energy of the radio signal very thinly from near d.c. to a few GHz (Gezici et al., 2005). When this pulse is applied to an appropriately designed antenna, the pulse propagates with distortion. The antennas behave as filters, and even in free space, a differentiation of the pulse occurs as the wave radiates (Choi et al., 2004). Impulse radios, must contend with a variety of interfering signals, and also must insure that they do not interfere with narrowband radio systems operating in dedicated bands. These requirements need the use of spread-spectrum techniques (*UWB Federal Communications Commission*). A simple means for spreading the spectrum of these UWB bandwidth low-dutycycle pulse trains is time hopping, with data modulation accomplished by additional pulse position modulation at the rate of many pulses per data symbol. There must be a real payoff in the use of impulse radio to tackle the difficult problem of coexistence with a myriad of other radio systems. Multipath resolution down to a nanosecond in differential path delay (equivalently down to a differential path length of one foot) leads to an elimination of significant multipath fading (Foerster, 2001). This may considerably reduce fading margins in link budgets and may allow low transmission power operation. Due to its significant bandwidth, an impulse radio based multiple access system may accommodate many users, even in multipath environments.

The IR-UWB does not require the use of additional carrier modulation for transmission, as the pulse propagated in the radio channel. The technique is therefore a baseband signal approach (Norimatsu et al., 2007). This technology has a low transmit power and also has a fine time resolution due to the sharp transmitted pulses.

Capability of IR-UWB technology for precise distance measuring and positioning in WBAN has been established in recent time (Gigl et al., 2007; Sahinoglu, Gezici, and Guvenc, 2008; Yang et al., 2013). IR-UWB is viewed for its potential application in through-wall radar, medical imaging, sensor networks, robot positioning, tracking and supervision. The key point of these application is to evaluate the distance of the target (Monica and Ferrari, 2014).

3.2.2 Modulation Techniques

Modulation is the process where one or more properties (frequency and amplitude) of a periodic waveform are altered. Several techniques have been employed to modulate UWB signal which, depicted in Figure 3.2 includes Pulse Position Modulation (PPM)(Ge, Yue, and Affes, 2002), Pulse Frequency Modulation (PFM) (Stoppa, Demarchi, and Crepaldi, 2015), On-Off Keying (OOK)(Phan et al., 2007), Pulse Amplitude Modulation (PAM)(Liu, 2003) and Binary Phase Shift Keying (BPSK)(Liu, 2003). There are many other techniques but above stated techniques are preferred and are adopted in accordance with their application.

PULSE POSITION MODULATION - PPM

Information is encoded with the position of the pulse as shown in 3.2 (b) where one bit is encoded in each pulse. The pulse which is transmitted at nominal position is referred to bit 0, and pulse transmitted after the nominal position is referred to bit 1. PPM signal is described by the Eq. 3.1

$$s(t) = \Sigma_k^{\infty} p(t - kT_f \pm T_{pk}) \tag{3.1}$$

where UWB pulse $p(t)$ is modulated by small shift in the pulse position T_{PK} with in the frame interval T_f.

PULSE AMPLITUDE MODULATION - PAM

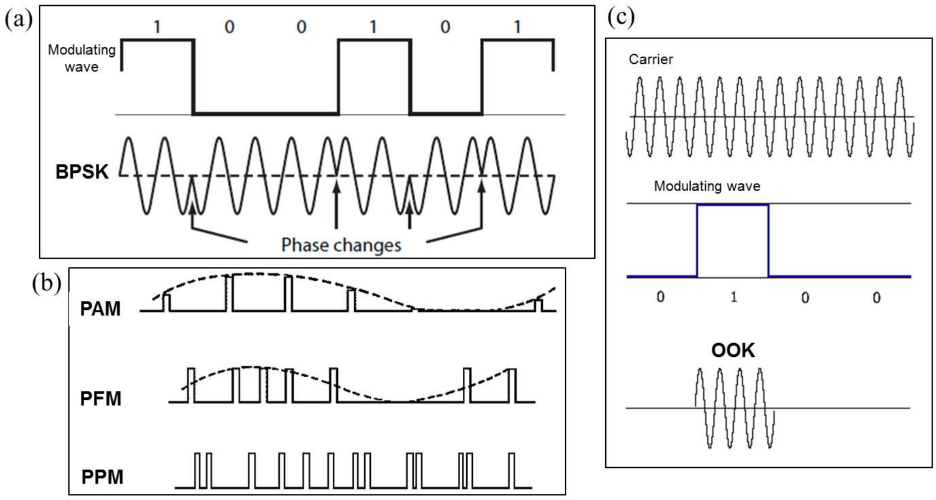

FIGURE 3.2: RF modulation:(a) BPSK, (b)PAM, PFM, PPM and (c) OOK modulation.

Information is encoded by varying the amplitude of the pulses as shown in 3.2 (b) which shows modulation that includes zero and lower amplitude respectively. PAM signal is described by

$$s(t) = \Sigma_k^{\infty} a_k p(t - kT_f) \tag{3.2}$$

BINARY PHASE SHIFT KEYING - BPSK

Information is transmitted by changing the phase of a reference signal. There are two polarities where one bit information is for each pulse hence known as bi-phase modulation. Generally signal is defined as

$$s(t) = \Sigma_k^{\infty} A_k p(t - kT_f) \tag{3.3}$$

where A_k is the amplitude of the pulse that take the values 1 and -1 with in the frame interval T_f and UWB pulse $p(t)$.

ON-OFF KEYING - OOK

Pulse is transmitted when information bit is 1 where as it is absent when information bit is 0. OOK can be define as

$$\begin{cases} 0, & j = 0 \\ 1, & j = 1 \end{cases}$$

An OOK implementation is very simple besides it has a poor performance due to noise and interference resulting in higher probability of false

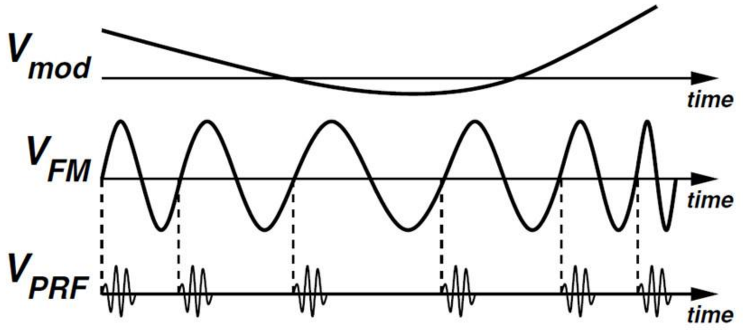

FIGURE 3.3: FM and PRF modulation

alarm.

PULSE FREQUENCY MODULATION - PFM
Information is transmitted by varying the frequency or repetition rate using fixed duration pulses. It is represented by analog signal using two levels 0 and 1.

3.2.3 Pulse Repetition Frequency Modulated UWB

The Pulse Repetition Frequency (PRF) modulation used consists in the number of pulses of a repeating signal in a specific time unit, normally measured in Pulses Per Second (PER). The term is used within a number of technical disciplines, notably radar. In radar, a radio signal of a particular carrier frequency is turned on and off; the term "frequency" refers to the carrier, while the PRF refers to the number of switches. PRF has a pulse period, τ , which is the time between pulses .

$$\tau = \frac{1}{PRF} \tag{3.4}$$

PRF is usually associated with pulse spacing (t_p), which is the distance that the pulse travel before the next pulse occurs.

$$t_p = \frac{\nu_t}{PRF} \tag{3.5}$$

where ν_t is the propagation speed.

As reported Padgett, 2003, which shows evident similarities between PRF ad FM, a PRF modulated signal $w(t)$ can be expressed as $w(t) = \Sigma_n p[t - kT(n)]$, where $p(t)$, k and $T(n)$ are the base pulse, a constant and the transmission time of the n-th pulse respectively.

Figure 3.3 shows an example FM and PRF modulated radiated voltage (V_{FM} and V_{PRF}, respectively) and their corresponding modulating signal V_{mod}. The difference between the two approach lies in the signaling of PRF

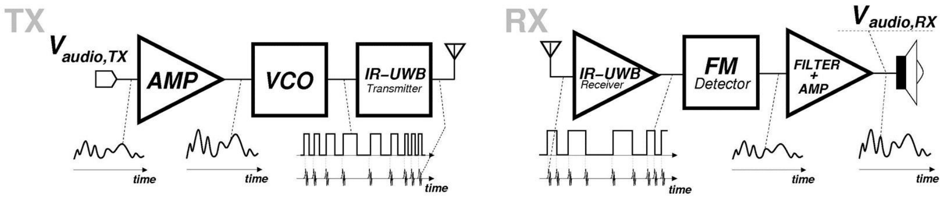

FIGURE 3.4: PRF IR-UWB system architecture for the transmission of a complex information, such as audio signals.

modulation which radiates a pulse every time V_{FM} crosses zero with a positive slope. Assuming a power amplifiers operating across the same load R (the antenna load) and a transmitter efficiency of μ_{FM}, the power consumption of the FM transmitter $P_{c,FM}$ is

$$t_p = \frac{P_{FM}}{\mu_{FM}} = \frac{V_{FM}^2}{2R \cdot \mu_{FM}} \tag{3.6}$$

where P_{FM} is the FM radiated power. On the other hand the power consumed at the transmitter $P_{c,PRF}$ with an efficiency μ_{PRF} is

$$t_p = \frac{P_{PRF}}{\mu_{PRF}} = \frac{V_{PRF}^2}{2R \cdot \mu_{PRF} T_p r_{TX}} \tag{3.7}$$

where T_p is pulse duration and r_{TX} is the average PRF. A typical radiated power for a personal FM transmitter IC for audio broadcast is -7 dBm (*Belkin TuneCast-II.*) which corresponds to $V_{FM} = 100\,mV$ on a $50\,\Omega$ load. An ordinary integrated IR-UWB transmitter can radiate about 150 mV on a $50\,\Omega$ load for $T_p = 2\,ns$. Considering an efficiency $\mu_{FM} = 20\%$ and $\mu_{PRF} = 10\%$ (*ROHM BH1417 Stereo PLL FM Transmitter.* Crepaldi et al., 2012) and the advantageous of the PRF at the TX if $r_{TX} < \frac{V_{FM}^2}{V_{PRF}^2}\frac{\mu_{PRF}}{\mu_{PRF}T_p}$ the result is $r_{TX} < 111.1$ MHz. Therefore, the PRF modulation is useful if the pulse rate is kept below the 111.1 MHz limit. The system presented in this Chapter, r_{TX} is 666 kHz, ensuring a lower energy consumption than FM modulation.

3.3 Radio System Architecture

Figure 3.5 depicts the system comprises a TX and an RX module that include an integrated chipset, with a very-low complexity TX and an interference-robust RX introduced, respectively.

TRANSMITTER (TX)

An analog IR-UWB system operating in the 3.1-5 GHz band where the transmitter can be aggressively duty cycled ($< 1\%$ pulse duration) and achieve significantly lower energy consumption compared to standard packet-based and FM wireless systems ((Stoppa, Demarchi, and Crepaldi, 2015)). The TX module receives and conditions the input signal ($V_{audio,TX}$) from a source (PC, mp3-player, smartphone, etc), and the incoming data, directly processing it and feeds a Voltage Controlled Oscillator (VCO) which generates a square wave proportional with frequency to the input signal level. When no input is applied the VCO oscillates at a nominal rate r_{TX}, and when signal is applied rate is modulated as Eq. 3.8.

$$r_{OSC,TX} = r_{TX} + \Delta r[\Delta V_{audio,TX}(t)] \tag{3.8}$$

where $\Delta V_{audio,TX}(t)$ is the amplitude variation of the audio signal in the bandwidth of interest, and Δr is its associated PRF variation compared to a null imput. The function Δr is assumed linear with the amplitude level of the signal $\Delta V_{audio,TX}$.

The VCO output ($V_{OSC,TX}$) digitally triggers the generation of pulses from the UWB-IC. Information is not conveyed on a continuous wave signal, but only on UWB spiking with $< 1\%$ duty cycling w.r.t. average pulse rate. The pulses with center frequency f_c and duration T_p are asynchronously triggered and radiated every time a positive edge occurs at $V_{OSC,TX}$. The RF signal is filtered by the TX antenna, and through path loss and channel impairments pulses reach the RX.

The transmission approach aims to achieve the following advantages:

- a very low complexity and ultra-low power consumption;
- a robust pulse rate drifts for signal detection;
- a lower number of pulses transmitted for a unicast transmission than packet based communication (e.g. Bluetooth);
- a TX/RX latency of hundreds nanosecond-order.

RECEIVER (RX)

The receiver captures the $V_{RF,RX}$ with an envelope threshold detector. The RX toggles a digital output ($V_{OSC,RX}$) every time a new pulse is received for an output rate of $r_{OSC,RX} = \frac{1}{2}r_{TX} + \frac{\Delta r}{2}$. $V_{OSC,RX}$ is a square wave, which directly feeds a passive linear-phase FM detector based on a frequency-to-amplitude conversion operating similarity to a zero-crossing detector. The detector input normally required a limiter in analog FM receivers to normalize amplitude variations in order to fed with frequency variation only. This is not required with the system used, since the $V_{OSC,RX}$

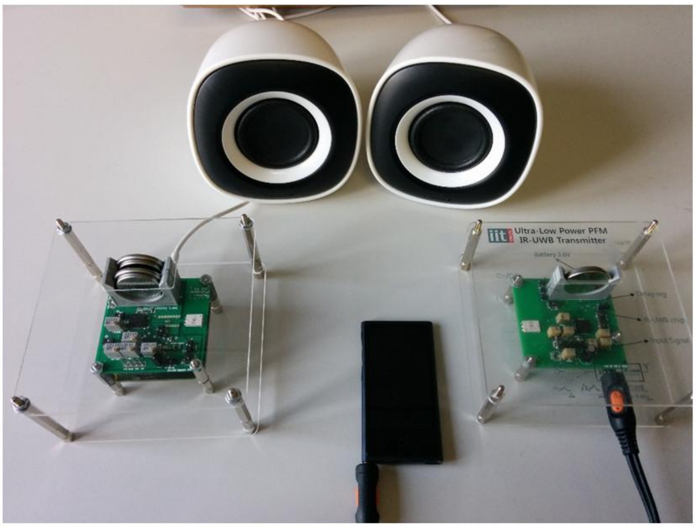

FIGURE 3.5: Analog-PRF modulated IR-UWB transmitter and receiver demonstrator.

is already full swing. The received signal can be then related to the transmitted one with,

$$V_{OSC,RX} = R(f)V_{OSC,TX} \tag{3.9}$$

where f is the Fourier frequency and R is the over-the-air linear transfer function. The passive FM detector is a frequency-to-amplitude converter while high frequency signals (out of the 0-20 kHz band) and noise are cutoff by a II° Order Sallen Key filter. The demodulated signal is amplified by instrumentation amplifier INA114 and fed to the loudspeakers ($V_{audio,RX}$).

3.4 Demonstrator Radio System

Figure 3.5 shows the live demonstrator of the analog-PRF modulated IR-UWB transmitter and receiver. A MP3-reader is connected to the TX module with a 3.5 mm audio-jack. The RX module tested about a meter away and connected to the loudspeakers.

3.4.1 IR-UWB Transmitter

Figure 3.6 (a) and (b) depict the schematic and (c) the routing of the TX IR-UWB module, respectively. The system is powered with a 3.6 V LIR2450 rechargeable Li-Ion batterie with 100 mAh capacity. Two linear voltage regulators (LDO) generate 1.2 V and 2.5 V for the integrated transmitter and the conditioning circuit plus VCO, respectively. TPS71712 and TPS71725

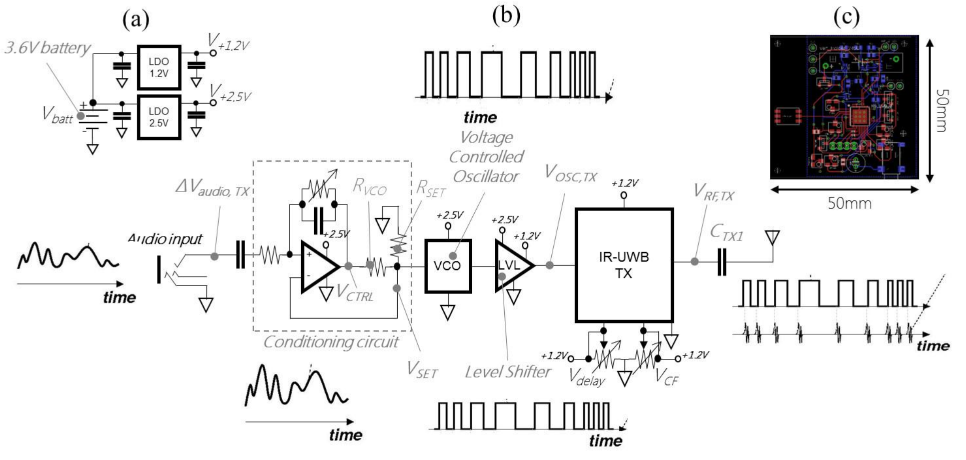

FIGURE 3.6: Schematic of the analog-PRF modulated IR-UWB transmitter. (a)The power supply circuit with 1.2 V and 2.5 V LDO; (b) the core of the TX circuit with VCO, Level Shifter and IR-UWB IC; (c) the PCB routing of the overall circuit.

(SC70-5 package) have been used. The advantages of a low dropout voltage regulator over other DC-to-DC regulators or voltage dividers.

- the absence of switching noise - as no switching takes place;
- a smaller device size (SOT23 have been used) - as neither large inductors nor transformers are needed;
- a greater design simplicity - stability obtained with a $1\mu F$ ceramic output capacitor

When the audio signal is applied, AC coupled through C_{TX1}, nominally $0.1\mu F$, and adapted to the imput range of the VCO. The LTC6990 voltage controlled silicon oscillator capable of operating in a $488 - 2Mhz$ frequency range and providing $< 1\%$ frequency drift across $0 - 100°C$ through the dedicated conditioning circuit. The VCO is able to oscillate with a certain frequency determined by internal master oscillator. R_{SET} programs the internal master oscillator frequency with determines the output frequency depending on N_{DIV} value. Tuning range of VCO is determined by the second resistor at SET input, which provides the control voltage. At output square wave frequency modulation (SWFM) signal is generated with a frequency inversely proportional to the control voltage. Table 3.1 lists the LTC6990 pinout.

VCO is designed with the following parameter for the input voltage of $0 - 2\,V$

$$\begin{aligned} f_{OUT,MAX} &= 1\,MHz\,at\,V_{CTRL,MIN} = 0\,V \\ f_{OUT,MIN} &= 200\,kHz\,at\,V_{CTRL,MAX} = 2\,V \end{aligned} \tag{3.10}$$

TABLE 3.1: LTC6990 pinout scheme.

V^+ and GND	supply voltage 2.25 to 5.5 V.
SET	Voltage is regulated to 1v at this pin, where master oscillator frequency is programmed with the amount of current sourced from SET pin.
DIV	Voltage at this pin determines the output frequency divider setting. V_{DIV} may be generated by the resistor divider.
DIV	Voltage at this pin determines the output frequency divider setting. V_{DIV} may be generated by the resistor divider.
OE	High value on this pin enables the output driver.
OUT	SWFM generated from GND to V.

For higher accuracy, the master oscillator frequency should be in between 62.5 kHz and 1 MHz range. In accordance with the datasheet N_{DIV} value must meet the following conditions

$$\begin{aligned} \frac{62.5\,kHz}{f_{OUT,MIN}} \leq N_{DIV} \leq \frac{1\,MHz}{f_{OUT,MAX}} \\ f_{OUT,MIN} = 200\,kHz\,at\,V_{CTRL,MAX} = 2\,V \end{aligned} \tag{3.11}$$

solving the Eq. 3.11 for given paramenters $0.3125 \leq N_{DIV} \leq 1$ then $N_{DIV} = 1$. Next, K_{VCO} determines the VCO gain and f_0 is the output frequency at $V_{CTRL} = 0$ and they are given by

$$\begin{aligned} K_{VCO} = \frac{f_{OUT,MAX} - f_{OUT,MIN}}{V_{CTRL,MAX} - V_{CTRL,MIN}} = 400\,kHz/V \\ f_{0V} = f_{OUT,MAX} + K_{VCO} \cdot V_{CTRL,MIN} = 1\,MHz \end{aligned} \tag{3.12}$$

The last step is calculate R_{VCO} and R_{SET} with the following Eq. 3.13 and 3.14

$$R_{VCO} = \frac{1\,MHz \cdot 50\,k\Omega}{N_{DIV} \cdot V_{SET} \cdot K_{VCO}} = 125\,k\Omega \tag{3.13}$$

$$R_{SET} = \frac{1\,MHz \cdot 50\,k\Omega}{N_{DIV} \cdot (f_{0V} - V_{SET} \cdot K_{VCO}} = 83\,k\Omega \tag{3.14}$$

VCO gain K_{VCO} accuracy depends on V_{SET} which can cause error in the output frequency since it is controlled by the voltage ratio of V_{CTRL} to V_{SET}. The frequency error due to ΔV_{SET} that is approximated by Eq. 3.15

$$\Delta f_{OUT} \cong K_{VCO} \cdot V_{CTRL} \cdot \frac{\Delta V_{SET}}{V_{SET}} \tag{3.15}$$

This means that the potential for error in output frequency due to V_{SET} error increases with K_{VCO} and become maximum, when V_{CTRL} is maximum. In VCO application, design is modified with the introduction of

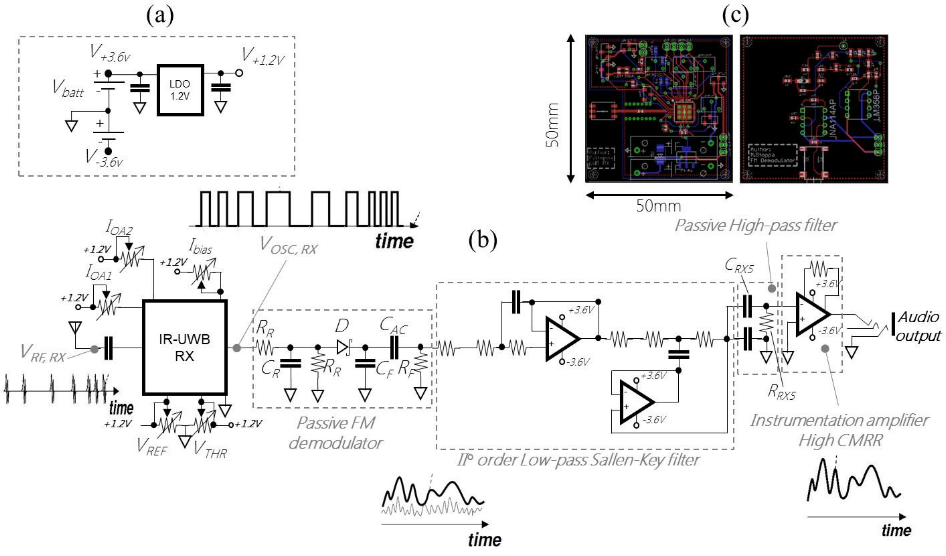

FIGURE 3.7: Schematic of the Analog-PRF modulated IR-UWB receiver.(a)The power supply circuit with 1.2 V LDO; (b) the core of the TX circuit and IR-UWB IC, FM passive detector, active low pass filter, passive high pass filter and instrumentation amplifier; (c) the PCBs routing of the overall circuits.

an OPA322 in inverting configuration to make V_{CTRL} dependent on V_{SET}. This circuit has a positive transfer function i.e. the output frequency is directly proportional to the input voltage V_{IN}. Now the maximum absolute frequency error occurs at highest output frequency hence the percentage relative frequency error is greatly improved. Finally, the output of the VCO spans 2.5 V, and it is adapted to the integrated receiver which works in a 1.2 V with a FCLP34P5X level shifter prior to the pulse trigger input. The TX module comprises an IC including the same transmitter presented by Crepaldi et al., 2012 which implements a flexible UWB pulse generator in a $0.004\,mm^2$ silicon area, with both center frequency and bandwidth tunability. The transmitter is directly connected to a chip antenna (Tayo Yuden) which filters the generated signal in the 3.1-10.6 GHz band and the system provided two analog controls V_{DELAY} and V_{CF} to set pulse duration and center frequency f_c. The integrated transmitter consumes a measured 30 pJ energy per transmitted pulse.

The result is a dual layers PCB ($50\,mm \times 50\,mm$), Figure 3.6 (c), with components and widespread ground plane on both layers. The system provides also different test-points to monitor the intermediate outputs. Aside the headers, all components are SMD and manually soldered.

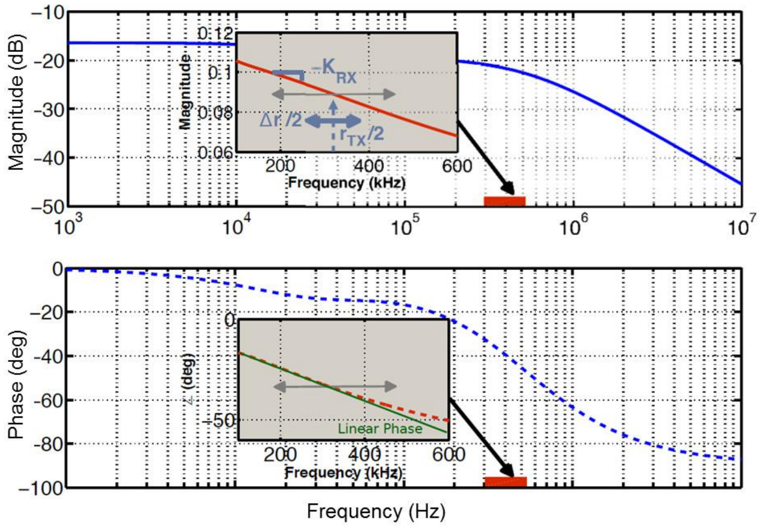

FIGURE 3.8: AC frequency response of the passive FM detector.

3.4.2 IR-UWB Receiver

The schematic and the routing of the RX IR-UWB are shown in Figure 3.7. The RX module comprises two rechargeable batteries mainly used to generate positive and negative power supply for the detector and filtering. From the positive supply domain,a TPS71712 voltage regulator brings down voltage to 1.2 V and power the IC receiver which requires three current and two voltage bias, $I_{OA1,2}$, I_{bias} for the front-end and V_{THR}, V_{REF} for the baseband, respectively. The integrated RX power supply ranges 0.9-1.2 V. The RX center selectivity is set to about 3.5 GHz, the center frequency f_c of the TX. The square wave output of the receiver is processed by a Shottky diode and a passive RC network. R_R and C_R are $1\,k\Omega$ and 470 pF, respectively, C_F and R_F are $1\,k\Omega$ and $748\,pF$ while C_{AC} is $3.2\,\mu F$. The cut-off frequency needs to be set where the phase rotation of the main pole is both linear w.r.t. to the received Δr, and where the amplitude conversion is linear, as well. The diode $D, C_F R_F$ and C_{AC} implement the detector core which aims at absorbing current from the upstream $R_R C_R$ network as a function of frequency. Figure 3.8 shows simulated the small signal AC frequency response of the passive detector. It is meant to operate in the region of the transfer function immediately after the main 3 dB cut off-frequency at 100 kHz, that is where frequency is linear with the magnitude response of the curve. The signal is then high-pass filtered with R_{RX5} and C_{RX5}, nominally $1.5\,M\Omega$ and $2\,\mu F$. The active speakers already available onto the market have an input impedance from 8Ω to 48Ω. The filtered signal is fed to an INA114AP instrumentation amplifier providing high common mode rejection without significant added noise.

As routing result, Figure 3.7 (c) shows two stackable dual-layers PCB

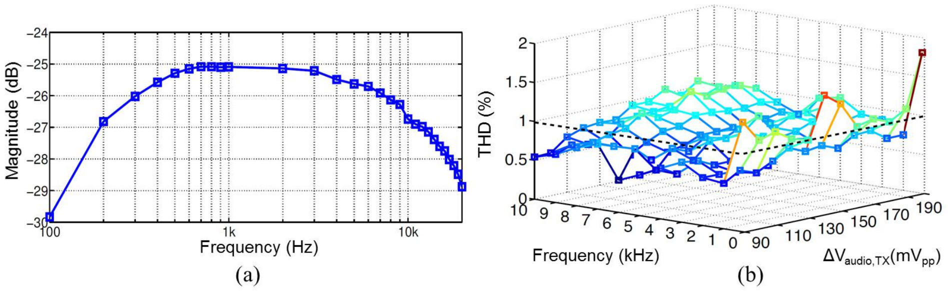

(a) (b)

FIGURE 3.9: Over-the-air transfer function. (a)Frequency response $R(f) = \frac{\Delta V_{audio,RX}}{\Delta V_{audio,TX}}$ of the complete pulsed UWB radio system operating over-the-air (no pulse error). (b) Radio System THD in the range 100 Hz−10 kHz

(both $50\,mm \times 50\,mm$). The top PCB hosts the IC receiver, power supply circuit and two socket batteries. The bottom PCB is routed with the passive FM detector, signal conditioning circuit and the jack female output.

3.5 Experimental Measurements

During measurements, both modules (tested in the range of $10 - 35°C$) are powered with the Li-ion batteries, and no additional filters besides antenna are included in the PCB. The INA114AP is set to $\sim 0\,dB$ gain. The integrated RX power supply ranges $0.9 - 1.2\,V$. In the over-the-air measurement sessions the integrated TX in Crepaldi et al., 2012 has been set to generate pulses at a center frequency of 3.5 GHz with bandwidth ranging 300 MHz−500 MHz, to match the FCC definitions, otherwise explicitly mentioned. The RX center selectivity is set to about 3.5 GHz, the center frequency f_c of the TX.

3.5.1 Over-the-Air Transfer Function

The modules (battery powered) are placed at a fixed distance of $\sim 0.5\,m$, and the TX is fed with a sine wave of amplitude $\Delta V_{audio,TX} = 200\,mV_{pp}$. By measuring Delta $V_{audio,RX}$ the over-the-air transfer function is computed. The small signal transfer function $R(f) = \frac{\Delta V_{audio,RX}}{\Delta V_{audio,TX}}$ includes the operation of the complete TX-RX system plus the IR-UWB channel response. Figure 3.9 (a) shows the small signal frequency response of the radio system. As shown, the 3 dB transfer function ranges $100Hz - 7kHz$ which falls in the audio signal bandwidth, typically $20 - 20kHz$ for Hi-Fi systems.

3.5.2 Pulse Error Rate

Bit Error Rate (BER) is a key parameter that is used in assessing systems that transmit digital data from one location to another. Systems for which the BER is applicable include radio data links as well as fibre optic data systems, Ethernet, or any system that transmits data over a network of some form where noise, interference, and phase jitter may cause degradation of the digital signal. Although there are some differences in the way these systems work and the way in which bit error rate is affected, the basics of bit error rate itself are still the same. When data is transmitted over a data link, there is a possibility of errors being introduced into the system. If errors are introduced into the data, then the integrity of the system may be compromised. As a result, it is necessary to assess the performance of the system, and bit error rate, BER, provides an ideal way in which this can be achieved. Unlike many other forms of assessment, bit error rate, BER assesses the full end to end performance of a system including the transmitter, receiver and the medium between the two. In this way, bit error rate, BER enables the actual performance of a system in operation to be tested, rather than testing the component parts and hoping that they will operate satisfactorily when in place.

As the name implies, a bit error rate is defined as the rate at which errors occur in a transmission system. This can be directly translated into the number of errors that occur in a string of a stated number of bits. The definition of bit error rate can be translated into a simple formula:

$$BitErrorRate(BER) = \frac{Number\,of\,errors}{Total\,number\,of\,bits\,transmitted} \tag{3.16}$$

Within this project, the transmission used is analog and a definition for Bit-Error Rate (BER) is not possible to adopt. However, the system is event-based, and the absence of an event trigger at the receiver impacts on signal demodulation, with audible pops and cracks (similarly to FM). We define RX sensitivity as the average input power so that Pulse Error Rate (PER) is 10^{-3}, similarly to digital communications (in some cases also 10^{-5} is enforced). With such average pulse miss (one pulse over 1000), no significant pops and cracks are audible. PER is here defined based on the hypothesis that the receiver does not toggle in absence of an event trigger at the TX, that is $P_{(ERX|ETX)} \longrightarrow 0$, where E_{RX} and E_{TX} are the trigger and toggling events at the TX and RX, respectively. As a consequence, a direct cause effect relationship is maintained through the transmission chain, and PER

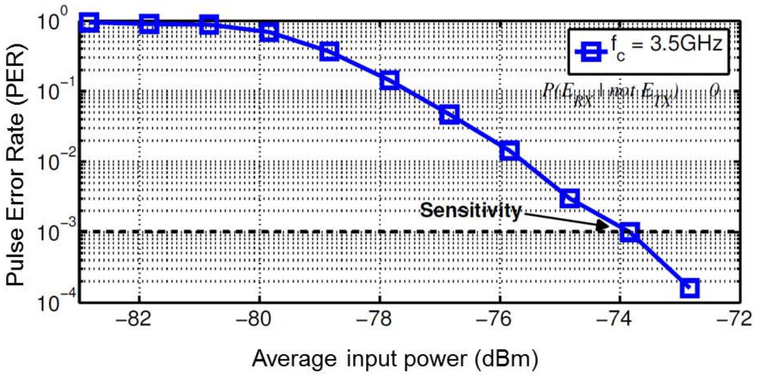

FIGURE 3.10: Receiver Pulse Error Rate (PER) with center frequency $f_c = 3.5\,Ghz$

.

can be defined as

$$PER = 1 - \frac{\Sigma E_{RX}}{\Sigma E_{TX}} \tag{3.17}$$

and assuming that no other event can lead the RX to toggle. The PER was measured using pulses lasting 10ns generated by a 12.5 kHz-12 GHz general purpose RF signal generator. Figure 3.10 shows the measured PER for a receiver sensitivity at 10^{-3} error ratio of -74 dBm. In presence of narrowband interference, however, the receiver can toggle also in absence of a pulse event trigger. Interference performance can be quantified based on the false triggers events per unity of time obtained injecting continuous wave interference at the RX input. In these conditions the false events can be considered additive to those obtained when the PFM modulated pulses are streamed.

3.5.3 Total Harmonic Distortion

A method to characterize the linearity of audio systems and the power quality of electric power systems is the Total Harmonic Distortion (THD). The total harmonic distortion, or THD, of a signal is a measurement of the harmonic distortion present and is defined as the ratio of the sum of the powers of all harmonic components to the power of the fundamental frequency. The THD is the summation of all harmonic components of the voltage or current waveform compared against the fundamental component of the voltage or current wave. The THD is expressed by the Eq. 3.18

$$THD = \frac{\sqrt{V_2^2 + V_3^2 + V_4^2 + ... + V_n^2}}{V_1} \tag{3.18}$$

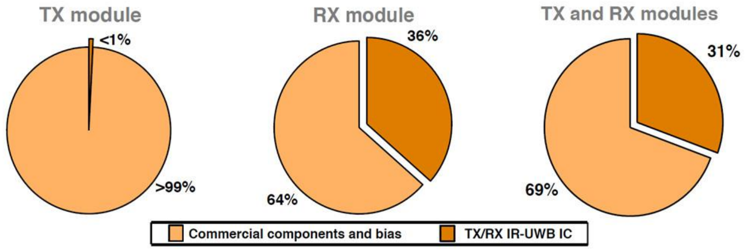

FIGURE 3.11: Current consumption breakdown for TX and RC modules and overall TX system. For the RX modules both supply lines ($\pm 3.6\,V$) are considered

.

where V_n is the fundamental frequency component and V_n is the n-th harmonics component. Following the DIN standardization, the Hi-Fi amplifiers have to be characterized with a THD less than 1%.

The Total Harmonic Distortion (THD) of the complete radio system ($\Delta V_{audio,TX}$ to $\Delta V_{audio,RX}$) is evaluated using the TX and the RX modules battery powered at 1 m distance. A sine wave spanning an amplitude in the range 90-200 mV_{pp} is injected through the audio input of the TX module using a general purpose signal generator in the frequency range 100 Hz-10 kHz, and the spectrum of $\Delta V_{audio,RX}$ is evaluated. Figure 3.9 (b) shows measured THD for different $\Delta_{V audio,TX}$ amplitudes and different test frequency. Results show that THD remains delow 1% for signal amplitudes below 150 mV_{pp} slightly exceeding the limit for large signal amplitude and for very low frequency. The THD <1% is a limit aligned to commercial analog wireless headphone sets. The results show that the THD has an increasing trend for large input amplitude and for high audio frequency.

3.6 Discussion

Power consumption is dominated by the commercial components. When battery powered the TX module consumes 1.89 mA current, while RX module consumes 10 mA (2 mA negative supply, 8 mA positive supply) from the Li-ion battery which have a nominal capacity of 100 mA. This results in a playtime og 50 h at the TX and 12.8 h at the RX (limited by the positive supply). When the batteries are charge and at full power (for a measured 3.98 V), this corresponds to 7.52 mW, 32.4 mW power consumption. Figure 3.11 shows the current consumption breakdown of each module subdivided between the IR-UWB transceiver IC and commercial components including voltage regulator (LDO) and bias. The $< 1\%$ slice clearly confirms the advantages in terms of power consumption of PFM-modultated IR-UWB at the TX.

Consumed current is a meaningful metric as other solutions operate with different voltage supply and moreover can be directly related to battery capacity (measured in mAh units). Note that using AAA Alkaline or Ni-MH batteries which have a capacity of about 1000 mAh, the system can provide up to 120 h continuous operation. An equal wireless audio transmitter/receiver based on Bluetooth technology (with a packet-based approach) powered with 3.6 V consumes 110 mA and 40 mA current respectively at the TX and RX module (*Produino XL-DM01 2.4 GHz Bluetooth*), 40 times higher then PFM IR-UWB solution presented in this Chapter.

In terms of signal quality, compared to Infra-Red, the present solution provides better audio quality and higher SNR at similar operation distance orders. The system is then available solution for ultra-low-power audio streaming although pulses low penetrability at GHz-order compared to hundreds of MHz FM radio range, makes it more susceptible to multipath propagation and slow fading, hence suitable only for short range and in particular WBAN applications. The system has been tested both in Line-Of-Sight (LOS) and Non Line-Of-Sight (NLOS) conditions. In NLOS conditions the system operation is unchanged, but channel contributes with a larger path loss reducing the maximum operation distance to 1 m in typical office environments.

In this Chapter the efficiency of the IR-UWB has been demonstrated, proving a alternative to the current short-range wireless solutions for wearable application, with an ultra-low power and reliable wireless communication system.

Chapter 4

IR-UWB Face-to-Face Interaction and Proximity Sensor

Currently, researchers study Face-to-Face (F-to-F) interactions using wearable sensors and smartphones which provide 2 to 5 m proximity sensing every 20 to 300 s. However, studying interaction distance, which is known to impact disease spread, communication behavior, and other phenomenon, has proven challenging. In particular, Smartphones and other portable RF technologies based on Bluetooth, ZigBee and RFID are limited by their inaccurate, impractical ranging capabilities, need for infrastructure nodes and bulkiness. Wearable sensors may address these challenges exploiting the ultra-low power and low-complexity IR-UWB technology. A proof-of-concept of Face-to-Face detector and proximity sensor based on IR-UWB is presented in this Chapter. The objective of the system is to monitor the Doctor-Patient interaction during the hospitalization and, at the same time, to evaluate the proximity. A IR-UWB transmitter (TX) module is connected with a Smartphone (e.g. of the doctor) and generates UWB pulses at a fixed frequency. An asynchronous IR-UWB receiver (RX), attached to the hospital bed, encodes the signal frequency and evaluates the TX-RX distance exploiting the Pulse Error Rate of the IR-UWB communication. The RX board is stacked with a programmable microcontroller with WiFi module built-in board which allows a seamless connection with the hospital WiFi infrastructure. A custom user-interface reads the data streamed via WiFi, counts the Doctor-Patient interaction and shows in real time the amount of proximity. The TX draws 1.9 mA from the smartphone battery (3.7 V 2000 mAh) while the RX system consumes 3 mA and $250\,mA@3.3\,V$ from the IR-UWB shield and MCU-WiFi module, respectively. UWB TX/RX chipset operate at 3.5 GHZ center frequency and 1.2 V supply. The IR-UWB proximity sensor requires no phase-locking and no-pairing procedure improving seamless current wearable/portable sensors and power usage. The system is able to sense, without delay, the interaction distance with an accuracy of

3 cm and a limited power budget. Once proved the benefits of the system, a new PCB re-design provides a better integration with a wearable/portable system.

4.1 Introduction

The control of hospital-acquired infections and the development of appropriate strategies to reduce their human impact and related economic burden are currently major public health priorities. Reaching these objectives is however hampered by the limited empirical knowledge available to identify the key factors responsible for shaping the spreading behaviour of such infections in the hospital community (Isella et al., 2011).

The knowledge of contact patterns among individuals is of paramount importance in the control of infections transmitted from person to person. In hospital environment patterns of transmission of infections can be studied using data on contact patterns. However, it requires high-resolution information both at the spatial and temporal level to accurately characterize the interactions among individuals with a non-obtrusive technology (Huang et al., 2014). The lack of such information has so far limited the guidelines on preventive strategies for the epidemiology of hospital acquired infections. Mostly, general and qualitative recommendations cannot take into account the characteristics of patients, procedures, hospital wards, structures and logistics and the related heterogeneities across diverse hospital settings (Organization et al., 2002). It is important to note that Face-to-Face (F-to-F) interaction does not demand an absolute position but rather requires a determination of proximity (Cattuto et al., 2010).

Traditionally, F-to-F interactions are studied via surveys and other forms of self reporting. Currently, the two most popular technological solutions are Bluetooth scanning smartphones (Liu, Jiang, and Striegel, 2014) and wearable RF/RSSI scanning sensors (Forys et al., 2013). These technologies give access to proximity patterns and allow the collection of data on specific structural and temporal aspects of social interaction patterns (Golder, Wilkinson, and Huberman, 2007; Eagle and Pentland, 2006; Hui et al., 2005). However, the spatial resolution achieved by these techniques is at best of the order of a few meters and, in general, spatial proximity of wearable devices are not necessarily a good proximity for F-to-F interaction.

Pure RF ranging techniques are appealing since a RF channel is often needed as a data link regardless of application. Several smartphone systems sense interactions by using Bluetooth scans to detect neighboring phones. Such systems can sense if two people are within 5 m of each other, but cannot accurately sense interaction distance beyond that (Eagle, Pentland, and Lazer, 2009; Yoneki and Crowcroft, 2014). To conserve battery life, such systems typically provide 5 min temporal fidelity. Some wearable sensor systems use a similar technique, RF scanning, to sense F-to-F interactions in larger groups. For instance, OpenBeacon uses active RFID tags (Huang, Tang, and Shen, 2006) worn like name badges. They are low power and low complex devices used only for discrete interaction monitoring without evaluate the proximity. On the other hand, Irene, WREN (Forys et al., 2013), or TelosB (Angelopoulos, Mouskos, and Nikoletseas, 2011) use wireless power hungry sensors coupled with an external infrastructure. These deployments have reported a range of proximity of 2 m at a 20 s temporal fidelity without an estimation of the distance.

To overcome such issues, the capability of IR-UWB technology can be exploit for F-to-F estimation and proximity measurements at the same time. UWB signaling is especially suitable in this context because it allows centimetre accuracy in ranging, as well as low-power and low-cost implementation (Cardinali et al., 2006). The key-point in Impulse-Radio regards the use of short duration pulses, that from a pure signal theory point of view, occupy bandwidths of several GHz. The use of short duration pulses is particularly advantageous for the transmitters since aggressive duty cycling can be used preserving the battery life. It keeps power amplifiers and oscillators active for very short durations, allowing very low average powers.

Ranging and positioning with UWB technology can be estimated with four main approaches: Time-of-Flight (TOF), Time Difference of Arrival (TDoA), Angle-Of-Arrival (AOA) and Signal-Strength (SS) based systems.

1) TIME-OF-FLIGHT (TOF)

Time-based positioning techniques rely on measurements of travel times of signals between nodes. If two nodes have a common clock, the node receiving the signal can determine the time of arrival (TOA) of the incoming signal that is time-stamped by the reference node. Since UWB signals have very large bandwidths, this property allows extremely accurate location estimates using time-based techniques via UWB radios. Also, 500 MHz order bandwidth pulses permit high resolution ranging thanks to the possible estimation of TOF. This inherent shrinkage in tune and the high resolution signal processing possible on the received signal. Since the achievable accuracy under ideal conditions is very high, clock synchronization between the nodes becomes an important factor affecting TOF estimation accuracy. Hence, clock jitter must be considered in evaluating the accuracy of a UWB positioning system (Denis, Keignart, and Daniele, 2003).

2) TIME DIFFERENCE OF ARRIVAL (TDOA)

In the TDoA measurements, the difference between the arrival times of two signals travelling between the target node and the two reference nodes is estimated. Usually, TOA-based range measurements need synchronization among the target node and the reference nodes. However, TDoA measurements can be obtained even in absence of synchronization between the target node and the reference nodes, if there is synchronization among the reference nodes (Xu, Ma, and Law, 2006; Barton and Rao, 2008).

3) ANGLE-OF-ARRIVAL (AOA)

An AOA-based positioning technique involves measuring angles of the target node seen by reference nodes, which is done by means of antenna arrays. To determine the location of a node in a two-dimensional (2-D) space, it is sufficient to measure the angles of the straight lines that connect the node and two reference nodes. However, this approach is not suitable for UWB positioning since use of antenna arrays increases the systems cost, annulling the main advantage of a UWB radio communication (Taponecco, D'Amico, and Mengali, 2011).

4) SIGNAL-STRENGTH (SS)

Relying on a path-loss model, the distance between two nodes can be calculated by measuring the energy of the received signal at one node. Currently, some studies have used the received signal strength indicator (RSSI) reported by many radios to estimate range. However, for wearable application the effective irradiated power from body-worn radios can be significantly different and much more dynamic than simple models would suggest, due to absorption, attenuation, reflection, and shadowing. Even in relatively static conditions, RSSI ranging is only accurate to within 2 m (Gigl et al., 2007; Crepaldi et al., 2014).

In this Chapter, a face-to-face (FtoF) doctor-patient interaction and distance estimation based on IR-UWB for hospital application is presented. The distance estimation approach is based on the sensitivity of the RX module and, in particular, on the Pulse Error Rate characteristic. At the TX, a fixed frequency square signal, triggers the generation of UWB pulses. Then, the RX toggles the digital signal every time a new pulse is received within a precise distance limit. Beyond such limit, the RX begins to miss pulses and it does not toggle in absence of an event trigger . A complete transmission of the information provides a F-to-F event within a range limit. Then, further this limit, the number of pulses missed is proportional with the TX-RX distance. The advantages of this approach are:

- the ultra low-power consumption and the small PCB size, especially relevant for the TX module connected with a portable device (e.g. smartphone);

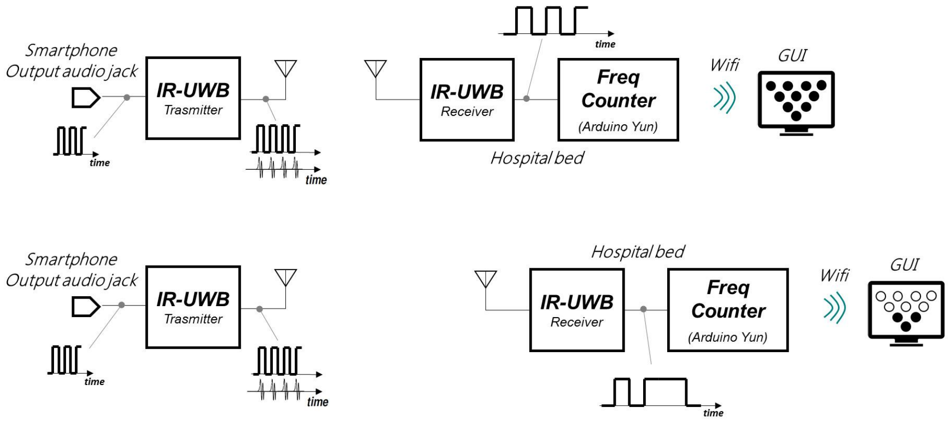

FIGURE 4.1: IR-UWB F-to-F interaction and distance evaluation system.

- the FtoF interaction coupled with a proximity sensor;
- the absent of an external infrastructure.

The system enables the transmission of analog information based on a pulse-based and fully asynchronous wireless link, hence enabling at the transmitter side significant power savings compared to standard wireless communication systems. Asynchronous Line-Of-Sight (LOS) over-the-air measurements obtained with an integrated all-digital transmitter shows a maximum sensitivity of 3 cm TX-RX separation.

4.2 IR-UWB Proximity Sensor System Architecture

Figure 4.1 shows the system approach used to evaluate the TX-RX interaction and relative distance. The TX module, without an embedded oscillator may be connected with the audio jack output of a smartphone. A very simple wave generator App generates a square wave signal at a fixed frequency that is directly connected with the IR-UWB TX module. As shown in Chapter 3, the signal input triggers the generation of UWB pulses and in particular, a 30 pJ energy pulse at 3.5 GHz with a bandwidth of 500 MHz every time a rising edge is received. Therefore the TX module consumes only when a pulse is received reducing the power consumption.

Then, the UWB RX shield includes an interference-robust integrated chipset and it is able to encodes the information toggling the digital signal when a new UWB pulse is received.

The IR-UWB RX is connected with a commercial prototyping board which hosts an AVR microcontroller (MCU) based on the ATmega32u4 built-in with a WiFi module (*Arduino Board Yun*). The board reads the digital signal with a General Purpose Input/Output (GPIO) of the MCU; the

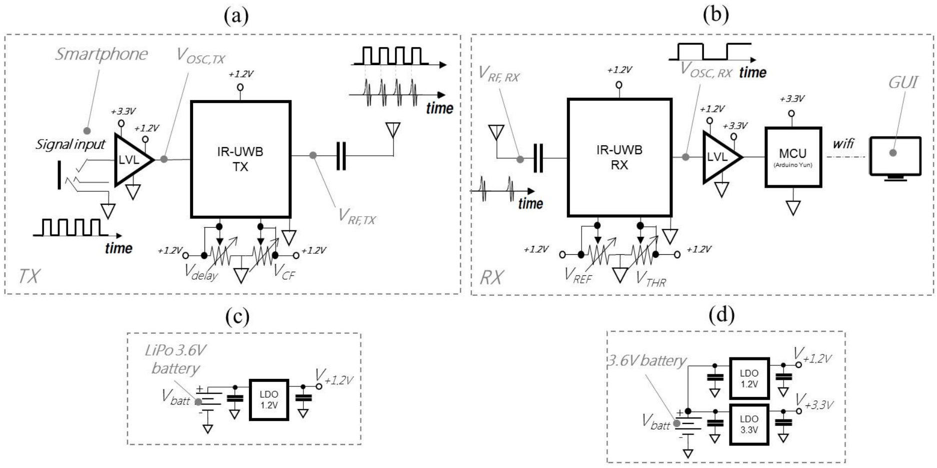

FIGURE 4.2: IR-UWB F-to-F interaction proximity sensor TX-RX block schemes.

firmware counts how many pulse per second are received and transmits the information via WiFi to a custom user interface (wrote in C#, see source code in Appendix) able to manage the WiFi communication and to show graphically the TX-RX distance. Different thresholds are correlated with different Pulse Error Rate levels. They allow to evaluate the amount of the distance and each of them is graphically represented by a LED stripe that, following an overrun of the threshold, they switch on. The TX and RX IC has the same properties explain in Chapter 3.

4.3 Demonstrator Proximity Sensor System

Figure 4.2 shows the block scheme of the transmitter and the receiver modules. Both use 3.6 V rechargeable Lithium-Polymer (LiPo) batteries with 1000 and 2300 mAh respectively. The transmitter module comprises a linear voltage regulator (LDO TPS71712) to generate 1.2 V for the integrated transmitter (Figure 4.2 (c)). The input square signal, coming from the audio wave generator, is applied to the TX board and a FXLP34P5X level shifter adapts input to the UWB IC. Before the UWB chip antenna connected to the IC, a single 0603 10 pF DC block capacitor in included at the radio frequency input. The center frequency f_c and the pulse duration can be adjusted with analog trimmer connected to the V_{CF} and V_{DELAY} pins on the TX UWB IC.

The pulse generation is triggered every,

$$\{t_i | c(t) = V_{DDC(t)} > 0\} \tag{4.1}$$

where $C(t)$ is a periodic signal. Hence the UWB signal $u(t)$ at the antenna output $V_{RF,TX}$ is, $s(t) = \Sigma_{i=-\infty}^{+\infty} u(t - iT)$ where $1/T = f_{TX}$.

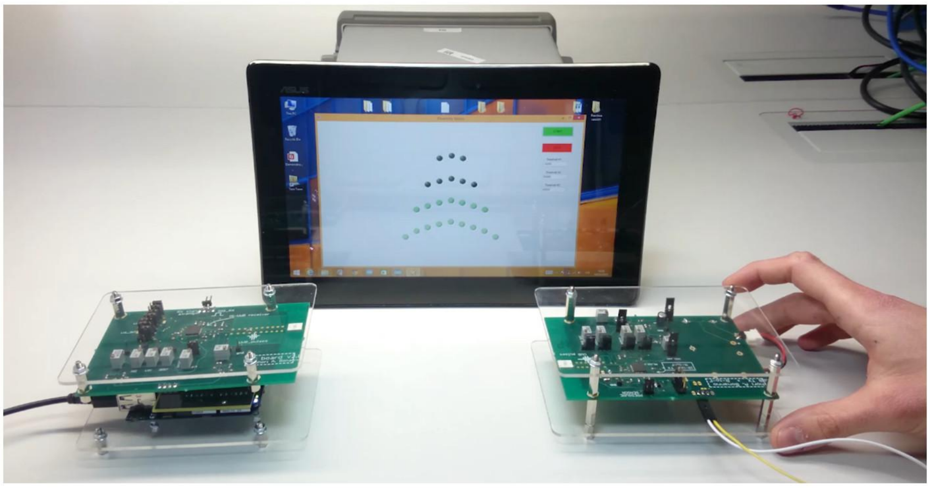

FIGURE 4.3: TX and RX IR-UWB boards with the custom GUI

At the RX the RF signal from the front-end is AC coupled to the baseband. The front-end AC response has wideband $B_W = 270\,MHz$, as reported from a previous scientific work (Crepaldi et al., 2014).

The RX system (Figure 4.2 (b)) comprises the UWB RX shield stacked with a MCU-Wifi programmable module. The battery powered the both MCU-Wifi board and the UWB-shield with a dedicated 1.2 V fixed voltage regulator. The information received is adapted w.r.t. the digital voltage range of the MCU (digital $V_{L,input}$ and $V_{H,input}$). The MCU counts the number of pulses received per second and compares the results with the known fixed TX signal frequency (see MCU source code in Appendix). Through a TCP/IP protocol, the information is streamed via WiFi to a custom standalone user interface able to:

- open a TCP communication (TCP/IP socket);
- read and convert the data into a string variable;
- compare the values with pre-set and adjustable thresholds;
- show the TX-RX (or Doctor-Patient) proximity with graduated LED stripes
- count the F-to-F events.

As results, Figure 4.3 depicts two UWB demonstrator boards used for the tests of the reliability of the system. In background, a portable system with the custom GUI shows in real-time the results. The TX and RX demonstrators are boxed between two $plexiglass$® layers and they occupy $12 \times 8\,cm$ including the flat batteries placed on the bottom of the PCB.

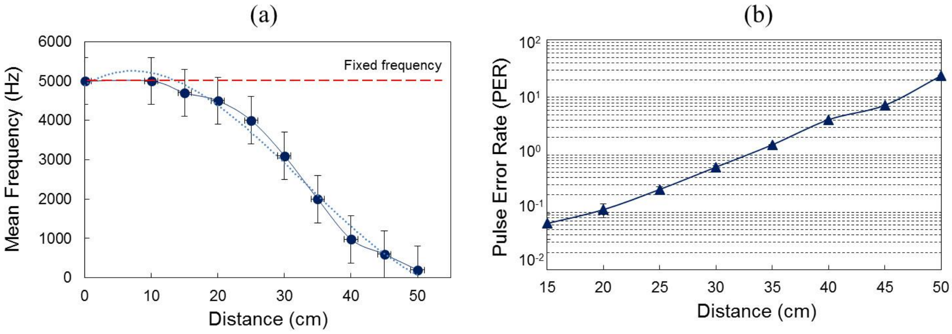

FIGURE 4.4: Experiment of TX-RX distance evaluation. (a) Frequency variation and (b) Pulse Error Rate at different distances.

4.4 Experimental Measurements

During measurements, both modules are powered with the LiPo batteries and no further devices are included with the PCBs. As describe in Chapter 3, the integrated RX is powered with a ranges of $0.9 - 1.2\,V$ and in the over-the-air measurement sessions the integrated TX in Crepaldi et al., 2012 has been set to generate pulses at a center frequency of 3.5 GHz with bandwidth ranging 300 MHz−500 MHz, to match the FCC definitions. The RX was set to the same f_c of the TX. Two identical oscilloscope probes, same length, corresponding to two separate channels, are connected to transmitter trigger $V_{OSC,TX}$ and received signal $V_{OSC,RX}$ respectively. The RX is powered with an battery and the output frequency is captured with an Agilent DSO9404A 4 GHz 20 GS/s oscilloscope. Positive-to-positive edge measurements are run 1 kS points.

Figure 4.4 (a) shows a one-dimensional mean frequency variation for 1 cm interval distance up to 50 cm. Below 15 cm the digital signal can be transmitted with relative standard deviation below 0.1% until 5 kHz, and below 1% for frequency $\leq 1\,MHz$ (frequency excluded since too high for a smartphone wave generator App (max $f_{OSC} = 20\,kHz$).

Figure 4.4 (b) depicts the Pulse Error Rate (PER) in y-axis log format in relation with the TX-RX relative distance. Eq. 4.2 expresses the PER equation. This result was carried out through the C based algorithm flashed within the MCU. It is capable to count the pulse receive with an error of 0.5% (around 10 Hz at $f_{OSC} = 5\,kHz$) and encode the distance with a resolution of $\sim 3\,cm$.

$$PER = \frac{Number\,of\,RX\,error\,pulses}{Total\,number\,of\,TX\,pulses} \tag{4.2}$$

TABLE 4.1: Comparison with Commercial Products.

	This work	*PulsON 410®*	*DecaWave DW1000*	*Ubisense 7000*	*PLUS Location System*
Method	PER	TW-TOA|CRE	TOA	AOA|TDoA	TOA
Ranging Accuracy (cm)	5	2	10	15	100
Range (cm)	50	4000	300	N.a.	N.a.
Central frequency (GHz)	3.5	4.3	3.5	6-8	6.6
Bandwidth (MHz)	500	2200	900	N.a.	N.a.
Power consumption (mW)	10.8 (TX), 900 (RX+WiFi)	4000	N.a.	3000	N.a. (TX) 1500 (RX)
Size (cm^3)	450 (TX), 480 (RX)	115	150	1820	15.4

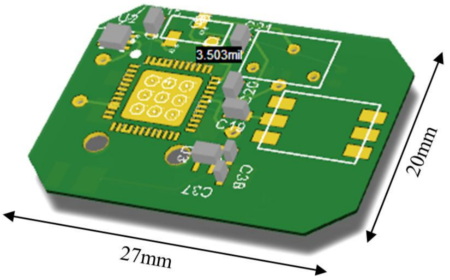

FIGURE 4.5: 3D model of the new version of IR-UWB TX ranging system

4.5 Discussion

Table 4.1 compares the system performance w.r.t. commercial products based on IR-UWB chipset operating at the same frequency range 3.1−10.6 GHz. Consumed current is a meaningful metric as other solutions operate with different voltage supply. The system presented can provide up to 8 h in continuous operation with a small LiPo capacity of about 120 mAh, thanks to the ranging method adopted.

The relevant benefits of the system proposed in this Chapter in comparison with the State-of-the-Art are:

- the low complexity and ultra-lower power consumption of the TX device, ideal for wearable/portable application;
- the range of application (15 cm) and the 2-D spatial accuracy (3 cm) in accordance with the F-to-F interaction purpose;
- the simultaneous function of F-to-F interaction and proximity estimation.

In the end, the TX system can be significantly improved in terms of integration through an advance double layers PCB routing proposed in Figure (4.5) with a surface area only $5.4\,cm^2$. With this size, the TX module can be connected with a smartphone. Furthermore, adopting an electronic oscillator able to generate a fixed frequency (e.g., Timer 555 in astable mode) the small transmitter can be attached or embedded within a normal cloth.

Chapter 5

Wearable Soft Actuators - EAPtics project

A tremendous variety of devices used today rely on actuators of one sort or another to convert electrical energy to mechanical energy. Conversely, many power generation applications operate by converting mechanical action into electrical energy. Promising recent developments in material processing, device design and system configuration have enabled the scientific and industrial community to focus their efforts on the realisation of smart textiles. In fact, all components of interactive electromechanical systems (sensors, actuators, electronics and power sources) can be made from polymeric materials, to be woven directly into textile structures (sensing and actuating micro-fibres) or printed or applied onto fabrics (flexible electronics). In particular, intrinsic sensing, actuating, dielectric or conductive properties, compliance, lightness, flexibility and the relative low cost of many electroactive polymers (EAP) make them potentially suitable materials for the realisation of such systems. Current EAP actuator sheets or fibers perform reasonable well in the centimeter and mN range, but are not practical for larger force and deformation requirements. In order to make EAP actuators technology scalable a design methodology for polymer actuators is required. Design variables, optimization formulas and a general architecture are required, as it is usual in electromagnetic or hydraulic actuator design. This will allow the development of large EAP actuators specifically designed for a particular application. It will also help to enhance the EAP material final performance. This approach is not new, it is found in Nature. Skeletal muscle architecture has a profound influence on muscle force-generating properties and functionality. Based on existing literature on skeletal muscle biomechanics, the Nature design philosophy is inferred. Formulas and curves employed by Nature in the design of muscles are presented. Design units such as fiber, tendon, aponeurosis, and motor unit are compared with the equivalent design units to be taken into account in the design of EAP actuators. Finally, a complete design methodology for the design of actuators based on multiple EAP fiber is proposed. In addition, the procedure gives an idea of the required parameters that must be clearly modelled and characterized at EAP material level. The solution proposed was patented and extended at European countries (Stoppa and Freni, 2015).

5.1 Introduction

In order to endow fabrics with motor functions, flexible actuating devices are needed. They share with sensors the necessity of overcoming several technological problems in order to allow textile implementations. Multifunctional electroactive fibres and fabrics will give the traditional textile industry a new additional value, the possibility of making daily life healthier, safer and more comfortable, bringing technological advances closer to the public through the use of easy-to-use interfaces between humans measuring devices and actuators.

The most noticeable challenging issues include the identification of efficient principles of operation and suitable configurations, selection of high-performance materials, and implementation of custom fabrication processes. Fabrics with shape-recovery capabilities have been developed (Carosio and Monero, 2004). Despite this, no success in embedding effective and comfortable actuating functions into textiles has been substantially reported so far.

Electroactive polymers are usually divided into two principal classes, according to their actuation mechanism: ionic EAPs and electronic EAPs. The first group relies on electric activation mediated by charge carriers, i.e. ions and/or molecules, while materials belonging to the latter group respond to the stimulation of an electric field. When the triggering mechanism depends on the diffusion of relatively bulky chemical species, the rate of response is slowed down. Consequently, the actuation speed of ionic EAPs is much slower, compared to electronic EAPs: this is their major drawback. On the other hand, smart polymers actuated by electric fields are able to apply relatively small forces and require very high voltages.

In particular, the attention was focused on Electroactive Polymers (EAPs): these polymeric materials work as transducers, converting electrical inputs into mechanical outputs, and vice versa. They show features that cannot be traced in other traditional functional materials (e.g. piezoelectric ceramics), such as large active strains, high energy density, mechanical compliance and flexibility, very low weight, zero noise emission, simple and scalable structures and tailorable properties. All these characteristics make EAPs the actuation system closest to natural muscles (Brochu and Pei, 2010; Carpi et al., 2011b). Despite the first awareness about the potentialities of Electroactive Polymers may be traced back to 1880, just nowadays this technology is moving from academic laboratories to industrial production and commercialization. Therefore, EAPs represent the cutting edge in the context of functional materials (Carpi et al., 2011b; Bar-Cohen, 2002).

A brief look at some electroactive polymers may be useful to get a general picture about the technology and to analyze advantages and drawbacks of different alternatives.

5.1.1 Ionic EAP

Ionic EAPs can be activated, within a surrounding electrolyte medium, by very low voltages (on the order of 1 V). The commonly accepted explanation of the phenomenon attributes the observed deformation to the input/output diffusion of ions (exchanged with the surrounding electrolyte) into/from the polymer sample, driven by the applied voltage. In fact, the voltage produces a variation of the polymer oxidation state, which causes, in order to maintain the global electroneutrality, the necessary modification of the number of ions associated with each polymer chain (doping and dedoping processes) (Bar-Cohen, 2002; Bar-Cohen, 2004). Conducting polymer actuators typically exhibit active strains on the order of 1%-10%, high active stresses (up to tens of MPa), and low driving electrical potential differences (order of 1 V). Nevertheless, the use of conducting polymers as actuators is typically limited by their short lifetimes and high response times. Polyelectrolyte gels (Shiga and Kurauchi, 1990), ionic polymer-metal composites (IPMCs)(Punning, Kruusmaa, and Aabloo, 2007), conducting polymers (Osada and De Rossi, 2013), and carbon nanotubes (Mirfakhrai, Madden, and Baughman, 2007) are examples belonging to the Ionic EAP.

5.1.2 Electronic EAP

On the contrary, electronic EAPs require typically high driving voltages (electric fields on the order of 10-100 V m for electrostrictive polymers and dielectric elastomers). However, progress concerning the reduction of their driving fields is currently occurring. Electronic EAPs show, in comparison with the ionic ones, lower response time and higher efficiency, stability, reliability, and durability. Piezoelectric polymers (Baughman, 1996), electrostrictive polymers (Liu et al., 2005), ferroelectric liquid-crystalline elastomers (Lehmann et al., 2001), and dielectric elastomers (Carpi et al., 2011a) are electronic EAPs.

In order to describe the potential applicability of EAP-based actuators to electronic textiles, the most highly performing material are the Dielectric Elastomers.

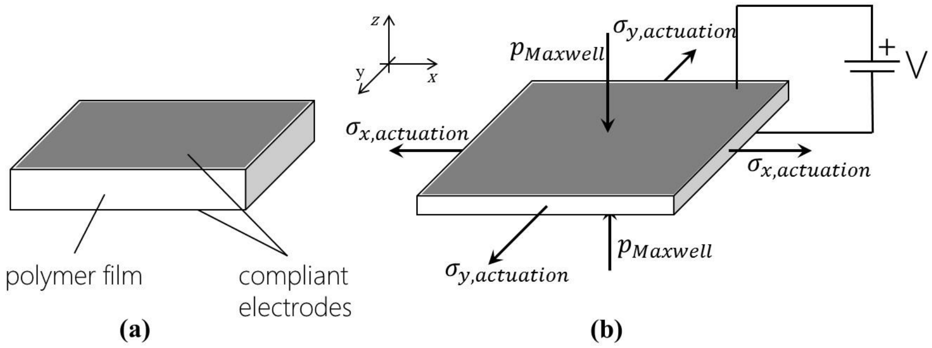

FIGURE 5.1: Dielectric Elastomer working principle. (a) Structure of the DE. (b) Mechanical deformation when a voltage is applied.

5.2 DE Modelling

Dielectric Elastomers (DE) represent the EAP class with the highest achievable active strains (order of 100%), as well as considerably high active stresses (up to 1 MPa) (Pelrine et al., 2000). They consist of insulating rubbery polymers, having a low elastic modulus. When a thin film of such materials is sandwiched between two compliant electrodes (e.g., made of carbon conductive grease), and a high voltage difference is applied between them, the polymer undergoes an electric field sustained deformation, consisting of a thickness squeezing and a related surface expansion (Pelrine et al., 2000; Pelrine, Kornbluh, and Joseph, 1998). The achievable large deformations are mainly due to a Coulombian effect, established by means of the electrostatic interactions occurring among free charges on the electrodes.

The resulting effect on the elastomer is a net contraction in thickness and a planar expansion (Figure 5.1). The excellent figures of merit possessed by dielectric elastomers in several respects (high actuation strains and stresses, fast response times, high efficiency, stability, reliability, and durability) make them the most highly performing materials currently available for polymer actuation. The price for achieving these high-level capabilities is represented by the high driving electric fields required (order of 100 V m). Thus, the actuation voltage can reach order of kV, but the capacitive nature of the solution guarantees little currents ($100\mu A - 1\,mA$) and, therefore, very low power consumption.

Both silicone rubbers and acrylic elastomers are used as dielectric elastomers. Furthermore, applying a prestrain to the material, efficiency can be highly improved and preferential actuation in one direction can be realized (Brochu and Pei, 2010).

Based on the principle of operation, two directions are possible to perform work against external loads.

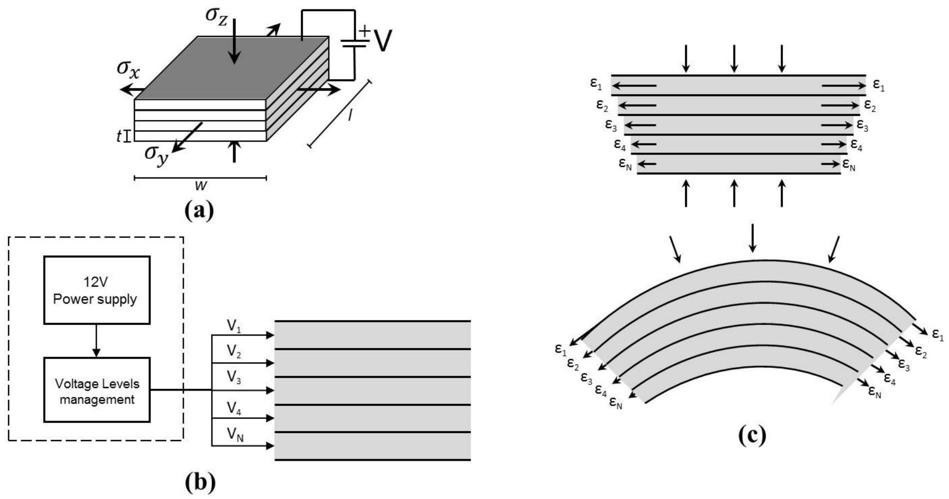

FIGURE 5.2: (a) Dielectric Elastomer multilayer design. (b) Voltage differentiation for each layer. (c) DE deformation according to the voltage applied.

- Work in the planar directions (expanding actuator): under electrical activation of a DE basic unit the film expands in the x, y plane and can thus work against external pressure loads in both planar directions x and y;
- Work in the thickness direction (contractile actuator): under electrical activation the electrodes squeeze the DE film in the thickness direction (z). Thus, the actuator can work against external tensile loads acting in the direction of the electric field lines of the compliant capacitor.

Many configurations for dielectric elastomer actuators have been proposed and demonstrated, including planar, tube, roll, extender, diaphragm, and benders (Ashley, 2003; Carpi and Rossi, 2005; Rosset and Shea, 2013; Chakraborti et al., 2012). Tube, and mainly, roll actuators are flexible devices potentially suitable to endow fabrics with linear (along a line) actuation functionalities. These actuators can elongate under electrical stimulation.

5.2.1 Multilayer design

The dielectric material can be reasonably assumed to be incompressible, therefore, $l \cdot w \cdot t = cost$ where l is the length, w the width and t the thickness of a single the dielectric layer. Or alternatively

$$(1 + s_x)(1 + s_y)(1 + s_z) = 1 \tag{5.1}$$

where s_x, s_y and s_z are the strains (it has been used s to not confuse with the dielectric constant ε) in the three directions. The electrostatic stress generated across the electrodes is the Maxwell pressure, described by:

$$p = \varepsilon_r \cdot \varepsilon_0 \cdot E^2 \tag{5.2}$$

where ε_r is the material relative dielectric constant, ε_0 is the vacuum dielectric constant and E is the applied electric field. Furthermore, the previous equation can be written as a function of voltage V and dielectric thickness t:

$$p = \varepsilon_r \cdot \varepsilon_0 \cdot \left(\frac{V}{t}\right)^2 \tag{5.3}$$

Taking into account the hypothesis that the dielectric material linearly elastic and isotropic (with a Young modulus Y) the thickness strain is given by:

$$s_z = \frac{-p}{Y} = \frac{-(\varepsilon_r \cdot \varepsilon_0 \cdot E^2)}{Y} = \frac{-(\varepsilon_r \cdot \varepsilon_0 \cdot (V/t)^2)}{Y} \tag{5.4}$$

For a definite polymer thickness, order of 100 V m electric field can be reached by applying high voltages, which may have disadvantages in many applications. In order to reduce the driving electric fields, polymers with a high dielectric constant (or permittivity) are necessary. In fact, according to the Eq. 5.3, the strain generated by a dielectric elastomer actuator is proportional to both the square of the applied electric field and the material dielectric constant (Pelrine, Kornbluh, and Joseph, 1998).

Considering a repetition of this planar structure in a stackable format, the multilayer structure resulted is made of N active layers. Figure 5.2 depicts an example of a multilayer geometry. Each layer performs a different linear elongation, so that $s_N > s_4 > s_3 > s_2 > s_1$. The resulting actuation is both a linear expansion along the x axis and a bending along the y-axis.

According to the equation 5.3, the planar strain along the polymeric dielectric increases with the bias applied and, therefore $s_N > s_4 > s_3 > \varepsilon_2 > s_1 \Leftrightarrow V_N > V_4 > V_3 > V_2 > V_1$.

Different voltage levels for different layers allow a fine control of the actuation, in terms of magnitude and direction of the deformation. Furthermore, thanks to superposition principle, the multilayer configuration allows to reduce of one order of magnitude the voltage applied (300-400 V). Notwithstanding the high voltage, the current is very low, around $10\mu A$.

5.2.2 Coaxial design

In order to endow fabrics with actuating functions, fiber-shaped actuators may be particularly useful. At the end of the 1990s, conducting polymer

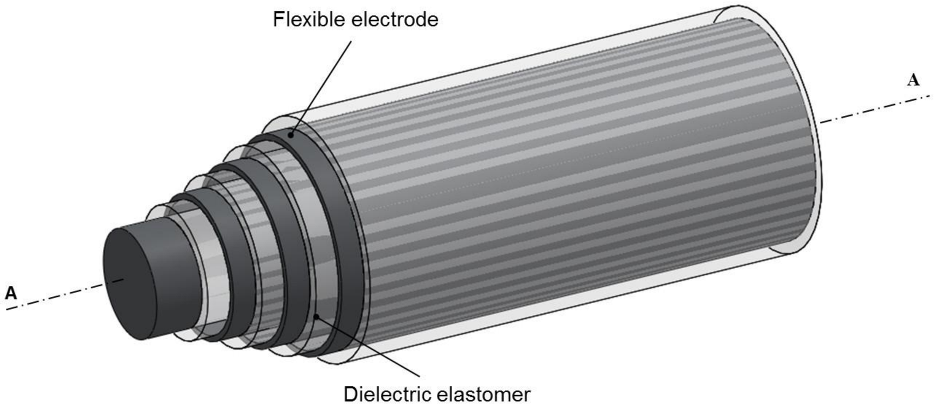

FIGURE 5.3: Dielectric Elastomer coaxial design.

fiber actuators was represented (Mazzoldi et al., 1998) obtaining a fiber-like structure have shown strains of about 0.3% and active stresses of about 3 MPa, for driving voltages lower than 1 V. However, the deformation of a conducting polymer was strongly anisotropic, with a deformation along the radial size, making the fibers not suitable for practical usage. Figure (5.3) shows the solution proposed which exploits the advantages of the multilayer geometry and turns them into a coaxial configuration. A coaxial structure allows to design fiber-actuators that can be endow within a fabric. As mentioned above, different voltage levels act different EAP layers obtaining a fine control of the final deformation along the axial direction. Furthermore, the coaxial solution leads in terms of energy stored, improving the efficiency in compare with a planar geometry. Since the EAP configuration can be approximated to a parallel-plate capacitor, its capacitance (C) is

$$C = \varepsilon \frac{S}{t} \tag{5.5}$$

where ε the dielectric constant, S the surface are of the plates d is the distance between the them. Therefore the energy stored (W) is

$$W = \frac{1}{2} C V^2 = \varepsilon \frac{S}{2d} V^2 \tag{5.6}$$

As described in Eq. 5.6, the energy stored is directly proportional with the surface area (S) and with the square of the voltage (V). Moreover, it is inversely proportional with the plates distance (d), in our case the thickness (t) of the dielectric elastomer. The coaxial approach leads relevant benefits in terms of energy efficiency and force generated. This is confirmed from the fact that, at the same volume (Figure 5.4), a planar geometry has always a smaller surface area then a cylinder ($l^2 < \pi l^2$). In particular the Eq. 5.7 demonstrates analytically this assumption with a multyplanar and coaxial

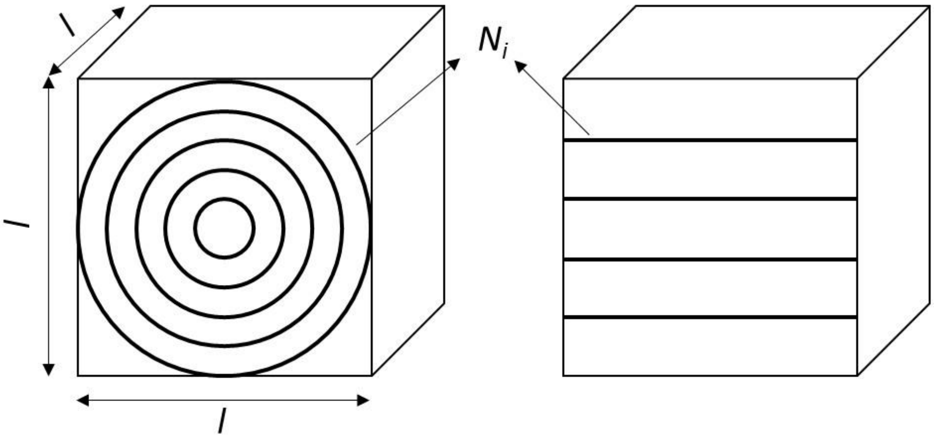

FIGURE 5.4: Comparison of coxial and planar architecture. The geometry are inscribed within a cube with the same volume and number of layers.

architecture. Figure 5.5 shows the final actuation result of a single EAP coaxial fiber.

$$\begin{aligned} S_{i,p} &= l_i^2 \\ S_{i,c} &= \pi d_i \cdot l \end{aligned} \tag{5.7}$$

where d is the diameter of the cylinder, $S_{i,p}$ and $S_{i,c}$ are the $i-th$ surface area of a plane and a cylinder, respectively. Considering an equal number of layers (N) and coaxial cylinder inscribed within a cube with the same volume, the sum of surface areas $S_{N,p}$ and $S_{N,c}$ are respectively

$$\begin{aligned} S_{N,p} &= l_i^2 \cdot N \\ d_i &= l - (i-l) \cdot \frac{l}{N} \\ S_{N,c} &= \sum_{i=1}^{N} \pi l^2 \left[1 - \frac{i-1}{N}\right] \end{aligned} \tag{5.8}$$

By solving the series $S_{N,c}$, the initial assumption is demonstrated as follows

$$\begin{aligned} S_{N,p} &< S_{N,c} \\ l^2 N &< \pi l^2 \left[N - \frac{N-1}{N}\right] \end{aligned} \tag{5.9}$$

where the inequation is always respected for $N > 1$.

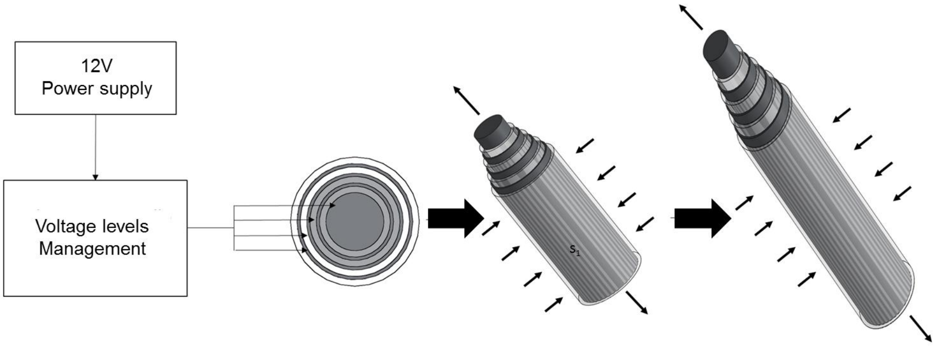

FIGURE 5.5: EAP coaxial fiber activation with a voltage differentiation.

The result is a resizing of the device and an increase of the force generate, following by the Eq. 5.4.

Considering the coaxial principle and investigating into the skeletal muscle architecture, the hierarchical structure of the muscle fibers can be approximated as a whole of EAP coaxial fibers able to generate a movement in response to electrical stimulus. Figure 5.6 enables to compare the muscle structure with a multi-fibers coaxial EAP. Taking into account the chance to activate individually each fiber with different potential, the "muscle hierarchical selective recruitment principle" can be mimicked. This allows to obtain the following advantages:

- to adjust the force produced;
- to control the direction of the deformation;
- to further reduce of the tension applied.

5.3 Control Circuit and Proof-of-Concept

The electroactive polymers need high voltage to be activated, typically in the order of $3 - 5\,kV$. The use of passive components such as resistors and capacitors has been suggested as a method for simple and inexpensive coupling of electrical and mechanical response of the actuator (Pelrine et al., 2008). The aim of the circuit proposed is to test the possibility of controlling the polymer actuator layer at different voltage with an AVR microcontroller. The circuit consists of four blocks:

- a variable power supply provides stable voltage 0-12 V and current of 125 mA for the high voltage converter;

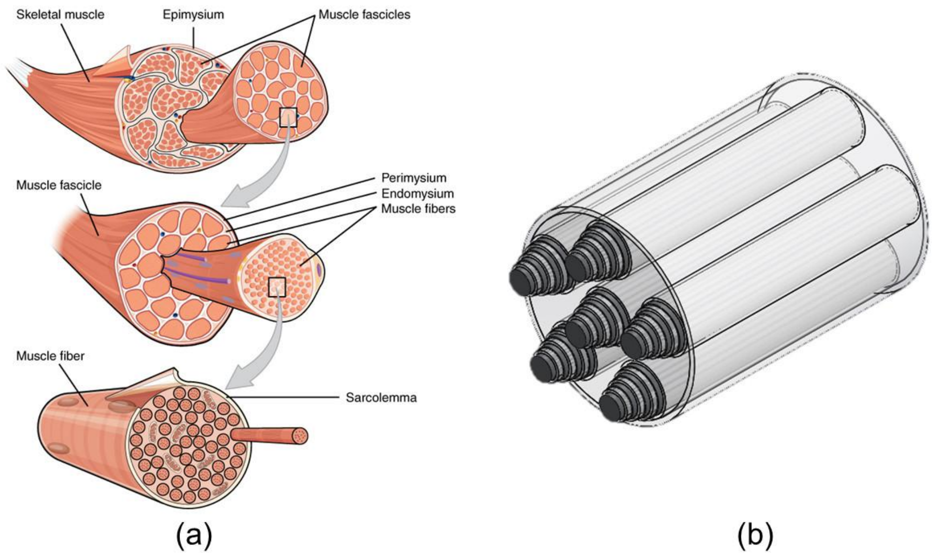

FIGURE 5.6: (a) Muscle hierarchical structure. (b) Multi-fibers coaxial EAP

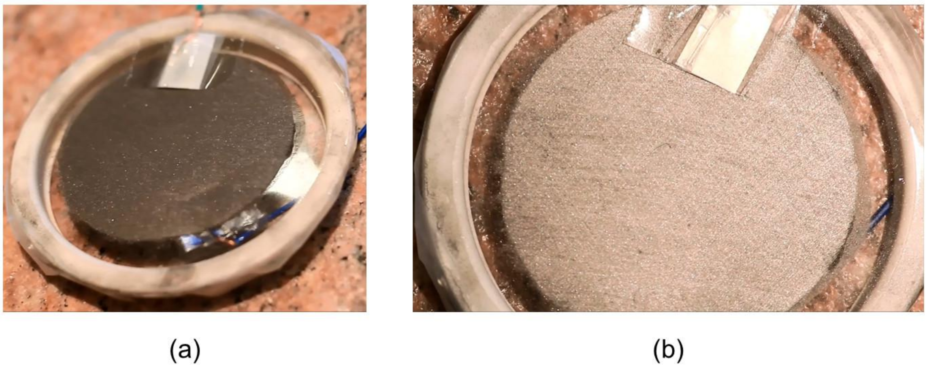

FIGURE 5.7: EAP proof-of-concept.

- an AVR microcontroller and digital potentiometer MCP4131 adjust the behaviour of the actuator. Digital potentiometer has a range of 128 values;
- a commercial high voltage DC/DC converters (Series GMA Itek Power High Voltage DC-DC converter) converts incoming voltage of 0-12 V to high voltage (0-3 kV);
- five voltage dividers provide different high voltage output, from 3 kHz to 50 V.

The high voltage DC to DC converters provides an output voltage available in the range 100 V to 3 kV with a input of 1-12 V range and a maximum output power of 1.5 W.

The test of the electronic circuit was performed using a single EAP layer (thickness of $100\mu m$) based on VHB 3M acrylic silicon material and monitoring the behaviour. Initially the VHB was pre-stretched and attached on a rigid frame. Then, thanks to the adhesive property of the material, the flexible electrodes was made with a deposition of micro-particles of graphite on both sides. Finally, two copper connectors attached with carbon grease to the electrodes allow the electrical connection with the circuit. Figure 5.7 shows the EAP proof-of-concept able to change the diameter size of $1\,mm\,kV$. The system was tested with different voltages adjusted with both the digital potentiometer and the voltage dividers. The DC-DC high voltage converter has shown a linear input-output characteristic, however q.e.d. the material does not change its shape with a voltage lower than 1 kV. Another aspect monitored was the time relaxed that resulted around 100 ms, mainly due to the elastic recovery of the material.

5.4 Discussion

A new concept of the EAP geometry inspired by the muscle architecture and a proof-of-concept of the EAP working principle based on dielectric elastomer has been presented in this Chapter. A deep analysis of the EAP multilayer configuration, well known among the scientist community, in addition to the application of different voltages for each layer, lead relevant improvements within the soft actuator technology. A fine control of the deformation and lower voltage applied in compare with the literature are part of these improvements. Since an excessive increase in the number of layers can lead to a stiffening of the actuator, the coaxial geometry aims to solve this issue. Increasing the surface area of the electrodes, a performance improvement is obtained without affects the mechanical properties of the material. Furthermore, a coaxial structure allows to develop active fibers, which can be potentially woven within a fabric and fill the gap of the wearable man-machine interface. This solution was patented and brought to a further level of innovation, taking inspiration from the natural muscle anatomy. In principle, a multi-fibers coaxial configuration would allow further improvement of the EAP fibers performance introducing the change to control the strength and movement of the fiber with a selective activation of the fibers, as it happens for the muscle fibers.

Despite these promising improvements, there are several challenges to overcome, from material, electronic and integration point of view. Firstly, the material selection has be focused on dielectric elastomers with a lower anisotropy and lower ε_r value in order to increase the electrostatic effect. Furthermore, together with a reduction of the layers thickness the driving voltage can be reduced, reaching voltages used normally with the electronic

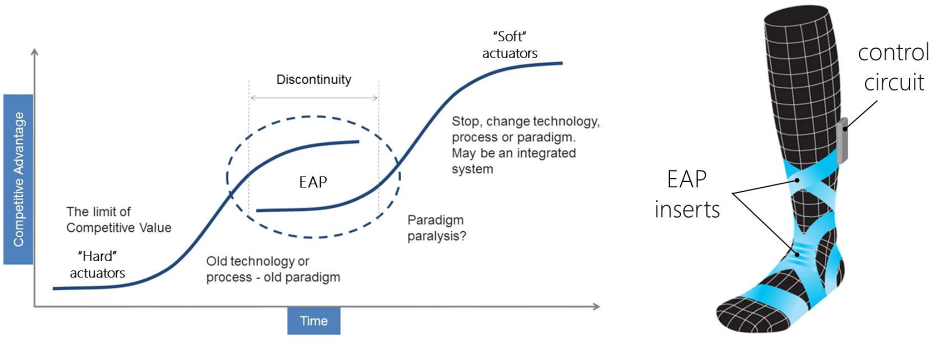

(a) (b)

FIGURE 5.8: (a) EAP technology trend in compare with the traditional "hard" actuators. (b) Active compression stockings concept.

consumer. Besides, with lower driving voltage, the overall size of the electronic circuit can be reduced.

Another issue is the material-circuit interface through metallic plates. Actually, the wiring of the flexible electrodes with the electronic circuit is fragile and peak effects generated by the metallic plates can pierce the elastomeric layer. Carbon grease improves the connection of the plates, however is not perfectly stable. Finally another challenge regards the manufacturing processes, in particular for the coaxial configuration. Techniques used to develop optical fibers, mainly based on extrusion processes, have to be studied and evaluated.

Despite these and other challenges (such as improvement of device reliability and efficiency), the integration into fabric of EAP-based actuating, electronic and power functions represent one of the means of having great potentialities for the development of completely wearable electronic textiles. Figure 5.8 (a) depicts graphically the EAP technology trend in compare with the well know traditional actuators devices. Currently, the EAPs are within the discontinuity with lower competitive advantages than the commercial product, but with a promising growth of the technology filling the gap and leading new promising applications.

A further development of the manufacturing processes of the EAP fibers with the optimization presented in this Chapter will allow to fill the existing gap between the mechanical actuator and the human body interaction.

5.5 Application Scenario

The near-future developments of such EAP-based smart-textiles open new challenges. One of them concerns the improvement of the wearability of EAP devices by means of textile-compatible configurations and shapes, preferably in fiber form. This implies the development of device manufacturing processes (extrusion, electrospinning, wet- or dry-spinning, casting, etc.) and textile technologies (weaving, coweaving, knitting, jacquard, coating, printing, etc.) for their integration into fabrics. Nature took million of year to develop the mostly efficient machine: the human body. Taking inspiration from the body anatomy and physiology followed by an smart material and electronic technology improvement, new generation of wearable device will be not so far.

Following a benchmark of the possible technology application, the medical field was selected with aim to propose a solution against the Chronic Venous Insufficiency disease (CVI). In CVI states, venous blood escapes from its normal antegrade path of flow and refluxes backward down the veins into an already congested leg. Venous insufficiency syndromes are most commonly caused by valvular incompetence in the low-pressure superficial venous system but may also be caused by valvular incompetence in the high-pressure deep venous system (or, rarely, both). CVI pathology is the 3^{rd} most widespread cause of death in Europe (Eberhardt and Raffetto, 2014), with 19 mln patients/year. Current solution is to wear compression stockings, static and highly uncomfortable medical device. The therapy is strongly compressed by the refusal to use the compression stockings due to their inconvenience and low efficiency. To tackle these issues, stirrups of EAP actuators can be embedded within the stockings with the following advantages:

- active device against passive traditional stockings;
- adjustable compression according to the actual need of the patient;
- easy fit thanks to the temporary expansion of the stockings size, particularly relevant for elderly patients;

Figure 5.8 (b) shows a possible interfacing of the EAP actuators with the human body anatomy.

Chapter 6

Gravity Loading Countermeasures SkinSuit

Gravity has a profound effect on human evolutionary development, shaping not only its mechanical dynamics but also its supporting mechanisms (White and Averner, 2001; Blaber, Marçal, and Burns, 2010). Despite the use of several countermeasures, significant physiological deconditioning still occurs during long duration spaceflight. The effects on the musculoskeletal system are perhaps the greatest challenge to solve primarily due to the absence of loading in microgravity. Seeking new countermeasures is an on-going priority for long-term space mission programs (Convertino, 1996). Wearable technologies are significant relevant in space exploration research (Cadogan, 2015), as demonstrated from the manifold progresses of the SpaceSuits, a complex wearable systems able to preserve the health of the astronauts during External Vehicular Activities (EVA), and to counteract the effect of the microgravity. A new generation of wearable system, Gravity Loading Countermeasure SkinSuit (GLCS), was used for the first time on the International Space Station (ISS) on September 2015 within the IRISS space mission (Vicente and Walker, 2015). It is a passive garment made with elastic materials able to provide a simulated gravity loading on the body thanks to a bidirectional weave material strain that develops loads cumulatively towards the legs (Waldie and Newman, 2011). This Chapter is focused on the research activities within the GLCS project with the objective to turn the SkinSuit from a passive into an active wearable countermeasures system and to monitor the effects of the microgravity on the spinal column, and thus length, via a novel wearable system. A background of the physiological effects on the human body due to the space environment and the State Of the Art (SoA) of the current countermeasures is presented. Then, Paragraph (6.3) details a proof of concept of an Gz-load control system, coupled with a Load Monitoring (LM) system. Following trials, the load monitoring approach, was succeeded by a superior Stretch Monitoring (SM) system was integrated within the SkinSuit. Finally, this Chapter shall define the Spinal Elongation Monitoring (SEM) system: a proof-of-concept of the first wearable device able to measure the spinal elongation in microgravity conditions.

6.1 Background of the Technology

During spaceflight, the human body is subject to physiological adaptation to the microgravity conditions. Humans are well adapted to living in a 1-G environment, thus the microgravity environment of space can have profound effects on the human body.

Exposure to microgravity, whether simulated or actual, was shown to result in a reductions of the ventricular mass (Eckberg et al., 2010), blood volume (Eckberg, 2003), balance control (Reschke et al., 2009), nervous system sensitivity and reserve (Cooke and Convertino, 2007), arterial tone (Verheyden et al., 2009), bone mass (Lang et al., 2004), immune function (Baqai et al., 2009) skeletal muscle mass (Blaber, Marçal, and Burns, 2010) and lead to development of space motion sickness (Lackner and DiZio, 2006). These changes can lead to operational difficulties and health consequences, both in space and upon return to a gravitational body (including Earth or future missions to the Moon/Mars).

Some of the most profound changes occur in the musculoskeletal system. Bone is a dynamic organ that adapts to the loads under which it is placed. Due to the unloading caused by the microgravity environment during long-duration spaceflight missions, astronauts can lose up to 1-2% Bone Mineral Density (BMD) per month, concentrated in the weight-bearing areas of the skeleton, which is equivalent to the yearly losses observed in post-menopausal women (Stein, 2013; Smith et al., 2014). Astronauts in space lack the normal static loading due to standing in 1 G, but also the dynamic loads caused by impact and muscle activation during movement. Bone loss may be the most important limiting factor for long-term spaceflight, due to the risk of fracture (Bikle, Sakata, and Halloran, 2007; West, 2000).

Similarly, degradation of muscle mass, force and power have been observed (Fitts et al., 2010; Gopalakrishnan et al., 2010). Since muscle contractions are also a major source of bone loading, the loss of muscle power may accelerate bone loss. Astronauts commonly complain of back pain during initial exposure to microgravity, presumably is related to spinal elongation that occurs in the absence of gravity. In fact, approximately 50% of crewmembers reported back pain due to the spine elongation of up to 70 mm (Barratt and Pool, 2008). Spinal elongations also seen on earth after extended periods of lying down, such as during sleep, when the spine can lengthen by as much as 2-3 cm (Styf et al., 1997). Elongation of the spine can affect the fit of space hardware custom-made for astronauts (e.g. EVA spacesuits) such as the launch and re-entry seats made for the Russian Soyuz vehicle (Wing et al., 1991).

6.2 Wearable Countermeasures

Health and fitness procedures and programs are required to mitigate the effects of living in microgravity, and ideally retain Earth-bound baselines. These approaches and related devices are collectively called countermeasures. For more than 50 years, countermeasure solutions have been developed and evaluated during spaceflight, including physical exercise apparatus (Convertino, 1996), nutritional supplement (Smith et al., 2005), compression/loading clothing (Stenger et al., 2010) and artificial gravity concepts (Young et al., 2001). Limitation of efficiency and impractically of current countermeasures to microgravity for new exploration missions require a more thorough understanding of the issues and the development of new solutions (Hargens, Bhattacharya, and Schneider, 2013).

While certain pharmaceutical measures, such as bisphosphonates to prevent bone loss, are being considered, at present the only countermeasure being used to actively address physiological deconditioning is physical exercise (Cavanagh, Licata, and Rice, 2007). Recent evidence shows that current exercise programs using the Advanced Resistive Exercise Device (ARED) are more effective in preventing deconditioning than previous ones, but still exercise alone is not sufficient to completely prevent bone and muscle loss. Additionally, astronauts currently devote a significant amount of time to exercise (Smith et al., 2012), time that could be spent performing critical science or maintenance activities. The idea of a passive countermeasure suit has existed for nearly as long as human spaceflight.

Recently, the Gravity Loading Countermeasures SkinSuit (GLCS) project created a new intravehicular body suit for use as a countermeasure. As a replacement of normal intravehicular garment, it would be worn by the crewmember during daily activities, providing a constant stimulus to bone/-muscle inducing a constant load on the body to mimic standing and - when integrated with other countermeasures to improve the efficiency of exercising on Earth. Furthermore, an intelligent garment of this kind would offer another tool to scientifically evaluate the effects of the Gz loading on crew health in the microgravity environment (Attias et al., 2013).

FIGURE 6.1: Russian Pingvin Suit

6.2.1 Pengvin Suit

The Russian Pingvin (Penguin) suit (Figure 6.1), developed in the 1970's by Professor Arnlod Barer, is one of the current wearable countermeasures used on the International Space Station (ISS). It was not designed to mimic gravity, but induces weight-bearing stresses on the skeleton, and resistive exercise to the muscles. It uses elastic bands attached to non-stretch anchors at the shoulders, waist, knees and feet to impose two stages of loading on the body (Kozlovskaya et al., 2015). Upper and lower body loading along the vertical axis (z-axis) are imposed by bungee cords above and below a leather belt: from the shoulder to the belt (upper body), and from the belt to the feet (lower body). The upper body can be loaded up to 40 kg, with this load transmitted to the whole body if the belt is loose. Russian Cosmonauts, however, have found it difficult to wear the suit for the recommended 8 hours a day because it is hot and uncomfortable. The Pingvin Suit has poor thermal conductivity that presents significant hygiene issues since, given the fact that clothing cannot be washed in microgravity, presents a significant risk of skin infection (Ewert and Jeng, 2015). Whilst quantification of actual loading has not been published, it is stated to provide a constant load of around 400 N (Waldie and Newman, 2011).

6.2.2 Gravity Loading Countermeasures SkinSuit - GLCS

In an attempt to address some of these issues following the development of elastic fibre and advanced weaving technology the Gravity Loading Countermeasure SkinSuit (GLCS) (Figure 6.2), was conceived at the Massachusetts

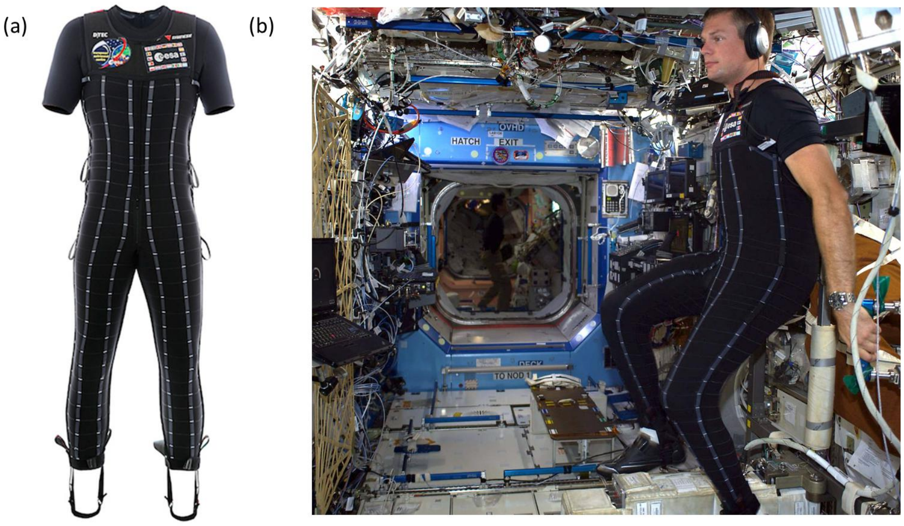

FIGURE 6.2: (a)Design of the Gravity Load Countermeasure Skin-Suit (GLCS). (b) GLCS during the IRISS space mission - astronaut ESA A. Mogensen

Institute of Technology (MIT). SkinSuit technology has the potential to provide low mass, low volume and zero-power usage. The minimal time consumption potentially improving both well characterised musculoskeletal de-conditioning. However, it may reduce potentially injury-risk inducing lower back pain.

The GLCS uses a concept similar to the Penguin suit: a passive garment using elastic materials to provide axial loading to the body. The main difference lies in the fact that the GLCS seeks to improve comfort and to mimic more closely gravitational loading by incrementally increasing the loading from the head to the feet. Figure 6.3 shows the loading profile achieved by a non-uniform stretching of the elastic material, gradually increasing the tension in the vertical direction. The circumferential compression caused by the horizontal fibers anchors the suit to the body by utilizing the friction force between the suit material and the skin. This allows the suit to achieve a portion of the bodyweight loading at the soles of the feet, without the entire load being carried on the shoulders. An initial prototype of the suit was tested on a parabolic flight campaign, and characterized for wearability and comfort (Kendrick and Newman, 2014).

The suit material is a bi-directional elastic weave to achieve the different longitudinal and lateral tensile requirements (Waldie and Newman, 2011). Fibers are oriented with high stiffness or along the z-axis, E_z, so that substantial bodyweight forces can be created without over-stretching the weave, particularly in the lower body. Conversely, low module fibres are used circumferentially, E_{circum}, to facilitate easy donning/doffing, and so

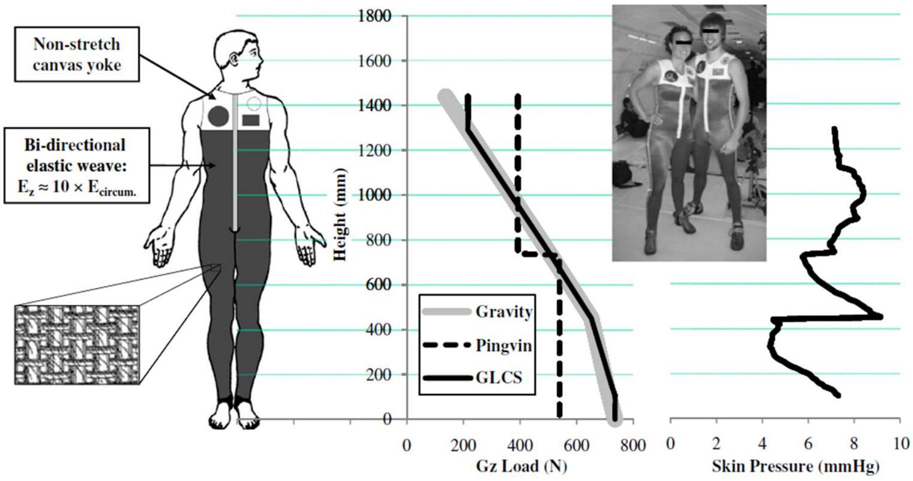

FIGURE 6.3: Gravity loading countermeasure skinSuit (GLCS) with loading regime and skin pressure

that the tension (and hence applied skin pressure) would not vary significantly due to changes in body shape. In recent versions of the SkinSuit, developed by James Waldie (RMIT University), European Space Agency (ESA) and King's College London, arrestor ribbons aligned vertically prevent over-extension of any specific 4 cm section of material. Skin pressure, p, is equal to the force N divided by area A, but is also described by the hoop tension equation 6.1 for a thin walled cylinder

$$p = \frac{N}{A} = \frac{T}{r} \tag{6.1}$$

where T is the circumferential material tension and r is the body segment radius. The height of each stage of the skinSuit, h, is equal to the spacing between the circumferential fibres of the material, and Area A under each stage is therefore equal to the local body circumference multiplied by the stage height, or $2\pi rh$. Using this data and Eq. 6.1 to solve circumferential material tension becomes

$$p = \frac{Nr}{A} = \frac{N}{2\pi h} \tag{6.2}$$

The resistance of the suit to sliding up and down is related to friction forces F, equal to the coefficient of friction between the elastic and the skin μ multiplied by the normal force N. For the GLCS, F represents the axial force trying to displace the suit, and is the difference in loading above and below the stage. F is prescribed as a rate of change in the 1-g loading regime, rather than the absolute loading at the z-coordinate. The normal force N is the force applied by the material on the skin compression, N, required to prevent the stage slipping under the force F. Therefore the tension yields is expressed by the Eq. 6.3

$$T = \frac{F}{2\pi h\mu} \tag{6.3}$$

where, following the Eq. 6.1, the skin pressure is

$$p = \frac{F}{2r\pi h\mu} \tag{6.4}$$

The Mark VI SkinSuit was studied during the IRISS space mission (2-12 September 2015) performed by ESA astronaut Andreas Mogensen in which the objective were:

- to evaluate the ability of the SkinSuit to counteract spine elongation and reduce, or even prevent, lower-back pain - It was assessed through frequent measurements of Andreas's height as well as a pain and questionnaire;
- to measure the +Gz load that SkinSuit provides whilst on the Space Station using NASA's Force Shoes - The plan was to measure the load in three standard postures to evaluate the experience by Andreas during a day on the ISS. However this task was not completed;
- to evaluate operational considerations, in particular in regard to hygiene (by collecting microbiological skin swabs), comfort, temperature regulation and range of motion (by questionnaires);
- to evaluate the effect of wearing the SkinSuit while exercising on the ISS CEVIS bicycle exercise machine.

Notwithstanding the final goal to mimic the Gz force on the musculoskeletal system with a gradual force distribution. One of the current limit of the GLCS is the inability to control the loading. Each GLCS is designed and taylored personally for each subject. Since the zero-g effects start to appear and to get worse, in a different manner for each subject and with different timing during a spaceflight mission, a load adjustment mechanism would allow to develop an *adaptable* system able to customize the countermeasure effects. Thus, the objectives of this Chapter are:

- to provide a Gz-load adjustment system;
- to give the chance to adjust the load according to different gravity condition (0-g, Moon or Mars gravity);
- to monitor the load variation;
- to investigate the balance between GLCS loading and comfort.

Moreover, the GLCS does not allow to monitor the g loading status over time, since the wearable system is entirely passive and it is designed to produce the maximum load available, following the anatomic measurements of the subjects. This requirement begins to be significant if the GLCS is able to adapt the g-loading according to the needs.

This Chapter defines a proof-of-concept of a adjustable Gz-load system and a wearable Load/Stretch Monitoring (L/SM) designed and characterized in order to obtain a real-time measure of the load and to titrate loading concurrently. As access to GLCS is limited, to test and to validate the adjustable load mechanism, a GLCS simulator was developed according to the original properties of the suit in terms of performance and mechanical properties.

6.3 Load Adjustment and Monitoring System for the GLCS

The current MK VI GLCS is designed to achieve around the 20-25% of the subject's body weight. Previous versions (Mark I, II, III) achieved higher loading but discomfort was significant. Exploiting the elastic properties of the SkinSuit material and its design, the stretch level can be adapted, increasing or decreasing the Gz-load. Furthermore, this Gz-load variation has to be monitored with a wearable system embedded within the GLCS.

In the first part of this section, a proof-of-concept of a load adjustment mechanism and a Load Monitoring (LM) system, integrated within the lower body GLCS simulator, are presented:

- definition of the project requirements;
- design of the load adjustment mechanism;
- design of the lower body GLCS simulator - tests and results;
- implementation of the the load adjustment mechanism with the lower body GLCS simulator - test and results;
- design and implementation of the LM system - test and results of the overall system;

Following the results obtained during the previous experiment, the second part of the section presents a more reliable solution to monitor the Gz-load variation of the GLCS, exploiting the stretch properties of the suit material. The Stretch Monitoring (SM) system designed is based on a custom and wearable stretch sensor coupled with a wireless read-out circuit. On the basis of the results obtained the SM system has been selected to be integrated within the SkinSuit for the future field testing.

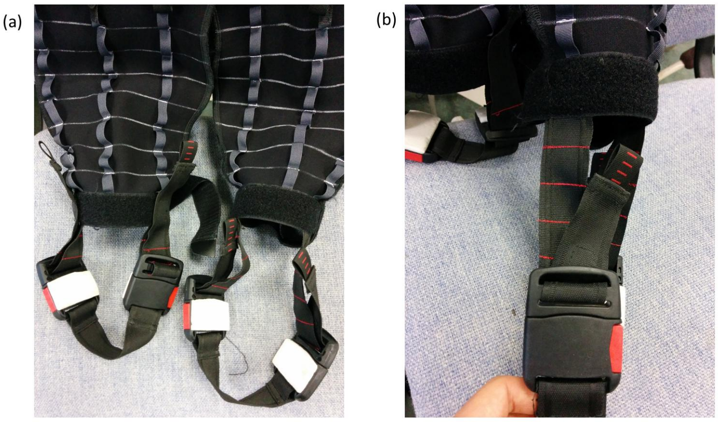

FIGURE 6.4: Gravity Load Countermeasure SkinSuit lock mechanism. (a) Lower part of the SkinSuit. (b) Detail of the lock mechanism

6.3.1 Requirements Definition

The structure of the SkinSuit can be sub-divided into three main sections:

- non-stretchable canvas yoke around the shoulders;
- gradual stretchable material from the chest to the ankles;
- non-stretchable stirrups wrapped around the sole of the foot.

The main feature of the GLCS, in comparison with the Pengvin Suit, is the loading profile obtained via non-uniform stretching of the elastic material, which gradually increases the tension along the vertical direction, with an analogue path of the gravity force profile. This important aspect has not to be altered with the implementation of a new mechanism or other system. For this reason, the GLCS' portion candidate to be adapted with the new mechanism is the bottom part, where the non-stretchable stirrups are connected through buckle clips in the rest of the suit. Figure 6.4 shows the current lock mechanism used in the GLCS Mark V. Following interviews with some ESA members involved in the GLCS project, Table 6.1 summarizes the advantages and disadvantages of the existing system.

The solution proposed aims to replace the buckle clips with a wearable mechanism able to change the length of the stirrups and then the stretch (or load) level produced by the SkinSuit. In order to obtain a balanced load, a couple of mechanisms have to be used for each ankle. Figure 6.5 shows the working principle of the load adjustment system.

The load adjustment device has to maintain the benefits of the current system whilst allowing a fine control of the SkinSuit's Gz-load. To enhance comfort, the system has to be compliant with the body shape, in particular the ankle anatomy and ensuring a reliable connection with the rest

TABLE 6.1: Advantages an disadvantages of the current design.

Advantages	- easy and simple implementation; - rapid lock and unlock; - always integration with Force-shoes.
Disadvantages	- no-calibrated adjustment; - manual lock (in microgravity it requires the help of an addition crewmember); - unintentional loosening over the time; - uncomfortable and bulky.

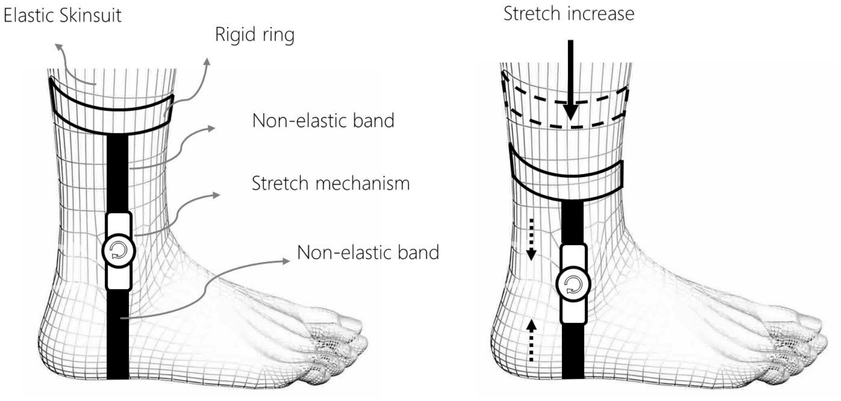

FIGURE 6.5: Load adjustment device - working principle

of the suit. Finally, it has be light, compact, low-cost, able to withstand a maximum force around 150 N, and easy to use without the aid of another person.

6.3.2 Load Adjustment Mechanism

Several candidate mechanical devices were considered bet, the *ratchet* mechanism, properly customized, was deemed to be the most suitable. A ratchet is a mechanical device that allows continuous linear or rotary motion in a single direction preventing reverse. A ratchet is one of the oldest of all mechanisms and its simplicity and reliability are the main advantages. It can bear a large load in relation to its size (Onwubolu, 2005). Basically, as shown in Figure 6.6, a ratchet mechanism consists of a ratchet wheel (1), a driving pawl (2), an arm (3), a locking pawl (4), and a support (0). The driving pawl engages the teeth of the ratchet wheel under the action of a spring, or its own weight. When the arm moves counter-clockwise, the driving pawl turns the ratchet wheel through a given angle. When the arm moves clockwise, the catch slips past one or more teeth, but the locking

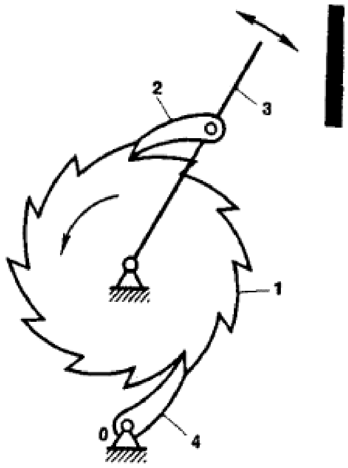

FIGURE 6.6: Ratchet mechanism - working principle

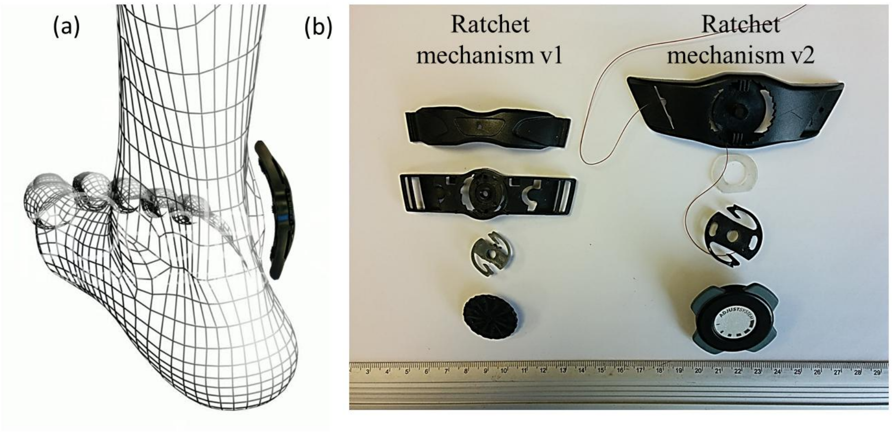

FIGURE 6.7: (a) Ratchet mechanism suitable shape with the malleolus and embeddable with SkinSuit. (b) Two different ratchet mechanisms with some mechanical improvement in order to enhance the robustness and usability.

pawl prevents the clockwise rotation of the ratchet wheel. Ratchets can be used to tension ropes or cables but are usually bulky and heavy.

However, the same principle can be re-adapted with a different geometry, in order to reduce the size and the weight whilst preserving efficiency. For instance, the ratchet adjustment mechanism used for bicycle helmets is light and compact used to adjust the internal size (Grim and Stroud, 2011). It was selected to adjust controllably the length of the SkinSuit's stirrups and fix it in a stable position. Figure (6.7) depicts the mechanism chosen and the relative placement on the body, enabling the compliance in terms of size and geometry with the ankles anatomy, compared to the original uncomfortable buckle clips.

6.3.3 GLCS Lower Body Simulator

After the requirements analysis and selection of the technology, the mechanism was re-adapted and tested in order to prove the feasibility of the implementation and the performance. Since each SkinSuit has to be individually tailored, a *GLCS simulator* was designed to test the adjustable mechanism. The current suit is able to produce a 20-25% of the g-force on the body at the maximum stretching level. Practically, after the donning, the SkinSuit has to be "activated" pulling up the stirrups to a fixed position. Over stretching across the suit is prevented by the inelastic *arrestor ribbons* aligned vertically along the suit, avoiding an over-extension of any specific 4 cm section of material. Thus, when the arrestor ribbons become completely flat to the suit, maximum stretch has been achieved. Furthermore, a preliminary test demonstrated that the SkinSuit, before the "activation", resulted already stretched at the torso, since the arrestor ribbons were completely flat. This led to the following considerations:

- without an "activation" from the bottom, the upper part of the suit produces a z-axis force, albeit minor, when it is put on;
- the z-axis force variation depends on the lower part of the suit, starting from the legs;

These remarks lead to consider the opportunity to focus the attention on the lower part of the suit, designing a "legs GLCS simulator", in which to embed the load adjustable mechanism and measure the relative effects. Considering a MK V SkinSuit and a subject whose body mass was 60 kg, the maximum z-axis weight force achieved by this suit is approximately 17 kg ($F_{GLCS} = 167\,N$), 25 % of the total weight. From this value, the small contribution of the torso has to be considered and subtracted from the total force produced. An experiment by using a half-body dummy dressed with the GLCS (Figure 6.8) the torso force contribution was defined by weights applied at the hips and then measuring maximum force required to stretch the arrestor ribbons. With a weight of 2.5 kg ($F_{torso} = 24.5\,N$ handlebar included), was required to completely the upper part of the SkinSuit wa. Therefore, the requirements needed for the lower body GLCS simulator experiment are:

- to mimic the elasticity of the suit;
- to produce a force around 140 N ($F_{legs} = F_{GLCS} - F_{torso} = 164\,N - 24\,N = 140\,N$);
- to adjust the load of the simulator;
- to host the ratchet mechanisms;

FIGURE 6.8: GLCS torso load contribution

- to measure the force/load changes.

Figure 6.9(a) shows the initial version of the lower-body GLCS simulator in which the elastic cords simulate one leg of the suit and the frame allows to adjust the stretch. The elastic material and the soles are connected together with the adjustable retched mechanism. The nominal length and the strength of the elastic cord were selected in order to achieve 70 N for each leg ($140\,N/2$). Stretch/force characterization was then performed in order to test the adjustable mechanisms under different load conditions. A cell load connected with the system measured the force change when the elastic cord was stretched with a ΔLength (ΔL) of 50 mm until 500 mm. Characterization shown the expected liner relation between ΔL and force (Figure 6.9 (b)), highlighting the maximum value reached by "one leg" of the suit equal to 73.5 N, proportional with the amount of Gz force that the GLCS is able to produce.

In order to performed a test as close as possible to the final application, Figure 6.10(a) and (b) depict the architecture and the final implementation of the entire GLCS lower-body simulator. The structure connected with a hospital bed allowed to change the length (hence the force) of the system varying the height of the bed with a dedicated lifting mechanism.

The first test was performed to prove the robustness of the ratchet mechanism, leading the force up to the maximum level and thus identifying the point of failure. Any mechanical failure was recorded during a cyclic stress test, in which the system was lead to the maximum stretch achievable and relaxed for 5 min continuously.

The second step was to demonstrate the effectiveness of the adjustable mechanism. Each ratchet mechanism was adapted to bear a force up to

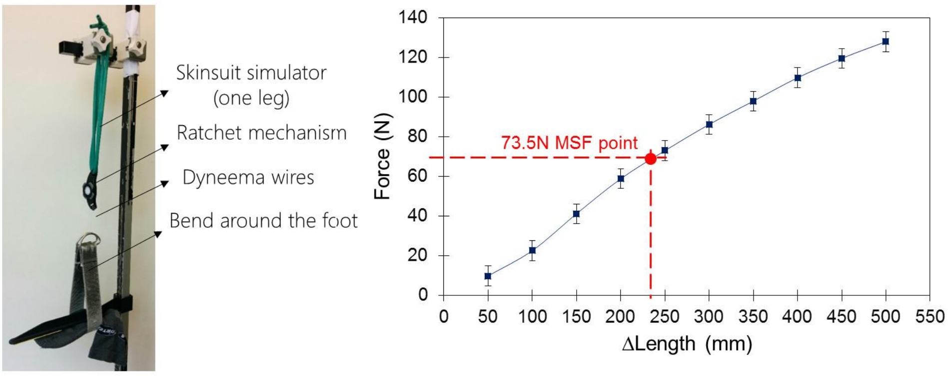

(a) (b)

FIGURE 6.9: (a) Single-leg GLCS simulator. (b) Stretch-Load test of the lower body GLCS simulator with load cell (single leg) - Line to the best fit. MSF: Maximum SkinSuit Force

90 N before to reach the breaking point. A couple of mechanisms for each ankle were activated manually under a pre-loading condition of 50 N. The gear was turned for 4 times and the length variation was measured. Thanks to the previous length/force characterization, the graph in Figure 6.10 (b) shows the force variation generated by the ratchet mechanisms.

The results show some promising properties of the mechanism obtaining a ΔL of 20 mm for each turn and thus a relative force variation $\Delta Force$ equal to 20 N, therefore 5 N per turn. Then, the internal design of the mechanism with 80 teeth, allows to adapt the load with a sensitivity of 0.17 N.

In conclusion of this experiment a proof-of-concept of the load adjustable mechanism for the GLCS was presented, in particular the evaluation of the ratchet mechanism solution and its properties. The next step is related to the design and test a wearable Load Monitoring (LM) system integrated within the GLCS able to measure $\Delta Force$ variation over the time.

6.4 Load Monitoring (LM) system - State of the Art

During the IRISS Space Mission performed by ESA astronaut Andreas Mogensen, one of the objective was to collect data about +Gz loading due to the SkinSuit. In terms of reliability tested during previous NASA experiments, the *Force-shoes* were candidate as measuring instrument to be used with the GLCS, in order to collect loads data of the Gz-load.

Designed by XSENS (*Xsens Force Shoes*), the Force-shoes (Figure 6.11) were used for the first time by NASA during exercise with the Advanced Resistive Exercise Device (ARED) on the International Space Station (ISS).The ARED uses adjustable resistance piston-driven vacuum cylinders along with a flywheel system to simulate free-weight exercises in normal gravity with

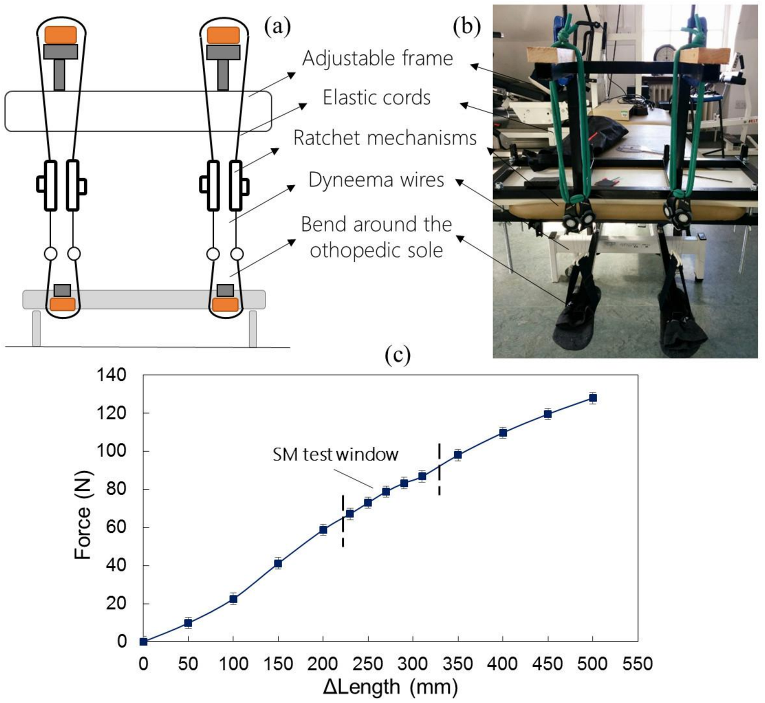

FIGURE 6.10: (a)Architecture of the full lower-body SkinSuit simulator. (b) Implementation of the simulator. (c) Characterization of the adjustable load mechanism.

the aim to retain strength, posture ability and functionality of the crew member's body (Fregly et al., 2013). The aim of the Force-shoes was to measure the exercise loads on the ARED with high accuracy, providing important data for current and future human research experiments in space (Hanson et al., 2014).

Although the reliability of the technology, the Force Shoes were not worn since the mission planners was shortened, skipping the Force Shoes tests. Furthermore, they are bulky, complex, does not provide a continuous real time Gz monitoring and take time to set up, a new simpler integrated load sensor system embedded within the SkinSuit, is the objective presented in the following section.

6.4.1 Sensor Technology Selection

As mentioned previously, the SkinSuit Mark V is able to produce a vertical load along the body of around 20-25 % of the body weight. In particular, the z-force vector is applied beneath the feet only on a portion of the stirrups that are rapped around the sole of the foot. The amount of the force is around 73.5 N per foot applied on a surface of 35 cm^2, measuring the stirrup area in contact with the foot. Therefore the resulting pressure is 21 kPa. The initial solution proposed was to instrument the stirrups with a flat and

FIGURE 6.11: Xsens Force Shoes

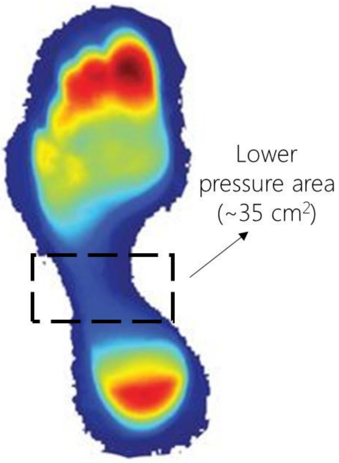

FIGURE 6.12: Sensor placement and standing weight distribution.

reliable force sensor. The selection of the suitable technology to be implemented takes into consideration the current plantar pressure technologies, normally used for podiatry, gait and posture analysis.

In taking any biomechanical measurements, devices must be optimized for the specific application to ensure that readings are accurate. Detailed analysis must be thoroughly undertaken prior to any measurements and for foot plantar system the sensor requirements have to be taken into consideration. The key specifications for the sensor performance include: linearity, hysteresis, pressure range, sensing area of the sensor, operative frequency, creep and repeatability, as detailed by Abdul Razak et al., 2012. In addition, the placement of the sensor is critical and, as explained in Par.6.12, the right placement was a trade-off between the sensor size and the sensing area.

There are a number of different commercial plantar pressure sensors including capacitive sensors, resistive sensors, piezoelectric sensors and piezoresistive sensors. These sensors provide electrical signal output (either voltage or current) that is proportional to the measured pressure. There is a number of commercially available foot-pressure sensors but they generally do not fulfil the requirements of many biomechanical applications due to specifications (size of sensing are, user interface, fit comfort and portability) and performances limitations (pressure range and accuracy) . A brief summary of the features of each technology, with the relative commercial products is listed below.

Capacitive Sensors - the sensor consists of two conductive electrically charged plates separated by a dielectric elastic layer. Once a pressure is applied the dielectric elastic layer bends, which shortens the distance between the two plates resulting in a voltage change proportional to the applied pressure.
Commercial products based on this system are the $emed$® platform systems (Novel, Germany) and $Pedar$® in-shoe systems (Novel, Germany) (*Novel Quality in Measurement*). Both not suitable for our application since the $emed$® is not embeddable with the SkinSuit and $Pedar$® has a bulky and hungry power electronic system.

Resistive Sensors - Force-Sensing Resistor (FSR) is a good example of resistive sensors. When pressure is applied the sensor measures the resistance of a conductive foam between two electrodes. The current flowing through the resistive sensor increases as the conductive layer changes (i.e., decreases resistance) under pressure. FSRs are made of a conductive polymer that changes resistance with force: the application a force causes the conductive particles to touch increasing the current through the sensors (Shu et al., 2010). FSRs are flat and easily integrable with a fabric, make it suitable for our application.
Commercial products based on this principle are $MatScan$® platform systems and $F - Scan$® in-shoe systems (Tekscan, USA).

Piezoelectric Sensors - produce an electric field (voltage) in response to pressure. The most suitable material for clinically oriented body pressure measurement is polyvinylidene fluoride (PVDF) because it is flexible, thin and deformable (Gefen, 2007). Piezoelectric devices have high impedance and therefore susceptible to excessive electrical interference that leads to an unacceptable signal-to-noise ratio.
Commercial products based on this system are Measurement Specialties, USA (*Measurement Specialties*) and PCB Piezotronics, Inc., USA (*PCB Piezotronics, Inc.*).

Piezoresistive Sensors - are made of a semiconductor material. In Piezoresistive materials the bulk resistivity is influenced by the force or

TABLE 6.2: Comparison of in-shoe pressure sensors commercially available compared to Wahab et al., 2008.

	Wahab et al.	**Textile Sensor**	**Parotec**	**Novel**	**Tekscan**	**Vista Medical**
Sensor Size	2 mm	N.D.	2 mm	1.9 mm	0.15 mm	2 mm
Number of sensor	15	6	24	99	960	128
Pressure range(kPa)	3.000	800	625	1.200	1.034	260
Pressure sensitivity	N.D	N.D.	N.D.	<7%	24%	N.D.

pressure applied: when the sensor is unloaded, the resistivity is high and when a force is applied the resistance decreases. When there is a pressure on the piezoelectric element (quartz crystal) the material produces electric charges from its surface. These charges create a voltage proportional to the applied force.
Commercial products based on this system are $FlexiForce^{\circledR}$ (Tekscan, USA) and ParoTec (Paromed, Germany) (*Paromed*).

Sensors from Vista Medical, Novel and Tekscan show some performance limitations as they are made of sheets of polymer or elastomer leading to issues such as repeatability, hysteresis, creep and non-linearity of the sensor output (Table 6.2).

Considering the final application, in which the sensor has to bear peaks of pressure of about 20-25 kPa and has to be comfortable interfacing both with the flexible surface of the stirrup and the skin, the Force Sensing Resistor® (FSR) was selected, tested and characterized before being embedded into a GLCS.

Figure 6.13 shows the sensor the architecture of the system.

6.4.2 FSR Characterization

Force Sensing Resistor (FSR) is a Polymer Thick Film (PTF) device which exhibits a decrease in resistance with an increase in the force applied onto the active surface. Its force sensitivity is optimized for use in human touch control of electronic devices. An overview of the FSR typical response behaviour is expressed via Force(N) vs Resistance ($k\Omega$) characteristic plotted in Figure 6.14 (a), using data from the technical datasheet. The characterization was carried out with a stainless steel actuator with a 10.0 mm diameter hemispherical tip of 60 durometer polyurethane rubber. These data show a particular force-resistance characteristic being the response of evaluation

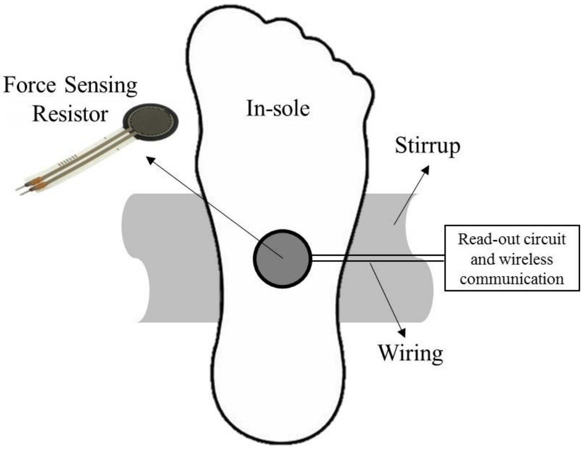

FIGURE 6.13: Load Monitoring system architecture.

part *FSR402* with 12.7 mm diameter circular active area. FSR resistance operates as more pressure is applied. When there is no pressure, the sensor looks like an infinite resistor (open circuit), as the pressure increases, the resistance goes down. At the low force end of the force-resistance characteristic, a switch like response is evident. This turn-on threshold, or "break force”, that swings the resistance from greater than $100\,k\Omega$ to about $10\,k\Omega$ (the beginning of the dynamic range that follows a power-law) is determined by the substrate and overlay thickness and flexibility, size and shape of the actuator, and spacer-adhesive thickness (the gap between the facing conductive elements). Break force increases with increasing substrate and overlay rigidity, actuator size, and spacer-adhesive thickness. Eliminating the adhesive, or keeping it away from the area where the force is being applied, such as the center of a large FSR device, ensures it a lower rest resistance (e.g. stand-off resistance). The sensor reaches the saturation force beyond 10 kg. The saturation pressure of a typical FSR is in the order of 100 to 200 psi. Forces higher than the saturation force can be measured by spreading the force over a greater area; the overall pressure is then kept below the saturation point, and dynamic response is maintained. Figure 6.14 (c) depicts a Force-Resistance characterization according to the project requirements, in terms of force range and accuracy, showing a high measurement error with forces lower than 40 N and a small force variation between 40 to 100 N.

Figure 6.14 (b) shows the relation between the conductance ($\frac{1}{R}$) and the force. This format allows interpretation on a linear scale. For reference, the corresponding resistance values are also included on the right vertical axis. It also includes a typical *part-to-part* repeatability envelope. The error band determines the maximum accuracy of any general force measurement. The spread or width of the band is strongly dependent on the repeatability of

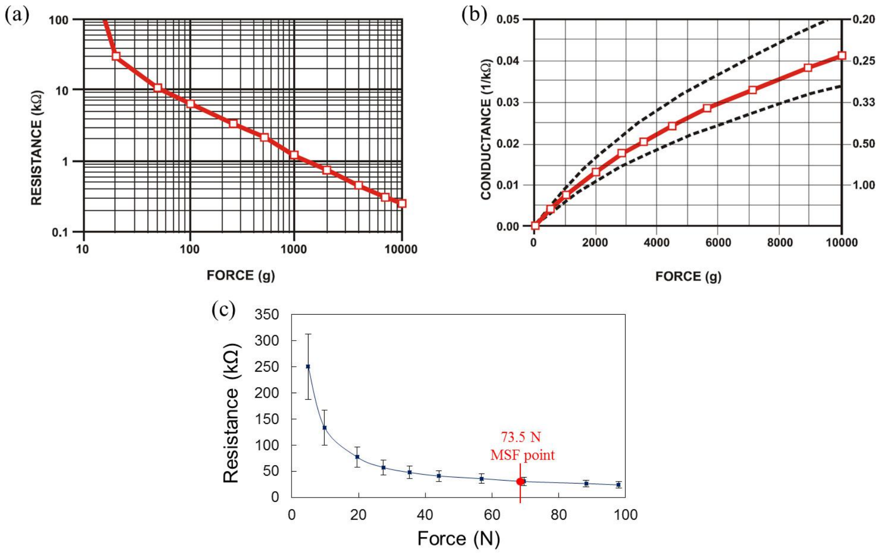

FIGURE 6.14: (a) FSR Force-Resistance characterization. (b) FSR Force-Conductance characterization. (c) Force-Resistance characterization simulated the GLCS conditions

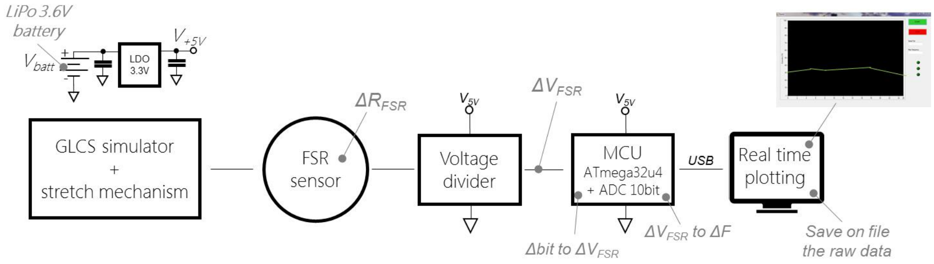

FIGURE 6.15: FSR System Architecture.

any actuating and measuring system, as well as the repeatability tolerance held by the manufacturer (Interlink Electronics) during FSR production. Typically, the *part-to-part* repeatability tolerance held during manufacturing ranges from $\pm 15\,\%$ to $\pm 25\,\%$ of an established nominal resistance.

6.4.3 FSR System Architecture

Figure 6.15 shows circuit used to test the sensors adopting a simple force-to-voltage conversion. The FSR device was tied to a measuring resistor in a voltage divider configuration ($\Delta R_{FSR} - to - \Delta V_{FSR}$) . The sensor connected to the power supply with a $+5\,V$ Low-DropOut regulator (LDO) and to the pull-down resistor R_{fixed} to ground. The ΔV_{FSR} of the voltage divider was connected to an ADC of a microcontroller. In accordance with the previous sensor characterization, the firmware code (see Appendix) flashed within the microcontroller was able to convert the ΔV_{FSR} into a Force variation

(ΔF). Finally, thanks to an ad-hoc user interface wrote in $C\#$, the results were plotted in real time on a laptop.

The output of the voltage divider is described by the eq. 6.5

$$V_{OUT} = \frac{V_{+}}{(1 + \frac{R_{FSR}}{R_{fixed}})} \tag{6.5}$$

In the shown configuration, the output voltage increases with the force applied. If R_{FSR} and R_{fixed} are swapped, the output swing will decrease with increasing force. These two output forms are mirror images about the line $V_{OUT} = \frac{V_{+}}{2}$.

The measuring resistor, $R_{fixed} = 10k\Omega$, was chosen to maximize the desired force sensitivity range and to limit current according to the datasheet (*Arduino Board Yun*). Following the datasheet, the current through the R_{FSR} should be limited to less than $1\,mA/cm^2$ with a force applied. A single sided supply LM358 op-amps was used to reduce the error due to the source impedance of the voltage divider. In this configuration the analog voltage reading from the microcontroller ranges from 0 V to about 5 V.

The source code(see Appendix) flashed onto the MCU (ATmega32u4) uses the embedded Analog Digital Converter (ADC) and allows an analog to digital conversion, following the eq. 6.6,

$$\frac{ADC resolution}{Voltage\, supply} = \frac{ADC\, reading}{Analog\, voltage\, measured} \tag{6.6}$$

$$\frac{1023}{5\,V} = \frac{ADC\, reading}{Analog\, voltage\, measured} \tag{6.7}$$

In particular it is a 10-bit ADC, thus it is able to detect 1,024 discrete analog values. The MCU reads the analog value coming from the voltage divider (V_{FSR}), converts to digital ones and calculates the resistance (R_{FSR}) as described in eq. 6.8. By calculating the conductance ($G_{FSR} = \frac{1}{R_{FSR}}$) the MCU is able to derive the Force (F_{FSR}), in accordance with previous characterization expressed in Figure 6.14 (b).

$$R_{FSR} = \frac{(V_{+} - V_{FSR}) \cdot R_{fixed}}{V_{+}} \tag{6.8}$$

The following tests were performed with the goal to evaluate the reliability of the system and repeatability of the measurements.

6.4.4 Tests and Results

The FSR sensor was implemented and tested with the full lower-body GLCS simulator, in accordance with Par. 6.4.3 System Architecture. The experiment applied varying elastic forces with a ΔL of in steps of 50 mm and

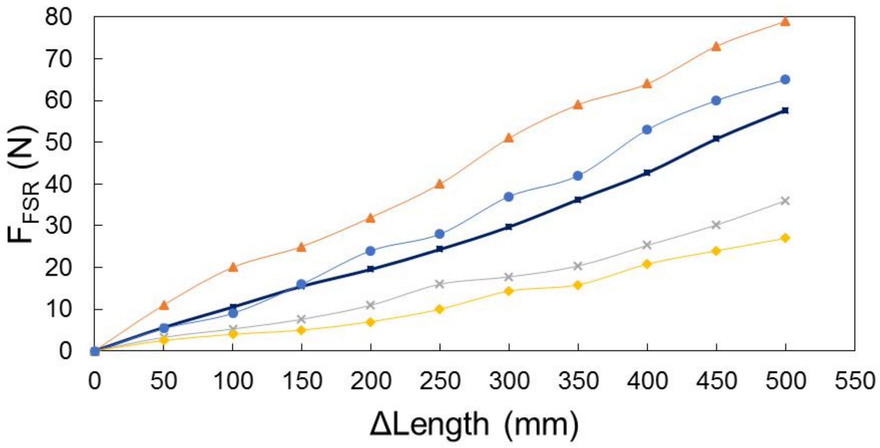

FIGURE 6.16: Reliability test of FSR with the lower body GLCS simulator.

reading the (F_{FSR}) from the sensor system with an average of 50 samples for each measurement point.

Figure 6.16 plots the behaviour of the force sensor (F_{FSR}) under different measuring set. The FSR sensor shows a linear behaviour at varying loads, however the repeatability is poor with standard deviation larger than 40%, with different measurements in the same experimental conditions. At a fixed ΔL value corresponds different F_{FSR} values during different measuring sets, mainly due to the anatomy of the foot, to the flexibility of the stirrup and to slight movement of the sensor across the foot sole surface. The foot has not an uniform surface and anatomy with high and low pressure profile in different areas; besides the movable stirrup, therefore the relative position of the FSR sensor with the foot can not be fixed. Furthermore, higher values were recorded when the sensor moved accidentally near the edge of the foot, due to a cutting edge effect between the stirrup and the sole; while lower and variable values were recorded when the sensor moved in the middle of the sole.

Furthermore, with a force distributed on the top of the sensor, the values read by the system were different from the previous ΔL vs $Force$ analysis, because, as shown in Figure 6.17, the sensor has been designed to sense a pressure applied only within the "black rigid ring" portion. With a force applied over a larger area, the rigid ring absorbs part of the force, recording a lower force value from the sensor. To solve this issue, a squared FSR sensor was used, however the curved profile of the sole causes a deformation of the sensor and then a resistance variation without any load applied.

As only load monitoring system has to be reliable and the measurements repeatable without a re-calibration of the system over the time based on the results obtained with the FSR sensors, are not suitable for integration

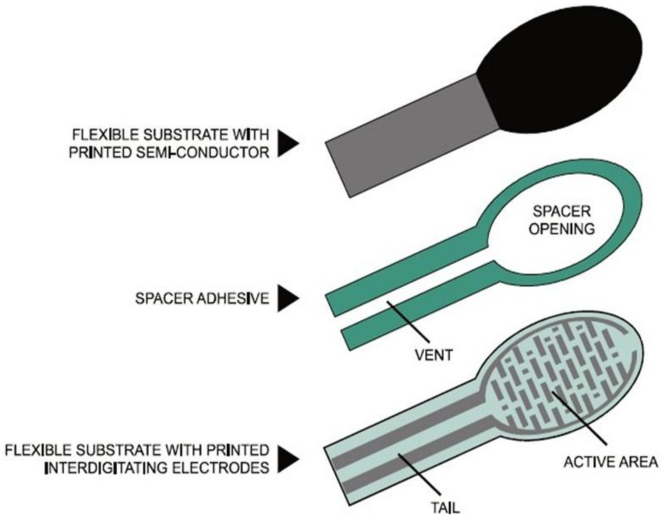

FIGURE 6.17: FSR structure.

with the GLCS.

To solve the issues reported and to respect the objectives of the project, in the next section a new technological approach is proposed.

6.5 Stretch Monitoring (SM) system

An alternative strategy is to measure the stretch of the suit. As described in 6.2.2, the GLCS gradually increases the tension in the vertical direction thanks to gradual distribution of the non-uniform stretch material. Exploiting the properties of the material, different stretch levels of the SkinSuit means different Gz-load values. Therefore measuring the displacement from two fixed points on the SkinSuit with a stretch sensor, allows to evaluate the amount of the stretch and thus the Gz-load applied by the suit. The solution proposed shown the following advantages:

- it is not affected by the foot anatomy;
- it is limited body-sensor interface;
- it can be easily customized for each GLCS.

Whereas, the challenges to overcome were:

1. to seek a suitable placement of the sensor on the SkinSuit followed by a previous suit stretch characterization;
2. to identify a wearable stretch sensor compliant with the elastic properties of the SkinSuit;

3. to characterize the sensor selected;
4. to integrate the stretch sensor coupled with a wireless read-out circuit within the SkinSuit;
5. to test and validate the system in the field.

6.5.1 GLCS stretch characterization

The structure of the GLCS Mark V, used for this evaluation, has a structure subdivided into 25 circumferential bands of about 3 cm of height and each band has arrestor ribbons aligned vertically to prevent over-extension of the material (see Figure 6.2). The stretch sensor, placed perpendicularly to the elastic bands, thus needs to be able to monitor local displacement. However, the vertical stretch is not uniform along the suit was worn and some portions are more stretchable than others. Therefore, it was necessary to characterized the GLCS in order to evaluate the amount of stretch in different areas and find the suitable placement for the sensor, in terms of range and variation of stretch.

Four different portions of the GLCS was characterized: torso, hips, upper leg and lower leg. Stretch characterization was performed by measuring the distance between the pairs of markers placed on each area with load. The nominal distance before stretch was to 60 mm, that is the height of two circumferential bands. Figure 6.18 (a) shows the experimental setup. When the GLCS is completely stretched the highest load is reached. In order to determinate the load range the maximum load of the GLCS Mark V is around 20-25 % of the subject's body-weight and thus for this test the max load was up to 15-17 kg.

The delta elongation (ΔL) of each area at different loads is not linear, as shown in Figures 6.18 (b), highlighting that the GLCS was not designed for use with different loads but with a single design load. Thus, as expected each area behaves differently with the same load, however the torso is resulted completely un-stretchable after donning. Torso and lower leg portion show the major variation and in particular:

- no changes of the torso part is appreciated, resulting completely stretched since the beginning of the experiment without any loads;
- an approximate linear and constant stretch-load behaviour was observed in the lower leg area.

The results shown the lower leg portion as the best candidate for stretch sensor placement.

Finally, as introduced in Paragraph 6.2.2, the friction between the suit and the skin was another relevant aspect to be considered, given that it

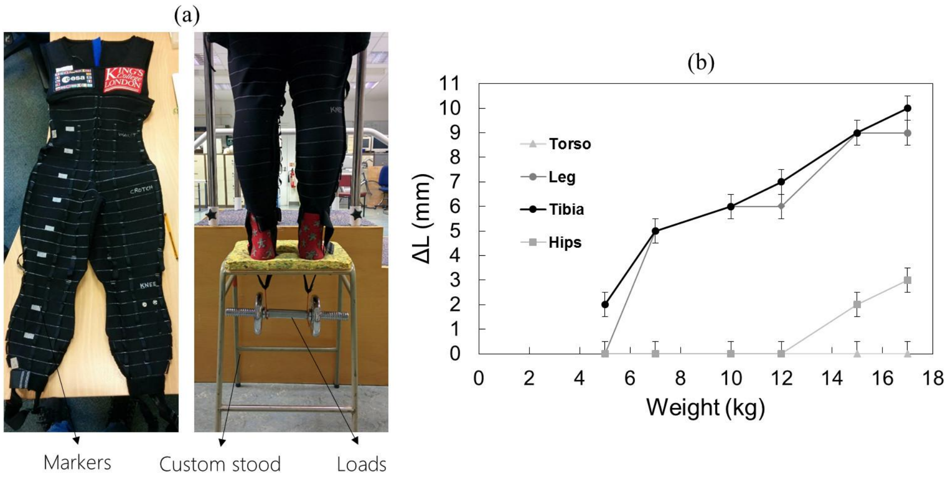

FIGURE 6.18: (a)Experimental set-up GLCS stretch characterization adjusting the Gz-load. (b) The four lines shows the stretching trend at different GLCS portion.

affects the stretch of the suit, compromising the linearity of the stretching. For this reason for the next part of the experiment, Talco powder has been be used to reduce the friction.

6.5.2 Sensor - Material selection

The strain gauge is one of the most common technologies used to measure strain/stretch. A strain gauge provides an extremely simple and accurate way to measure even slight deformation of a solid surface or object. It is a relatively simple transducer that varies slightly in resistance when compressed or stretched, and can be bonded (using adhesive such as epoxy) to metal, plastic, wood, glass or other solids. Strain gauges made out of semiconductor material, like silicon or germanium, take advantage of the piezoresistive effect, a change in resistance that is greater than what can be explained by simple geometric deformation. Therefore strain gauges can reach high sensitivity $< 1\,\mu m$ and with a small active area of 1-2 mm^2 (Hannah and Reed, 1992).

However, this type of the technology can not be used for wide displacement and to be embedded into a flexible substrate, such as a fabric. Nevertheless, exploiting the same principle of piezoresistivity, has been made a range of wearable piezoresistive sensors. They can be sub-divided mainly into three categories: conductive yarn, thick film and conductive fabric.

Usually the advantages of these sensor are the comfort and the easy integration into a fabric by conventional textile processing (Huang, Tang, and Shen, 2006; Melnykowycz et al., 2014; Gibbs and Asada, 2005). The drawbacks came out when read-out electronics, typically rigid and bulky, have to interface with a fabric surface. It is very difficult to make a strong connection between the conductive yarns and electronics that need to be resistant to abrasion, wearing and washing. To address this issue, conductive polymers are widely used to develop conductive fabrics and in particular they are identified into two subclasses: intrinsically conductive polymers (ICPs) and conductive polymer composites (CPCs).

The ICPs can be coated onto the high elastic fabrics by an in situ chemical polymerization process (Brady et al., 2007; Scilingo et al., 2003). The result is a piezoresistive fabric with a strong variation of strain-resistance with time and a long response time. Paradiso et al., 2005 made a strain sensing fabrics by using CPCs. Composites made from carbon black filled silicone were coated onto high elastic fabrics showing a strain sensing properties between 5% and 35% of the strain.

Low complexity but high strain performing, stretch sensors can made be by conductive silicon (or conductive rubber) which could be integrated within the elastic fabric of the SkinSuit to measure the strain of the textile material under stretch. Conductive rubbers can be used as substitutes for traditional conductive materials, where lightweightness and flexibility are required: via the use of conductive fillers to achieve a low resistance the most common of which is black carbon .

A preliminary test was performed with the only available commercial product (conductive rubber cord *Conductive rubber cord*), depicted in Figure 6.19 (a). A 2 mm diameter rubber string impregnated with carbon-black with a nominal length of 40 mm was tested. Stretching the piezo-material with a step of 2 mm ΔL, the resistance variation (ΔR) was measured with a bench digital multimeter. The results, depicted in Figure 6.19 (b), show a rapid resistance variation at the beginning of the elongation phase, reaching a plateau after only 4-6 mm of stretching. Then, only a slight changes was measured with further stretch. Furthermore, the material took several minutes (around 5 min) to revert to the original length and electrical resistance condition. The material was however able to be stretched up to the 70% of its nominal length.

The results demonstrate that this kind of sensor can not be used for the Stretch Monitoring system since:

- it has not a linear ΔR variation at different elongation;
- it takes 5 mins minutes to revert to original condition (viscoelastic behaviour);
- it has a fast response following a stress but it tends to reach saturation after few 4-6 mm of elongation, which is less than the desired range of changes (around 20 mm);

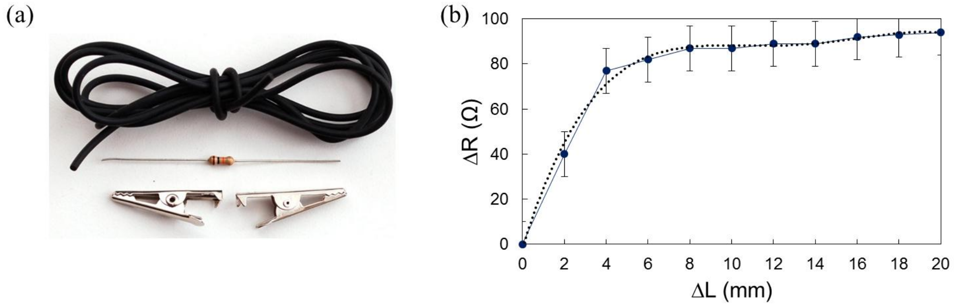

FIGURE 6.19: (a)Commercial stretch sensor. (b)Stretch-Resistance characterization.

TABLE 6.3: Conductive silicone ELASTOSIL 570/70 properties.

Typical characteristics	**Inspection Method**	**Value**
Hardness Shore A	DIN 53505	70
Crosslinker		C1 or C6
Appearance		black
Density	DIN 53479	1.1 g/cm^3
Tensile strength	DIN 53504 S 1	5.7 N/mm^2
Elongation at break	DIN 53504 S 1	140 %
Tear strength	ASTM D 624 B	9.9 N/mm
Volume resistivity	DIN IEC 93	2.8 Ω/cm
Compression set	DIN ISO 815-B	29 %

- its resistance changes after a bending of the material without stretch.

These critical aspects arise from the chemical composition of the conductive silicone and the moulded process. Therefore, to overcome the issues reported whilst maintaining the mechanical properties, the CLR with brand name ELASTOSIL 570/70 from Wacker Chemie AG (*Wacker ELASTOSIL*) has been chosen to develop a custom stretch sensor. It is an electrically conductive bi-component silicone rubber for press moulding and post curing. Table 6.3 summarizes the properties of the material.

In order to achieve the optimum electrical properties, it was post cured for 4 h at 200 $^{\circ}C$ after moulding. The minimum crosslinking temperature is 170. The result was a layer of conductive silicone $48\,cm \times 3\,cm \times 0.2\,cm$ (L x W x T) with resistivity of 2.8 Ωcm (Figure 6.20).

6.5.3 Stretch Sensor - Characterization

The moulded layer of conductive silicone was cut to obtain different strips of material with different length, from 500 mm to 50 mm with a step of 50 mm, with a constant width and thickness, 3 mm and 2 mm respectively. The strips characterized by stretching the material with a step of 5 mm and measuring the resistance variation with a bench digital multimeter. The

FIGURE 6.20: Custom stretch sensor.

objectives of this experiment were to analyse the behaviour of the material under static mechanical stress and evaluate the presence of hysteresis during the relaxation phase (poor-stretch release).

Figure 6.21 (a) collects the results each length sensors and the significant results can be summarized as follow:

1. the linear resistance variation under static mechanical stress, independently from the nominal length;
2. the low hysteresis during the relaxing phase, with the stretch and relaxation lines almost overlapped and a relaxation time around 2-3 sec;
3. a short latency to return to the nominal length during the unload phase;
4. in average, the total elongation was ∼70 % of the nominal length.

In comparison with the commercial conductive rubber cord, the custom material has an electrical behaviour suitable with the project requirements, ensuring a fine measurement of the GLCS stretch, and thus vertical load changes. Moreover, no observable electrical changes were recorded during the bending of the material. In order to address the issue of the short latency to return to the initial length, during implementation a sensor pre-stretched of the ∼10 % of the nominal length is required.

6.5.4 Stretch Sensor - System Architecture

The polymeric transducer changes its physical and electrical properties in response to an external stimulus and this changes needs to be converted into an electrical signal through a dedicated Read-Out Circuit (ROC). The resistance variation is a continuous physical quantity that has to be interfaced with a digital system. Generally, a voltage divider coupled with an

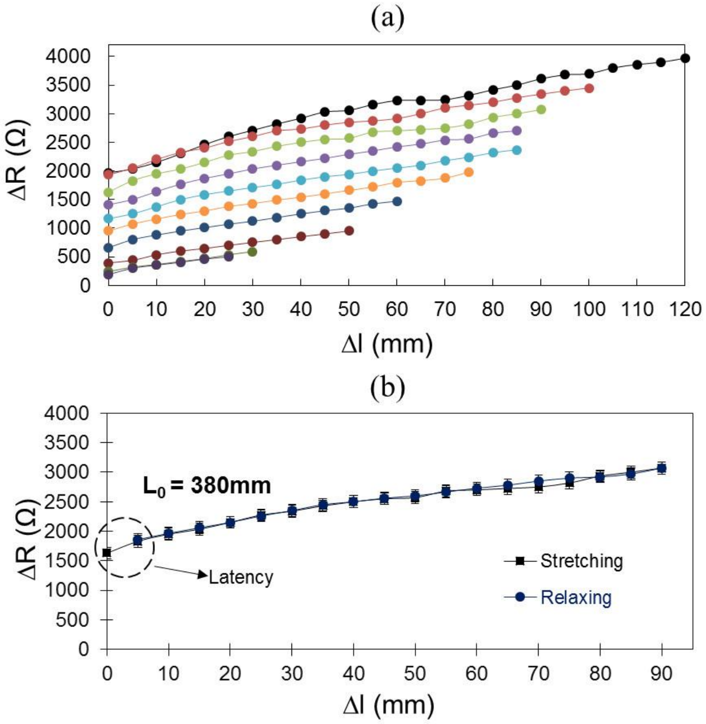

FIGURE 6.21: (a)Stretch sensor characterization at different nominal length. (b) Streching-Relaxing test

Analog to Digital Converter (ADC), converts a voltage quantity into a digital number. The conversion involves quantization of the input, so it necessarily introduces a small degree of error. Furthermore, instead of continuously performing the conversion, an ADC does the conversion periodically, sampling the input. The result is a sequence of digital values that are converted from a continuous-time and continuous-amplitude analog signal to a discrete-time and discrete-amplitude digital signal. With the proper mixed analog-digital approach it is possible to encode the analog information in the time-domain with a robust and reliable periodic digital signal. The quasi-digital approach is able to preserve the original information with high accuracy. The ROC, designed using a Schmitt Trigger oscillator, allows converting of an analog signal into a quasi-digital signal. The output is a square wave able to change its frequency according to the resistance value of the transducer.

Figure 6.22 depicts the SM system architecture comprised of the stretch sensor (ΔR_{sens}), the analog-to-quasi digital ROC (Δf output), the microcontroller, the Bluetooth module and the custom graphic user interface. The overall system was powered with a 3.7 V 200 mAh LiPo rechargeable battery coupled with a fixed 3.3 V voltage regulator.

The sensor was embedded within the GLCS with conductive thread providing the interface and the electrical connection with the ROC. Figure 6.23

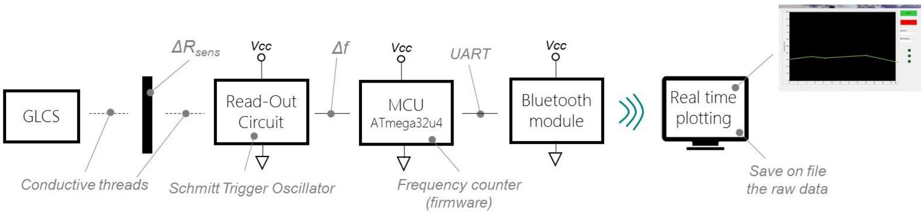

FIGURE 6.22: Stretch Monitoring system architecture.

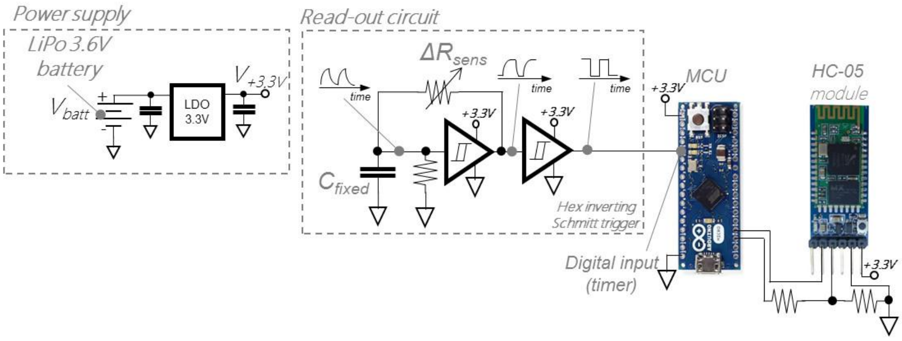

FIGURE 6.23: Circuit schematic of the SM system.

shows the circuit schematic of the system. The ROC is based on a Schmitt Trigger Oscillator in which the transducer is used as feedback element of the circuit. Schmitt trigger is a bistable multivibrator used as relaxation oscillator. This is achieved by connecting a single $R_{sens}C_{fixed}$ series between the output and the input of an inverting Schmitt trigger. The output will be a continuous square wave whose frequency depends on the values of R_{sens} and C_{fixed}, and the threshold points of the Schmitt trigger. Here, a comparator-based Schmitt trigger is used in its inverting configuration.

The HEF40106B hex inverter was used, which provides asix CMOS inverting buffer with high noise immunity, high bandwidth, high gain and excellent input/output characteristics producing a more "squared" output waveform compared with standard TTL logic gates. The inverting buffer switches at different points for positive-going and negative-going signals. The difference between the positive voltage (V_{T+}) and the negative voltage (V_{T-}) is defined as hysteresis voltage (V_H). The digital Schmitt trigger gate has a built-in hysteresis V_H (0.8 V) and the threshold voltages are (V_{T+}) (1.6 V) and V_{T-} (0.8 V). R_{sens} connects the circuit in a positive feedback loop necessary for oscillation. Figure 6.24 (a), (b) and (c) show the electrical characteristics of the HEF40106B with $V_{DD} = 3.3\,V$ and $V_{SS} = 0\,V$. The output changes with a propagation delay equal to 75 ns when the input voltage rises above 66 % and falls below 33 %. The capacitor in a Schmitt Trigger

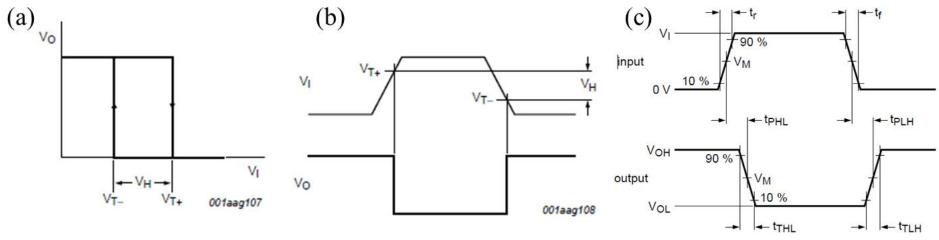

FIGURE 6.24: HEF40106B (a) trasfer characteristcs, (b) V_{T-}, V_{T+} and V_H waveforms definition and (c) delay propagation and output transition time.

Oscillator must charge to 66 % of rail voltage to make the output go LOW, then discharge to 33 % of rail voltage to make the output goes HIGH. The capacitor takes time to charge or discharge between these two values and this gives the oscillator a known frequency of operation. In addition to the first Schmitt Trigger output, a second inverter was used to square perfectively the output, with a inversion of the phase. Following the configuration proposed, the delay time variation (or frequency shift) is determined by the values of R_{sens}.

- when V_C is less than V_{T-}, V_O goes high (3.3 V) and starts charging the capacitor C through R_{sens};
- when V_C crosses the threshold voltage V_{T+}, V_O goes low (0.05 V) and the discharging of C through R_{sens} begins;
- when V_C crosses the threshold voltage V_{T-}, the initial step is repeated, generating an output oscillation.

The output frequency is given by the following Eq. 6.9

$$f = \frac{1}{t} = \frac{1}{t_h + t_l} \tag{6.9}$$

where the period t is the sum of the period when output is high t_h and when it is low t_l. To derive the frequency equation and in particular t_h and t_l the universal time constant formula (Eq. 6.10) for the RC circuit was used with the following parameters $V_{T+} = 2\,V$, $V_{OH} = 3\,V$, $V_{T-} = 1.5\,V$, $V_{OL} = 0.05\,V$ and $V_H = 0.5\,V$.

$$change = (final - start)(1 - e^{-\frac{t}{RC}}) \tag{6.10}$$

$$V_c(t) = V_f - (V_f - V_i)e^{-\frac{t}{RC}} \tag{6.11}$$

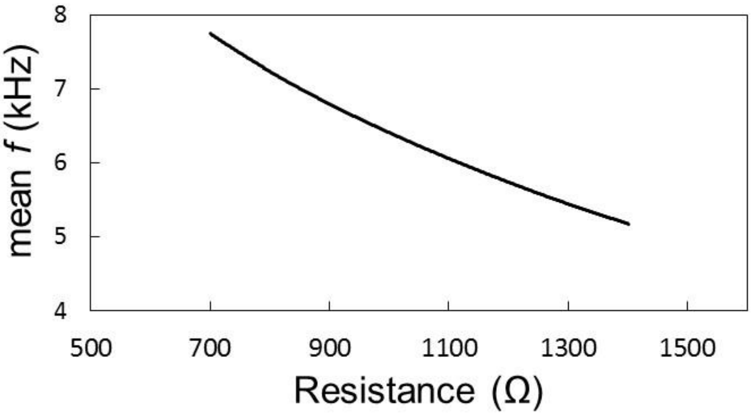

FIGURE 6.25: Schmitt Trigger simulation.

where $V_c(t)$ is the capacitor voltage change , V_f is the capacitor voltage at infinity and V_i is the initial voltage of the capacitor. The Eq. 6.10 can be written for t_h and t_l, as follow:

$$V_H = (V_{OH} - V_{T-})(1 - e^{-\frac{t_h}{RC}}) \tag{6.12}$$

$$V_H = (V_{OL} - V_{T+})(1 - e^{-\frac{t_l}{RC}}) \tag{6.13}$$

and respectively, $t_h = 0.26R_{sens}C$ and $t_l = 1.62R_{sens}C$. Considering the Eq. 6.9, the output frequency is

$$f = \frac{1}{t_H + t_L} = \frac{0.62}{R_{sens}C} \tag{6.14}$$

Figure 6.25 shows the LTspice simulation of the circuit with a frequency sweep from 700 Ω to 1400 Ω and step frequency of 1Hz.

6.5.5 Results and Discussion

The experiment performed using the set-up shown in Figure 6.26 (a). The Stretch Monitoring (SM) system with read-out circuit, MCU, Bluetooth Module and LiPo battery was assembled and integrated within a small "black box" with size of 65×27×27 mm (L×H×W) in order to be portable and attachable on one leg of the GLCS. The stretch sensor was embedded within the textile structure of the SkinSuit and connected with the SM system through conductive threads sewn within the elastic fabric. Two metallic snap-fasteners stitched with conductive threads provide a robust and comfortable electrical connection the SM system. A second stretch sensor has been embedded on the other leg of the SkinSuit and connected with a digital multimeter in order to compare simultaneously the ΔR and Δf variation during the experiment. The objective of the experiment was to prove the

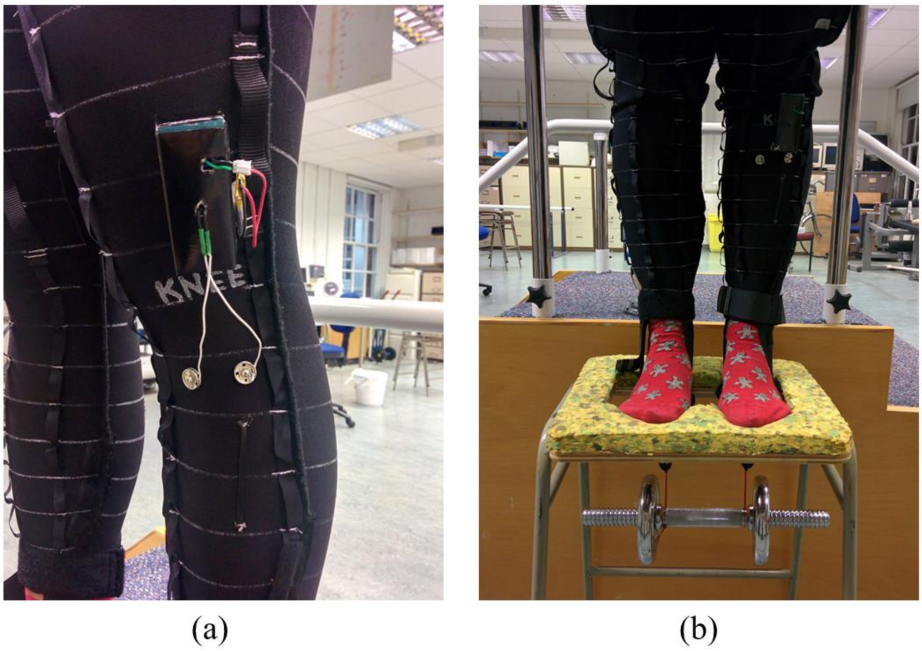

(a) (b)

FIGURE 6.26: (a) Stretch Monitoring system implementation on the GLCS. (b) Experimental set-up adjusting the Gz-load of the suit.

SM system effectiveness with different loads level. As shown in 6.26 (b), the subject with the SkinSuit was standing on a custom stool and different weights (0-17 kg of range) were hung on beneath to simulate different Gz-force. Through the custom user interface it was possible to monitor the real time load change through the SkinSuit.

Figure 6.27 depicts the results of the ΔR and Δf in relation with the force and length variations of the SkinSuit. Thanks to the previous characterizations, it was possible to determinate the amount of Gz force produced in relation with the length-force variation. The behaviour of the stretch sensor was almost linear for each leg. However, the friction between the skin and the suit had to be considered. Indeed, an increase of the stretch of the suit was obtained with a movement of the subject using a fixed weight. This aspect was measured by the sensor with a rapid variation of ΔR, and therefore Δf with a constant load. The system, powered with a 3.6 V 250 mAh LiPo battery provided a life time of 3 h with a continuous stream a rate of 10 Hz, adjustable from the user interface to save battery life or improving the data capture.

Thus, the SM system provides a real-time and potentially reliable monitoring of the Gz variation by the GLCS. Furthermore the system can be easily installed and removed from the SkinSuit if required during donning and doffing. A further integration of the electronics would enhance the efficiency of the system in terms of power consumption and overall size.

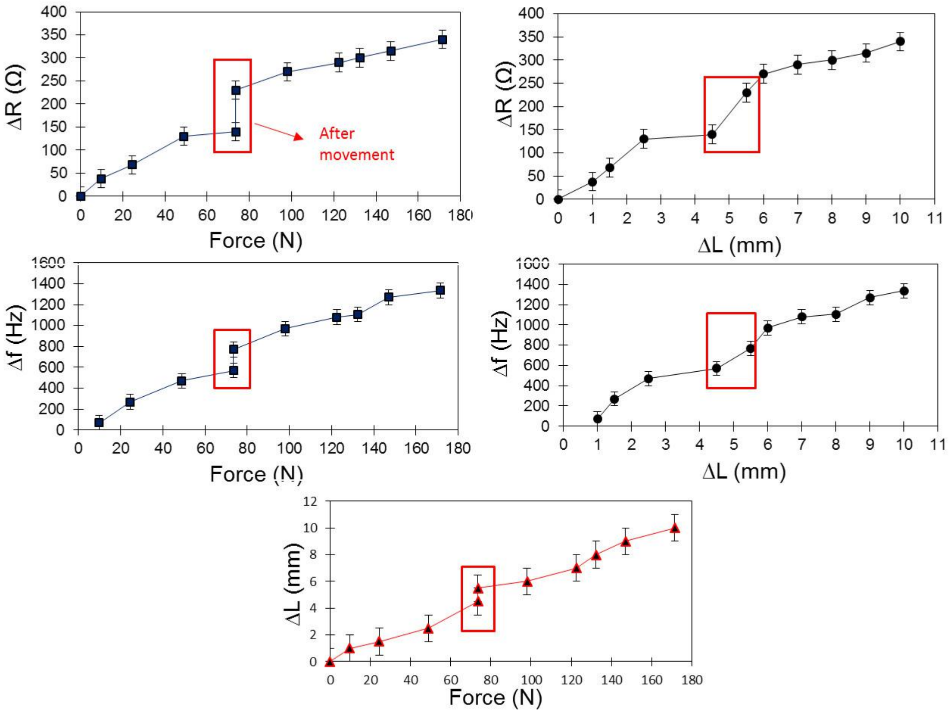

FIGURE 6.27: Stretch Monitoring system tests $(F - \Delta R)$, $(F - \Delta f)$, $(\Delta L - \Delta R)$, $(\Delta L - \Delta f)$ and $(F - \Delta L)$.

6.6 Spinal Elongation Monitoring System

Gravity affects the musculoskeletal system and in particular the spine. During sleep (4 - 8 h) the body can elongate 1.3 - 2 cm thought to be due to loss of a hydrostatic pressure gradient inducing intervertebral disc expansion. In space this process is increased resulting in up to 6.9 cm stature elongation. Currently, the spine elongation is monitored adopting standard measurement tools, such as stadiometer or tape measure. On board the ISS this analysis is usually assessed by repetitive measurements of the height, marked on the internal wall of the space module taking note of the elongation over time (Figure 6.28).

In this Chapter, a wearable, non invasive and integrated Spinal Elongation Monitoring (SEM) device is presented for potentially use in space. The system consists of a stretchable sensing material coupled with a custom electronic circuit directly attached on the body and, in particular, on the portion of the spine that has to be monitored. The round PCB circuit, with a surface area measured by $\sim 15\,cm^2$, provides a read-out circuit, able to convert the length variation of the sensor into a quasi-digital signal characterized by a frequency sensitivity, on average of $80\,Hz/mm$, and a low energy wireless communication based on Bluetooth Low Energy (BLE) or IR-UWB selectable with a physical switch, in order to allow a direct compare

FIGURE 6.28: Height measurements on board the ISS.

of efficiency and power consumption of the two transmission technologies. Two standard 55 mm ECG electrode (*Convidein ECG electrode*) were used to mount the sensors allowing a stable contact with the skin of the subject with low risk of irritation.

The main objective of the SEM system is to monitor autonomously spinal elongation involved by a novel 0-g simulator called Hyper-Buoyancy Flotation (HBF), designed by King's College London. With 5 h of experiment session, the spinal elongation was monitored in selective portions of the spine with an accuracy of 1 mm. The data are transmitted to the user interface in real-time mode, ensuring a direct and fine control of the elongation status. Two stretch sensors, connected to a multimeter and coupled with the SEM system, were used to record the elongation in thorax region (T2-T4 vertebrae) and lumbar region (T12-L2 vertebrae) of the spine, measuring respectively an average length variation of 3 mm and 5 mm during the experiment. .

6.6.1 Background

The exposure to microgravity induces significant deconditioning of the musculoskeletal and cardiovascular systems, that may compromise health and functionality in space (Convertino, 2009). Spinal elongation is just one of the factors that can also affect the safety and performance of a crewmember while in space. Spinal elongation occurs due to the lack of gravity/-compression on the spinal column. This may also induce flattening of the natural spinal curvatures. Lumbar back pain, also known as Space Adaptation Back Pain is a common symptom experienced by astronauts during early exposure to spaceflight (Thornton, Hoffler, and Rummel, 1977; Styf, Kalebo, and Hargens, 1994; Kerstman et al., 2012). Such pain has the potential to interrupt challenging in-flight tasks by reduction of restorative sleep and mental concentration. To date, there is lack of quantitative research addressing spinal adaptations and origins of lumbar back pain before,during and after spaceflight. The Flight Medical Clinical NASA Johnson Space Center concluded that among Shuttle orbiter crew members, the 68% report some degree of low back pain during spaceflight (Wing et al., 1991).

Therefore, to ensure an exploration class mission preserving astronaut's health, wellbeing and performance, effective countermeasures are urgently required (Young, 1999). During Apollo-Soyuz Test Project (ASTP) and Skylab, spinal elongation data was collected from a small number of subjects in a standing posture indicating a rapid increase in stature during the first few days of weightlessness, after which stature reached a plateau up to an increase of the 3% (Annis, 1978; Young and Rajulu, 2011; Bungo et al., 1987).

Whilst, devices such as Advanced Resistive Exercise Device (ARED), vibration isolated treadmill (T2) and Cycle Ergometer with a Vibration Isolation and Stabilisation System (CEVIS) are used for 2.5 hours of physical exercise to counteract the effects of the 0-g environment on the human body until recently back pain was neglected. More recently, 52% of the astronauts (Sayson et al., 2013), presumably secondary to the increased risk of disc injury (Johnston et al., 2010), a degeneration of spinal stabiliser muscles (Debuse et al., 2013) and stature elongation partly induced by saturated intervertebral discs and changes in spinal curvature (Sayson et al., 2013).

To acutely reduce back pain, the astronauts tend to adopt an embryonic flexion position. Height measurement is performed on the ISS with standard anthropometric tools, by marking the height on the internal wall of a space module (Figure 6.28). Several data were collected during last decades, especially with Skylab (Johnston and Dietlein, 1977), however selective spinal measurements have never performed, due to a practical challenges. On Earth, the height changes of intervertebral discs can be performed only with radiologic assessments (MRI or CT) but with the clear issue to simulate the weightlessness condition.

Vertebral column has 24 intervertebral discs interposed between the vertebral bodies: six in the cervical, twelve in the thoracic and five in the lumbar region, with one between the sacrum and coccyx (Figure 6.29). The discs account for approximately one-quarter of the total length of the vertebral column, and are primarily responsible for the presence of the various curvatures. On descending the vertebral column, the discs increase in thickness, being thinnest in the upper cervical region and thickest in the lower lumbar. In the upper thoracic region, however, the discs appear to narrow slightly. In the cervical region the disc is about two-fifths the height of the vertebrae, being approx-imately 5 mm thick. In the thoracic region the discs

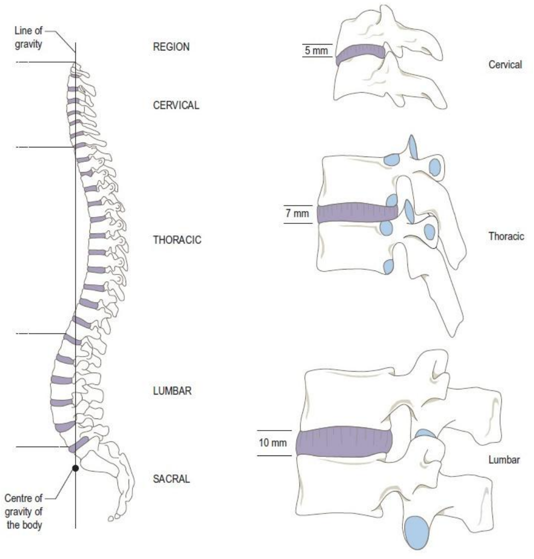

FIGURE 6.29: Vertebral column anatomy.

average 7 mm in thickness, so that they are one-quarter of the height of the vertebral bodies. The discs in the lumbar regions are at least 10 mm thick, equivalent to one-third of the height of the lumbar vertebral bodies. The relative height of the disc to the vertebral bodies is an important factor in determining the mobility of the vertebral column in each of the regions. Individual discs are not of uniform thickness; they are slightly wedge-shaped in conformity with the curvature of the vertebral column in the region of the disc. The curvatures in the cervical and lumbar regions are primarily due to the greater anterior thickness of the discs in these regions (Liem et al., 2001).

6.6.2 System Architecture

The Spinal Elongation Monitoring (SEM) system comprises of a piezo-resistive stretch sensor, a read-out circuit, a wireless low power data transmission and a re-chargeable battery. Figure 6.30 shows the System Architecture able to select the wireless communication technology to use, between Bluetooth Low Energy (BLE) and Impulse Radio-UlraWide Band (IR-UWB). This approach allows data to be transmitted for a short-range with a low power consumption, coupled with a compact design of the system. Furthermore, a double communication system allows is to be suitable with the Bluetooth receivers used by European Space Agency on the ISS and, thanks the IR-UWB technology, to provide a lower power consumption in compare with BLE for the next generation of wearable device. The overall system has to be placed directly on the back in a precise portion of the spine to be investigated.

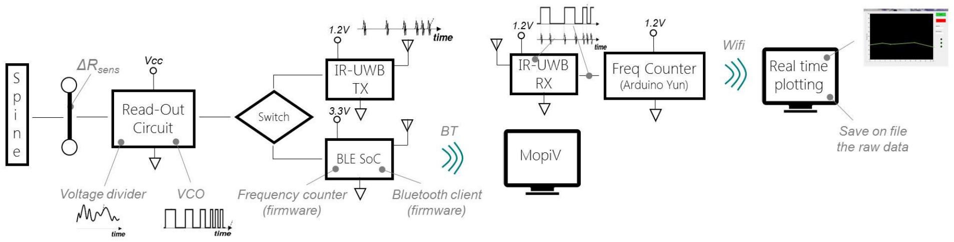

FIGURE 6.30: Spinal Elongation Monitoring (SEM) system architecture.

The elongation of the selected region of the spine is recorded by the stretch sensor that is able to change its electrical resistance (ΔR) proportionally yo its axial deformation. The sensing material was chosen in order to be compliant as much as possible with the stiffness of the skin. The ΔR produced under spine elongation is converted with a voltage divider into a voltage variation (ΔV), becoming the input of the Voltage Controlled Oscillator (VCO). The VCO generates an output oscillation frequency by the voltage input and in particular a frequency modulation due to the ΔV input. The result is a quasi-digital signal (as explained in Chapter 2) able to encode the analog information into a digital frequency variation ensuring a reliable and high noise immunity signal output. Then, selecting the IR-UWB communication, as presented in Chapter 3, the VCO output is able to digitally trigger the generation of low energy pulses (30 pJ energy per transmitted pulse) from the IR-UWB transmitter with a 3.5 GHz of center frequency and bandwidth ranging of 300 MHz-500 MHz. The information transmitted needs a IR-UWB receiver able to regenerates the modulated signal and, with an external Micro-Controller Unit (MCU) to process the data.

Conversely, a SoC BLE−MCU provides a fully integrated solution with a pre-processing of the VCO signal, recording the frequency shift, and with a previous pairing process, a packet-based Bluetooth communication with other Bluetooth devices, used as receiver. Despite this integrated solution, this advantage is mitigated from the higher power consumption than IR−UWB, as presented in Chapter 3. Finally, the results of the experiment are plotted in real time on a custom user interface wrote in C#, which is also able to save the raw data of the length variation of the sensor.

6.6.3 Material Characterization

According to the experiment objectives, two different regions of the spine (thorax and lumbar) were monitored during a flotation experiment. The nominal length of the sensors have to be consistent with the anatomy of the spine involving selectively of 3-4 vertebrae, through anthropometric data

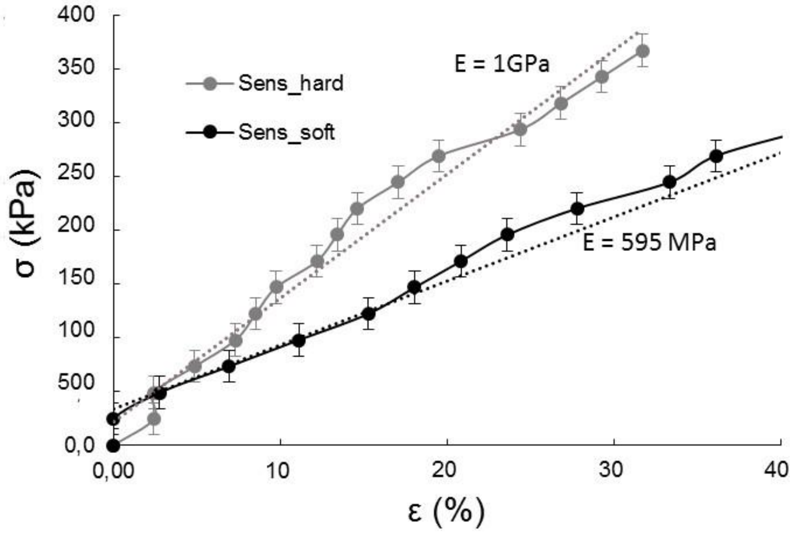

FIGURE 6.31: Spinal Monitoring sensor characterization of the stretch sensor v1 (hard) and v2 (soft) – Stress–strain curve.

(Cramer and Darby, 2013). The nominal length selected were 40 mm and 60 m for the thorax portion (T2-T4 vertebrae) and the lumbar portion (T12-L2 vertebrae), respectively.

The first approach was to develop the sensor using the same piezoresistive material used for the "Stretch monitoring system". However the stiffness of the material was greater then mechanical compared with mechanical properties of the skin. As human skin shows a heterogeneous, anisotropic, viscoelastic and non–linear stress–strain relationship (Agache et al., 1980), thus a stretch sensor with a low elastic module (E) around 100–500 MPa is needed to prevent an elastic return phenomena of the material when it is placed on the skin. The conductive silicon material, based on Wacker Elastosil® R 570/50, was selected to improve the mechanical properties of the sensor maintaining a linear electrical resistance variation under strain. Experimental set-up in which calibrated weights, a callipers and a digital multimeter was used to characterize two thin stripes of piezo–material with a nominal length of 40–60 mm and a section area of 4 mm^2. To reduce the stiffness of the sensor, as close as possible with average skin stiffness, the Young Modulus of the sensing material was measured. Figure 6.31 shows the stress-strain curve of both materials highlighting a lower Young's modulus (E) of the new material in comparison with the previous sensor. The Young's modulus is a measure of the stiffness of the material and it is defined as the relationship between the tensile stress (σ) and strain (ε) in the elastic field, as shown by the Eq. 6.15,

$$E = \frac{\sigma}{\varepsilon} = \frac{\frac{F}{A_0}}{\frac{\Delta L}{L_0}} \tag{6.15}$$

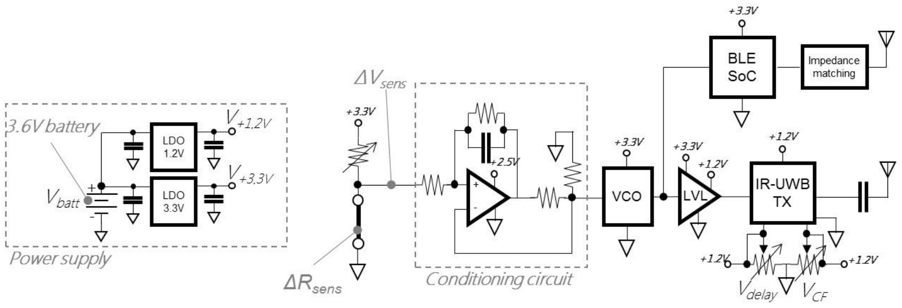

FIGURE 6.32: Block scheme of the SEM system.

where F is the force exerted on the material under tension, A_0 is the actual cross-sectional area through which the force is applied, ΔL is the amount by which the length of the material changes and L_0 is the original length.

Furthermore, the elastic deformation limit was improved reaching the 62% of the nominal length in compared with the previous 31%. Finally, as shown by Figure 6.31 a piezo-electric characterization for both 40 and 60 mm sensors was performed with different calibrated weight. Resistance sensitivity under stress of $61\,\Omega\,mm$ and $82\,\Omega\,mm$ for 40 and 60 mm length sensors, respectively, was measured. These results allow to calculate the amount of resistance shift during the stretch phase, required to determinate the spinal elongation.

6.6.4 Demonstrator and Implementation

A. Hardware Design

Figure 6.32 shows the block scheme of the SEM system. In order to optimize the PCB size, SMD components with a 0402 package for passive components and a QFN, SOT23 and TSSOP package for active components was selected. The system is supplied with a 3.6 V LiPo rechargeable battery with 150 mAh capacity connected with a standard 2-pin JST-PH connector to the PCB board. Then, two linear voltage regulators (Low DropOut regulator−TPS71712/33) with a fixed voltage of 1.2 V and 3.3 V supplies respectively the IR-UWB IC transmitter and the read-out circuit plus BLE−MCU SoC. The ΔR_{sens} applied to the voltage divider generates a ΔV_{sens} that was adapted to the input range of the VCO through the 20 kΩ trimmer R_T. The VCO is a LTC6990 voltage controlled silicon oscillator capable of operating in 488 Hz−2 MHz frequency range and providing <1% frequency drift across 0−100 $°C$, thanks to the dedicated conditioning circuit, as widely explained in Chapter 3.

A SMD slide switch allows selecting the IR−UWB or BLE wireless technology. With the IR−UWB, the output of the VCO which has an amplitude

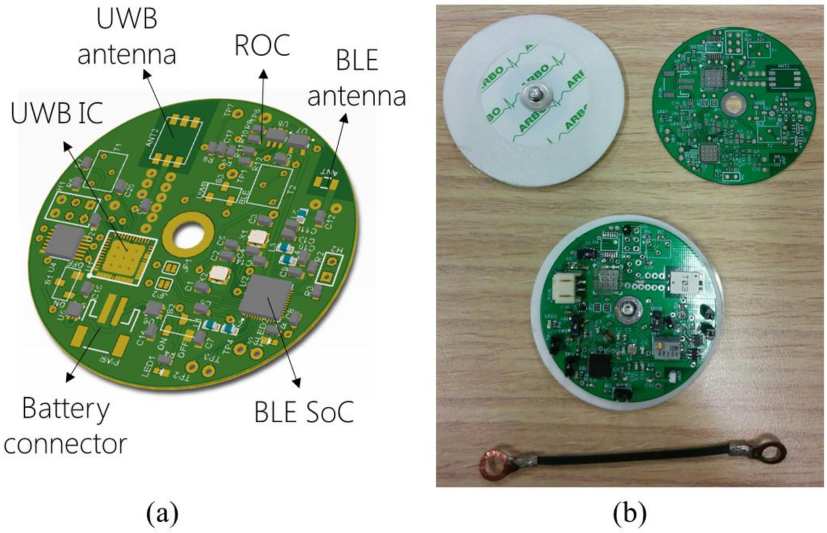

FIGURE 6.33: (a) SEM system altium design. (b) SEM system PCB and assembly

of 3.3 V has to be adapted since the UWB chipset works at 1.2 V. A bidirectional logic level translator (ADG3304) with $V_{CCY} = 3.3\,V$ and $V_{CCA} = 1.2\,V$ used to shift the voltage level of the oscillating signal from 3.3 V to 1.2 V. The UWB IC presented in Chapter 3, implements a flexible UWB pulse generator triggered by the VCO signal. The chip antenna (Tayo Yuden) filters the UWB signal in the 3.1−10.6 GHz band. The system provided two analog controls V_{DELAY} and V_{CF} to set the pulse duration and the center frequency f_c. The integrated transmitter consumes a measured 30 pJ energy per transmitted pulse.

Conversely, selecting the BLE communication system, the VCO signal flows directly to the GPIO pin of the commercial Bluetooth SoC (Nordic nRF51822). It is a flexible multiprotocol SoC ideally suited for Bluetooth Low Energy wireless applications. The nRF51822 is an ultra-low power 2.4 GHz wireless SoC integrating a 2.4 GHz transceiver, a 32 bit ARM® Cortex^{TM}-M0 CPU, a flash memory, and 31-pnins analog/digital peripherals. A well designed PCB is necessary to achieve good RF performance, in particular the RF matching network, since a poor layout can lead to loss in performance or functionality. Especially in the case of the antenna matching circuitry (components between device pins ANT1, ANT2, VDD-PA and the antenna), any changes to the layout can alter the behaviour of the SoC, leading a degradation of the RF performance.

All the reference circuits are designed for use with a 50 Ω single end antenna. A matching network is needed between the differential RF pins

ANT1 and ANT2 and the antenna, to match the antenna impedance (normally 50 Ω) to the optimum RF load impedance for the chip. The DC supply voltage has be decoupled as close as possible to the VDD pins with high performance RF capacitors. Following the *Antenna matching network requirements* of the component, the matching network is a Π-network. It consists of three components in a Π-configuration:one shunt C_{11}, then one in series L_5, and finally another shunt C_{12} (See schematic in Appendix). The optimum differential impedance at 2.4 GHz seen into the matching network from pin ANT1 and ANT2 on the QFN48 package is $(15 + j85)\Omega$, which is obtained following the *Antenna tuning* document, provided by the Nordic Semiconductor company, with $C_{11} = 0.8\,pF$, $L_5 = 3.3\,nH$ and $C_{12} = 1.5\,pF$. Finally a 2.4 GHz multilayer chip antenna (Wurth Elektronik) provides the Bluetooth transmission with an average gain of -0.5 dBi and an omnidirectional radiation pattern. Figure 6.33 shows the PCB, which was designed respecting the following requirements:

- a double layer PCB with a widespread ground plane for both layers;
- a ground plane clearance around the antenna area (following the antenna datasheets constraints);
- only one layer of components to ensure a flat bottom surface;
- a round shape with a $\oslash < 45\,mm$, compliant with the standard size of the ECG electrodes, used as mechanical support;
- a hole in the middle of the PCB provides a mechanical connection between the sensor and the ECG electrodes, through a metallic snap button.

B. Firmware Design

The following paragraph describes in depth the logic adopted to compute the frequency of the signal coming as input in the system. The firmware encodes the frequency oscillation of the VCO signal (V_{VCO}) and transmits the data via Bluetooth. More precisely, a General Purpose Input Output pin as input pin was used and the MCU was set to trigger an interrupt every time a rising edge is seen on the input pin. In addition, a 16 bit internal timer has been taken into account to keep track of the sampling rate of the signal. In terms of software, the mBed library for the nRF51822 has been chosen. The Nordic timer is configured so to execute a really small piece of code which increments the value of a counter variable every $10\mu s$. When the MCU sees the first rising edge it sets the counter variable to zero whereas, when the MCU sees the second rising edge, it computes the time delta, in terms of samples, and it transforms the result in Hz according to the formula below:

$$f = \frac{1}{(nCounts \cdot sample\, rate)} \tag{6.16}$$

where f is the frequency and $nCounts$ the number of counts. The code reported below initiates the system by creating the timer object, configuring the pin 23 as an interrupt input pin, setting the $tCount$ variable to zero and finally the setting the $seenRisingEdge$ to zero meaning that no rising edges are seen yet. Finally, the code starts the timer and register the input pin with the interrupt handler.

```
Ticker ticker;                              /* The timer object.
InterruptIn extSignal(p23);                 /* The signal to sample
/* comes to the pin 23.
static volatile uint32_t tCount = 0;        /* Samples counter.
static volatile uint8_t seenRisingEdge = 0; /* Set to 1 when a rising
/* edge is seen.

extSignal.rise(&signalDidRiseEdge);

ticker.attach_us(periodicCallback, SAMPLE_RATE_IN_us);
```

The code of the "periodicCallback" function is hereby reported.

```
void periodicCallback(void)
{
    tCount++;
}
```

As the reader may notice, the function increments the tCount variable and returns the program flow to the caller. As above mentioned, when a rising edge is seen on the input signal pin, an interrupt is fired. The MCU handles such an interrupt by executing the code below:

```
void signalDidRiseEdge(void)
{
    if(seenRisingEdge==1) {
        /* period is a global variable */
        period = tCount * SAMPLE_RATE_IN_us;
    }
    tCount = 0;
    seenRisingEdge = !seenRisingEdge;
}
```

The code above computes the signal period only when a rising edge of the input signal was recorded. If no rising edges were recorded, it just sets to zero the tCount variable. The period of the signal is later converted into a frequency and written to the Bluetooth Characteristic of the MCU that

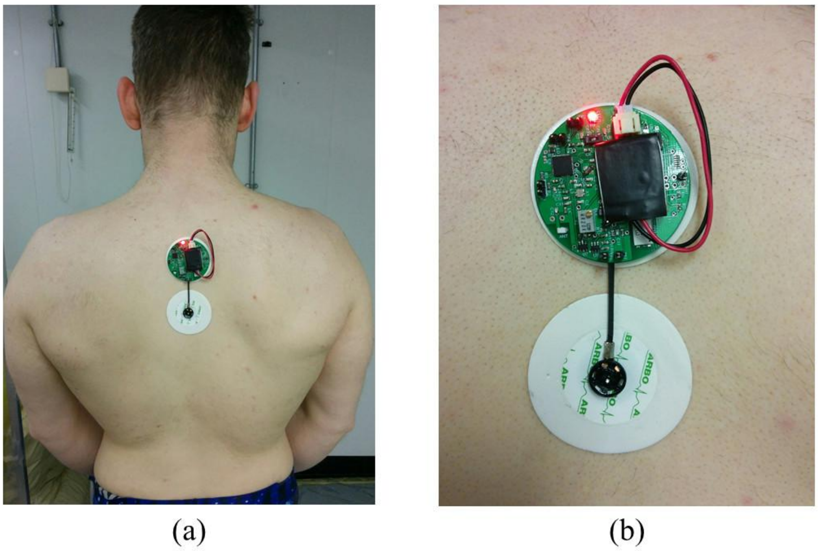
(a) (b)

FIGURE 6.34: SEM system preliminary test.

emulates a UART port. Finally, the code below performs the BLE write.

```
void signalDidRiseEdge(void)
void writeDataToBLE(const uint8_t *data) {

    if (data!=NULL && uartServicePtr!=NULL) {
        uint16_t dataSize = strlen((char*) data);
        ble.updateCharacteristicValue(uartServicePtr->
        getRXCharacteristicHandle(), data, dataSize);
    }
}
```

C. Implementation

Figure 6.34 depicts the final implementation of the SEM system coupled with the stretch sensor and the ECG electrodes. During the positioning step, the sensor was pre-stretched in order to enhance the stretching-relaxing hysteresis, as explained in Paragraph 6.5.3. Two custom "hooks" provide a robust connection of the sensor with the system, since the movements of the subject and the low stiffness of the skin can affect the mechanical stability of the device and the signal quality. A small LiPo battery (3.6 V 120 mAh) powers the system and it is placed on the top of the PCB.

6.6.5 Test and Results

A. Preliminary Tests

Preliminary tests of the overall system were performed placing between T1-T3 vertebrae (Figure 6.34) and testing the BLE and IR-UWB communication. The tests reported in Light-of-Sight (LoS) propagation of a maximum

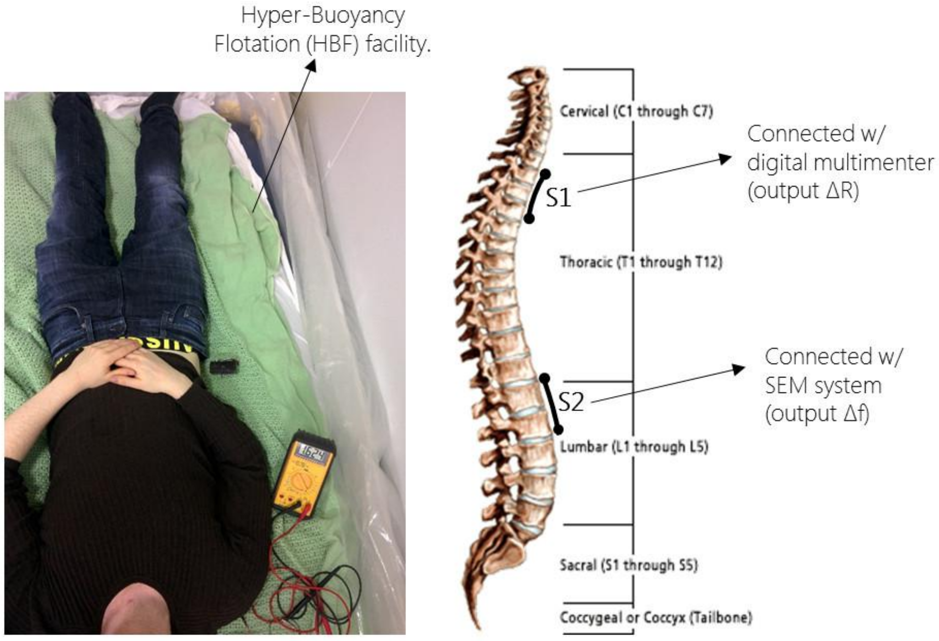

(a) (b)

FIGURE 6.35: Placement of the S1 and S2 stretch sensors.

range of 15 m and 1 m using the BLE and UWB modules, respectively. As BLE receiver was used a smartphone using the Received Signal Strength Indication (RSSI) with the dedicated mobile App. The UWB receiver (RX) presented in Chapter 4 was used to evaluate the maximum transmission distance considering the Pulse Error Rate. In terms of power consumption in transmission mode, the BLE SoC consumes 50 mW w.r.t. to the 15 mW of the IR-UWB IC (in agreement with the results presented in Chapter 3). The Read-Out Circuit (ROC) was identical for both communication systems, reporting a power consumption of about 8 mW. These preliminary tests allowed also to validate the robustness of the SEM system after movements of the subject such as flexion, hyperextension, lateral flexion and rotation of the torso. No disconnection was observed during any movement.

B. Spinal Elongation Experiment

The elongation of the spine was simulated with the Hyper-Buoyancy Flotation (HBF) facility. It was designed and implemented at King's College London (KCL). It comprises a hypersaline-filled water-bed developed to simulate a short term high fidelity model of spinal unloading. It allows to investigate the pathophysiology and develop techniques to ameliorate microgravity induced spinal elongation and associated back pain. In accordance with past tests, 4 hr of HBF experiment recorded an stature elongation of $\sim 18\,mm$ due to the increase of the intervertebral disc "height" during spinal unloading. In a single subject trial, the SEM device was set in

Bluetooth streaming mode, in order to be compliant with the receiver devices within the KCL facility. The SEM system was used for 5 hours of HBF experiment subdivided into three steps:

1. 4h 45′ lying on the HBF facility (interrupted with a break of 10 min);
2. 10′ sitting on a chair;
3. 15′ lying on a normal bed.

This protocol was chosen in preparation for the next 8 hr HBF experiment followed by a MRI scan, in order to evaluate the structures of the spine preciously. For this reason, it also is relevant to investigate the behaviour of the spine during the carriage of the subject between the HBF facility to the hospital imaging department.

The stretch sensors, placed on the back of the subject, were pre-stretched of the 10% of the nominal length. The thoracic sensor was connected with a digital multimeter, to measure the resistance change, and the lumbar sensor was connected with the SEM system. Finally, the (ΔR_{sens} and Δf_{osc}) were converted into a length change of the selective spine portions. Elongation of the spine region and thus stretch of the sensor, causes an increasing in its electrical resistance and a decreasing the frequency of the ROC signal output.

Figure 6.36 (a) shows the mean resistance variation of the thorax sensor every 15 min. The same procedure was used with the lumbar sensor, calculating an average of 100 samples within a measurement window of 10 sec every 15 min. The Figure 6.36 (b) plots the mean frequency of the signal. Both graphs present a subdivision into the different phases of the experiment, and in detail:

- $phase\,(A)$ – lying prone on the HBF;
- $phase\,(B)$ – rising from the HBF and standing up;
- $phase\,(C)$ - returning to the lying down on the HBF;
- $phase\,(D)$ – sitting on a chair with back at $90°$;
- $phase\,(E)$ – lying down on the bed.

In terms of elongation, the expected results are a constant increase of the resistance and a constant decrease of the signal frequency, respectively, specially during $phase\,(A)$, $phase\,(C)$ and $phase\,(E)$. Figure 6.36 (a) shows an complete opposite behaviour with a gradual decrease of the resistance, thus technically, a compression of the sensor, followed by a rapid increase when the subject stood up (phase (B)). Then, after the break, the phase

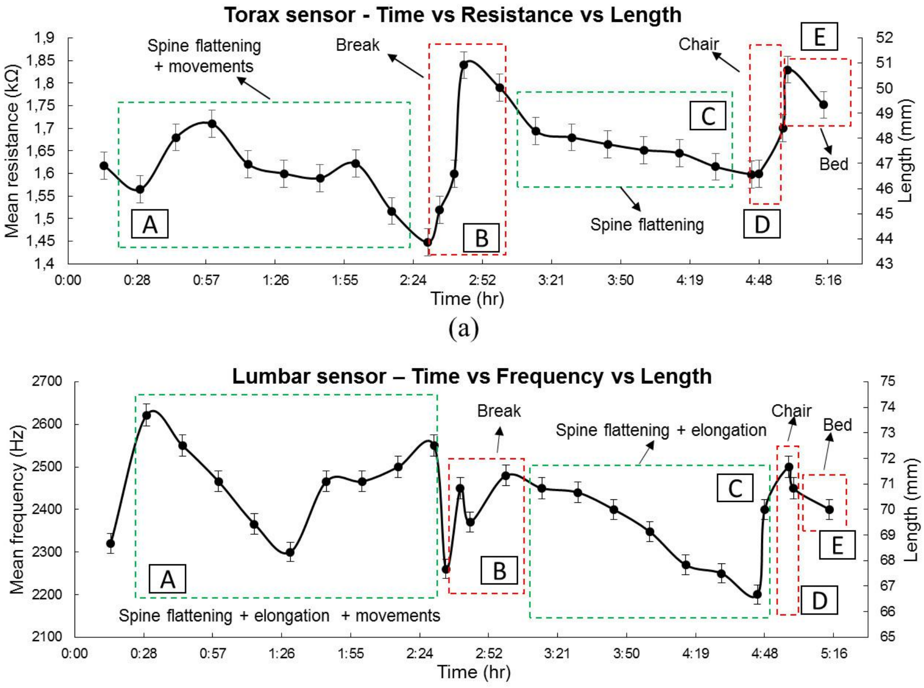

(a)

(b)

FIGURE 6.36: SEM system results after 5hr floitation test. (a) Resistance variation and (b) frequency variation with the spinal elongation.

(C) presents the same trend, up to the phase (D). The reason of these controversial results are due to the “spine flattening” process during the first part of the experiment. The kyphosis curvature tends to reduce its radius of curvature during the experiment. The sensor, previously stretched and positioned on the apex of kyphosis, begins to reduce its length during the "elongation phases" of the experiment. In that region of the spine, the intervertebral distance is less than the lumbar portion, therefore the contribution of the elongation mainly comes from the “spine flattening”, rather than from the increase of the intervertebral disc "height". A smoothness decrease of the resistance has been recorded when the subject slept (phase (C)), unlike the phase (A) that it is affected by motion artefacts. The thorax sensor, attached on the back with the subject in lying down position, measured a maximum displacement of 5 mm.

Figure 6.36 (b) depicts the results of the lumbar sensor in which, motion artefacts aside, shown an expected trend with a gradual increase of the sensor length during phase (A), (C) and (E). Opposite tendency during phase (B) and (D) when the subject stood up. Observing the graph, the transition between the $A - B$ and the $C - D$ phases was very quick and the spine tried to return slowly to the original condition. Likewise with the lumbar sensor, a slight “spine flatting” was observed coupled with an increase of the intervertebral spacing, since the sensor was placed just over the peak of the spine curvature. The amount of the stretch recorded was around 7 mm.

6.6.6 Conclusion

In this Chapter, the first wearable and no invasive device able to measure selectively elongation of the spine (Spinal Elongation Monitoring system) has been presented. The device was developed with a stretchable piezoresistive material coupled with a custom electronic circuit directly attached on the body of the subject. Two different short-range and low power consumption wireless technologies were implemented within the same system, with the opportunity to switch between them. BLE and IR-UWB short-range technologies were selected for their compact chipset (QFN package), low power consumption, short list of extra components and simple interface with the relative receivers. The results of the preliminary tests demonstrated the efficiency of the system of both wireless module with a wider range of transmission with the BLE (15 m) and a lower power consumption obtained with the IR-UWB (15 mW (TX)). Then, the mechanical robustness of the overall system was tested considering the issues due to movements and the soft and uneven surface of the back. The results of the experiments allowed to study the behaviour of the spine during unloading, showing that the elongation may occurs in the lumbar area where anatomically the nominal height of the vertebrae and intervertebral discs are higher than the thorax area. In both cases, it seems that the elongation was preceded by a flattening phenomenon which was prevalent observed on the thorax area, given that the sensor was placed at the apex of the kyphosis curvature. The sensor, pre-stretched during the experiment preparation, measured a untrue "compression" of the spine during the experiment session due to the flattening phenomenon. Finally, during the phase (D) and (E) of the experiment, the length of the spine changed rapidly mainly due to the recover of the anatomical curves of the back.

The SEM system had demonstrated the chance to monitor the behaviour of the spine during unloading selectively, providing a scientific support for the next steps of the research activities which will include a MRI analysis and a long-term bed-rest experiments with and without the GLCS.

Chapter 7

Conclusion

In this thesis work, a scientific contribution for the next generation of wearable technologies were presented, with a particular focus on circuit design of ultra-low power wireless technologies, the realization of smart piezoresistive / piezocapacitive and electro-active material, the design of read-out circuits and system integration/implementation. The research activities were carried out following an "application driven" approach, addressing the diverse challenges with a multidisciplinary method. This thesis begins with the establishment of the research area. Due to the interdisciplinary nature of the research topic, general requirements and challenges were presented, then the following chapters were structured with: I) a dedicated introduction in order to figure out the challenge to address, II) the solution proposed, III) characterization/tests, IV) experimental results and V) conclusions and discussion of the results.

In Chapter 2, the first objective was to combine a smart sensor, based on a piezo-capacitive polymer, and a custom read-out circuit within a fabric substrate. The transducer and the circuit were designed, developed and characterized in order to be compliant with the project requirements. The result was a compact and fully integrated sensor system, able to identify a contact event with a pressure resolution of 10 kPa and, at the same time, able to measure a pressure variation up to 4 MPa. The touch-pressure characteristics, the small design of the ROC, placed directly beneath the transducer, and the final fabric integration represents a novel contribution with respect to the similar commercial, bulky and stand alone pressure and/or touch systems.

In terms of short-range ultra-low power wireless communication systems for wearable technologies, in Chapter 3 a novel IR-UWB systems was presented. Requirements, challenges and current solutions among the wearable WBAN devices, mainly based on Bluetooth technology, were introduced. The IR-UWB (TX/RX) proof-of-concept designed and developed was able to demonstrate the streaming of a complex signal, such as an audio signal, with a radio range of 2.5 m and with a very low power consumption, equal to 7.52 mW (TX) and 32.4 mW (RX) respectively. The results allowed to prove the effectiveness of the IR-UWB as a real wireless technology alternative for the next generation of wearable WBAN devices.

In Chapter 4, the IR-UWB was used to develop a low-complexity ultra-low power Face-to-Face detector and, at the same time, a proximity sensor. Current solutions were introduced pointing out the high power consumption of the technology used, the presence of an external infrastructure, the proximity techniques adopted and the overall size. The final objective was to monitor the Doctor-Patient interaction during the hospitalization with relevant interest also about the human proximity. The final application is aimed to a deep investigation of the infections spreading behaviour within the hospital community. A proof-of-concept was designed and developed exploiting the IR-UWB with a Pulse-Error-Rate approach to evaluate the TX-RX distance. The TX-RX system proposed was able to detect the Doctor-Patient interaction with a range of 50 cm and to measure the relative distance with a 2-D spatial accuracy of 3 cm. The information was streamed to a graphical user interface able to count the number of interactions and to show the proximity. The transmitter, connected with a portable device (e.g. smartphone), or with further improvements in the stand alone configuration, consumed 10.8 mW with an autonomy of 8 h with a 120 mAh rechargeable battery.

In terms of wearable actuators, a novel contribution for the next generation was discussed in Chapter 5. ElectroActive Polymers, and in particular Dielectric Elastomers, are representative of a class of smart materials that are able to produce a deformation by applying a voltage. This technology was introduced and the relative technological challenges were detailed. A new concept of EAP geometry inspired by the muscle architecture and a proof-of-concept of the EAP working principle based on dielectric elastomer was presented in this Chapter. A deep analysis of the EAP multilayer configuration, well known among the scientist community, in addition to the application of different voltages for each layer, led to relevant improvements within the soft actuator technology. A fine control of the deformation and lower driving voltage were part of these improvements with respect to the literature. Since an excessive increase in the number of layers can lead to a stiffening of the actuator, the coaxial geometry aimed to solve this issue. Increasing the surface area of the electrodes, a performance improvement was obtained without affecting the mechanical properties of the material. Furthermore, a coaxial structure allowed to develop active fibers, which can be potentially woven within a fabric, filling the gap of the wearable man-machine interface. This solution was patented and brought to a further level of innovation, taking inspiration from the natural muscle anatomy. In principle, a multi-fibers coaxial configuration would allow a further improvement of the EAP fibers performance, introducing the possibility to control the strength and movement of the fiber with a selective activation of the fibers, as it happens in muscle fibers.

In the end, in Chapter 6 it is represented a scientific collector of the previous experiences within the wearable technology field. The research activities carried on within the Gravity Load Countermeasure Skinsuit (GLCS) project had the objective to turn the SkinSuit from a passive into an active wearable countermeasures system and to monitor the effects of the microgravity on the spinal column, by means of a novel wearable device. An explanation of the background of the physiological effects on the human body due to the space environment and the State Of the Art (SoA) of the current countermeasures was presented.

The first solution proposed was a Gz-load adjustment mechanism designed to change the stretch level of the SkinSuit. The overall mechanism was developed, tested and characterized with an ad-hoc GLCS simulator.

Then, in order to monitor the Gz-load variation, the first approach was to use a force sensor placed beneath the feet and integrated with the SkinSuit stirrups (Load Monitoring System). The Force Sensing Resistor (FSR) technology was selected as the best force sensor candidate in terms of force range, sensitivity, geometry and simple integration with the wearable system. The sensor was then characterized before the final integration, showing a sensing behaviour compliant with the project requirements. Then, the sensor coupled with a read-out circuit, was tested with the GLCS simulator. The results were unreliable with a poor repeatability, mainly due to the anatomy of the foot, to the flexibility of the stirrup and to the slight movements of the sensor.

These results led to consider another approach, exploiting the elastic properties of the SkinSuit and using a wearable stretch sensor (Stretch Monitoring System). The Mark V SkinSuit was characterized in terms of $stretch-Gz$-load variation in other to select the right placement of the stretch sensor. After a technical benchmark of the commercially available solutions, a custom stretch sensor based on a piezo-resistive polymeric material was developed and characterized. The sensor, connected with a read-out circuit based on a Schmitt trigger oscillator, was able to generate a quasi-digital signal, shifting the frequency of the square wave in response to a deformation of the sensor. The information was processed and transmitted via Bluetooth to a custom user interface. The sensor was embedded within the Mark V SkinSuit using conductive threads in order to fix it in position and to connect the sensor with the electronic module. Finally, the overall system was tested with different Gz-loads and the results presented an almost linear stretch behaviour, both in resistance and frequency variation with different static loads.

In the end, the first wearable and not invasive device able to measure selectively elongation of the spine (Spinal Elongation Monitoring system) was presented. The device consists of a stretchable piezo-resistive material coupled with a custom electronic circuit directly attached on the body of the subject. The circuit was able to encode the length change of the sensor into a frequency shift through a ROC based on a VCO. Then, BLE and IR-UWB technologies were both selected for short-range and low power consumption wireless communication and implemented within the circuit. This allowed to compare directly both technologies in terms of performance and energy efficiency, to interface the device with an existing wireless system using BLE and to set the device for the next generation of wearable wireless technology through the IR-UWB. The results of preliminary tests demonstrated the efficiency of both wireless module with a wider range of transmission with the BLE (15 m) and a lower power consumption obtained with the IR-UWB (15 mW (TX)). From the point of the sensing material, a new piezo-resistive stretch sensor was developed and compared with previous ones. The mechanical robustness of the overall system was tested considering the issues raising from the movements and the soft and uneven surface of the back. The results of the experiments allowed to study the behaviour of the spine unloading condition, showing that the presumably most likely elongation occurs mainly in the lumbar area (7 mm) in which, anatomically, the nominal height of vertebrae and intervertebral discs is higher than in the thorax area (5 mm). In both cases, the elongation was preceded by a flattening phenomenon which was mainly observed on the thorax area, given that the sensor was placed at the apex of the kyphosis curvature. In fact, the sensor, pre-stretched during the experimental set up, measured a false "compression" of the spine during the experiment due to the flattening phenomenon. The device performed continuously for 5 h saving the measurements every 15 min. This last scientific contribution allowed to collect together the competences, knowledge and results of the previous activities by designing, developing and testing on field a new wearable devices.

As a final consideration, the vision of wearable computing describes future electronic systems as an integral part of our "everyday clothing", serving as intelligent personal assistants. Therefore, such wearable sensors must maintain their sensing capabilities under the demands of normal clothes, which can impose severe mechanical deformation of the underlying garment, fabric substrate or human skin. The potential applications are several and wearable technologies have a direct link with human body monitoring. “Clothes are our own personal house” (Van Langenhove et al.,

2007) and there is no other device continuously in contact with the human body like garments. This way, the combination of smart materials, wearable electronics, low-power wireless technologies, sensors and the systems integration within a fabric or a human body, must be put together to understand the new generation of wearable devices. Textiles and clothes can be produced on fast and productive machinery at a reasonable cost, and the health and beauty industry is also taking advantage of these innovations.

Finally, the vision behind the current and near-future wearable technology, like in this thesis, is based on a highly multidisciplinary approach with an objective aimed at the final application, addressing and solving manifold challenges.

Appendix A

Appendix

A.1 Appendix Chapter 1

The following paragraph describes in depth the C and $C\#$ codes used for the MCU firmware and Graphic User Interface, respectively, in Chapter 1. The firmware code presented is a frequency counter plus the chance to transmit the data via WiFi to Graphic User Interface. The $C\#$ code is able to manage the WiFi communication and to show graphically the TX-RX pressure variation on the sensorized belt. Figure A.1 shows the GUI.

MCU FREQUENCY COUNTER AND WIFI TRANSMISSION
Objective: to count the frequency of the input signal.
General Purpose Input Output pin was configured as input pin and the MCU was set to trigger an interrupt every time a rising edge is seen on the input pin. In addition, a 16 bit internal timer has been taken into account to keep track of the sampling rate of the signal.

In terms of software, the Arduino library for the atMega32U4 has been chosen.

The Atmega timer is configured so to execute a really small piece of code which increments the value of a counter variable every 10 ms.

The signal frequency is gathered from the application by calling a public method of the Arduino library, namely FreqCountClass::read() which returns the signal frequency as uint32_t type.

The code reported below initiates the atMega32U4 timer by setting the sampling rate in ms.

```
void FreqCountClass::begin(uint16_t msec)
{
if (msec < 10) return;
gate_index = 0;
count_msw = 0;
count_prev = 0;
count_ready = 0;
counter_init();
gate_length = timer_init(msec);
uint8_t status = SREG;
```

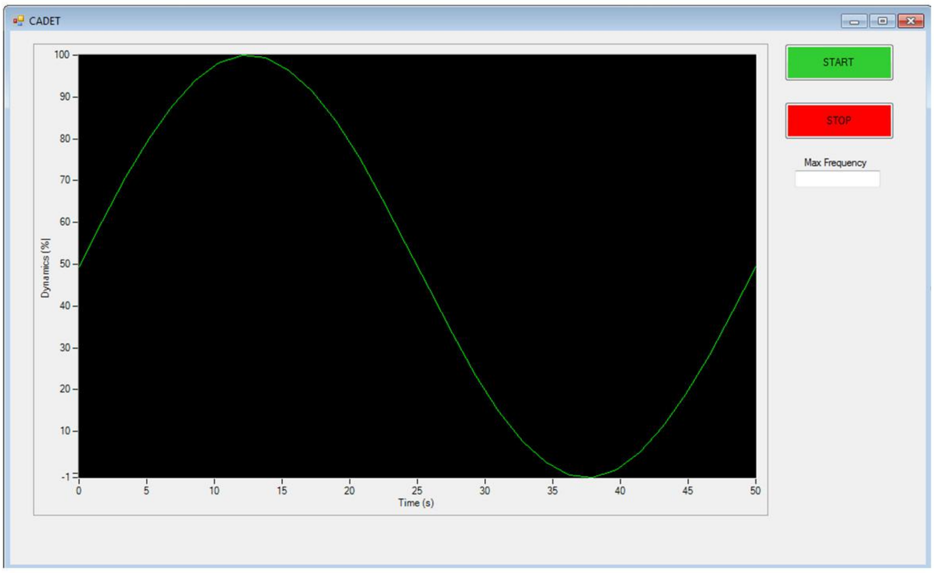

FIGURE A.1: Touch/pressure sensor GUI - CADET project.

```
cli();
timer_start();
timer_isr_latency_delay();
counter_start();
SREG = status;
}
```

The main routine of the application instead executes the following routine here bellow presented. Each second, the main routine ask for the signal frequency. When the frequency is available, the if statement returns true and the signal frequency is gathered.

```
void loop(){

  if (Skinsuit.available()) {

    if (FreqCount.available()) //Returns true when a new measurement
        //is available. Only a single
    {                          //measurement is buffered, so it must
        //be read before the next gating interval.

        unsigned long count = FreqCount.read();
        //Returns the most recent measurement, an unsigned
        //long  containing the number of rising edges
        //seen within the gating interval.

          Cadet.println(count*10);  //*10 because the GateInterval
           //is 100. In this case is faster.

    }
```

```
     delay(1);
 }

}
```

The code below present the body of the available() routine. The count_ready variable is private in the FreqCountClass class and cannot be accessed from the outside the class itself.

```
uint8_t FreqCountClass::available(void)
{
return count_ready;
}
```

Finally, the main code, where the frequency counter function is called, is below presented:

```
//---------MAIN CODE---------

//Project: Touch-pressure sensor - CADET project
//Communication: TCP protocol

//Author: Matteo Stoppa - Istituto Italiano di Tecnologia

//Description: frequency counter of the signal transmitted by UWB.
//The count value conditions the bliking speed of the LED.

//MCU: ATmega32u4 (Arudino Yun)

//IP address: 192.168.240.1


//Declaration libraries
#include <Bridge.h>      //Bridge between MCU and Lilino
#include <FreqCount.h>   //Frequency counter library
#include <YunServer.h>
#include <YunClient.h>

#define PORT 2000        //TCP port

unsigned long count;
int Tdelay;

YunServer server (PORT);
YunClient client;        //Instantiate a server enabling the
 //Yun to listen for connected clients

static boolean clientActive = false;
```

```
void setup(){

  Bridge.begin();        //Initialize Bridge
  Console.begin();       //Initialize Console
  FreqCount.begin(100);  //Begin frequency counting. GateInterval
    //is the time in milliseconds for
                         //each measurement. Using 1000 provides
                         //direct frequency output without
                         //mulitplying or dividing by a scale factor.

  server.noListenOnLocalhost();
  server.begin();        //Initialize Server
  client = server.accept();

  pinMode(4,INPUT);
  pinMode(6,INPUT);
  pinMode(8,INPUT);
  pinMode(12,INPUT);      //Pin Input

  digitalWrite(4,LOW);
  digitalWrite(6,LOW);
  digitalWrite(8,LOW);

  pinMode(13,OUTPUT);     //Pin Output

//  while (!Console){
//  }

}

void loop(){
  client.flush();            //Clear buffer TCP
  if (client.connected()){   //Connects to a specified IP address and port.
        //The return value
                             //indicates success or failure.
    if (!clientActive){
    }

    clientActive = true;
    if (client.available()){  //Returns the number of bytes available
           //for reading. In case of an input.
    }

  if (FreqCount.available())

  //Returns true when a new measurement is available.
  //Only a single measurement is buffered, so it must be read
  //before the next gating interval.

    {
      count = FreqCount.read(); //Returns the most recent measurement,
       //an unsigned long.
```

```
      count = count*20;
      // *2 --> the received signal has a half frequency of the original signal.
      // *10 --> the gateinterval is 100 and not 1000
  }
   client.println(count);
   delay(10);
   }
    else {
      if (clientActive){
      }
      clientActive = false;
      client = server.accept();
    }
}
```

TOUCH/PRESSURE SENSOR GUI - CADET PROJECT.

```
using System;
using System.Collections.Generic;
using System.Linq;
using System.Text;
using System.Net.Sockets;
using System.Threading;
using System.Net;

public class StateObject
{
    // Client socket.
    public Socket workSocket = null;
    // Size of receive buffer.
    public const int BufferSize = 256;
    // Receive buffer.
    public byte[] buffer = new byte[BufferSize];
    // Received data string.
    public StringBuilder sb = new StringBuilder();
}
public class AsynchronousClient
{
    // The port number for the remote device.
    private const int port = 2000;
    // ManualResetEvent instances signal completion.
    private static ManualResetEvent connectDone =
    new ManualResetEvent(false);
    private static ManualResetEvent sendDone =
    new ManualResetEvent(false);
    private static ManualResetEvent receiveDone =
    new ManualResetEvent(false);
    // The response from the remote device.
    private static String response = String.Empty;
    public static void StartClient()
```

```
{
    // Connect to a remote device.
    try
    {
        // Establish the remote endpoint for the socket.
        // The name of the
        // remote device is "host.contoso.com".
        //IPHostEntry ipHostInfo = Dns.GetHostEntry("192.168.43.102:255");
        //IPAddress ipAddress = ipHostInfo.AddressList[0];
        //
        IPAddress ipAddress = IPAddress.Parse("192.168.43.102");
        IPEndPoint remoteEP = new IPEndPoint(ipAddress, port);

        // Create a TCP/IP socket.
        Socket client = new Socket(AddressFamily.InterNetwork,
        SocketType.Stream, ProtocolType.Tcp);

        // Connect to the remote endpoint.
        client.BeginConnect(remoteEP,
        new AsyncCallback(ConnectCallback), client);
        connectDone.WaitOne();

        // Send test data to the remote device.
        Send(client, "This is a test<EOF>");
        sendDone.WaitOne();

        // Receive the response from the remote device.
        Receive(client);
        receiveDone.WaitOne();

        // Write the response to the console.
        // Console.WriteLine("Response received : {0}", response);
        // Release the socket.
        client.Shutdown(SocketShutdown.Both);
        client.Close();
    }
    catch (Exception e)
    {
        Console.WriteLine(e.ToString());
    }
}
private static void ConnectCallback(IAsyncResult ar)
{
    try
    {
        // Retrieve the socket from the state object.
        Socket client = (Socket)ar.AsyncState;

        // Complete the connection.
        client.EndConnect(ar);
        Console.WriteLine("Socket connected to {0}",
        client.RemoteEndPoint.ToString());
```

```
            // Signal that the connection has been made.
            connectDone.Set();
        }
        catch (Exception e)
        {
            Console.WriteLine(e.ToString());
        }
    }
    private static void Receive(Socket client)
    {
        try
        {
            // Create the state object.
            StateObject state = new StateObject();
            state.workSocket = client;

            // Begin receiving the data from the remote device.
            client.BeginReceive(state.buffer, 0, StateObject.BufferSize, 0,
            new AsyncCallback(ReceiveCallback), state);
        }
        catch (Exception e)
        {
            Console.WriteLine(e.ToString());
        }
    }
    private static void ReceiveCallback(IAsyncResult ar)
    {
        try
        {
            // Retrieve the state object and the client socket
            // from the asynchronous state object.
            StateObject state = (StateObject)ar.AsyncState;
            Socket client = state.workSocket;

            // Read data from the remote device.
            int bytesRead = client.EndReceive(ar);
            if (bytesRead > 0)
            {
                // There might be more data, so store the
                // data received so far.
                response = Encoding.ASCII.GetString(state.buffer, 0, bytesRead);

                //Console.Write("{0}", response);
                state.sb.Append(response);

                // Get the rest of the data.
                client.BeginReceive(state.buffer, 0, StateObject.BufferSize, 0,
                new AsyncCallback(ReceiveCallback), state);
            }
            else
            {
```

```
                // All the data has arrived; put it in response.
                if (state.sb.Length > 1)
                {
                    response = state.sb.ToString();
                }
                // Signal that all bytes have been received.
                receiveDone.Set();

            }

        }
        catch (Exception e)
        {
            Console.WriteLine(e.ToString());
        }
    }

    static void Send(Socket client, String data)
    {
        // Convert the string data to byte data using ASCII encoding.
        byte[] byteData = Encoding.ASCII.GetBytes(data);

        // Begin sending the data to the remote device.
        client.BeginSend(byteData, 0, byteData.Length, 0,
        new AsyncCallback(SendCallback), client);
    }
    private static void SendCallback(IAsyncResult ar)
    {
        try
        {
            // Retrieve the socket from the state object.
            Socket client = (Socket)ar.AsyncState;

            // Complete sending the data to the remote device.
            int bytesSent = client.EndSend(ar);
            Console.WriteLine("Sent {0} bytes to server.", bytesSent);
            sendDone.Set();
        }
        catch (Exception e)
        {
            Console.WriteLine(e.ToString());
        }
    }
}
```

A.2 Appendix Chapter 3

The following paragraph describes in depth the $C\#$ for the Graphic User Interface in Chapter 3. The $C\#$ code is able to manage the WiFi communication and to show graphically the TX-RX proximity. Pre-setting the distance

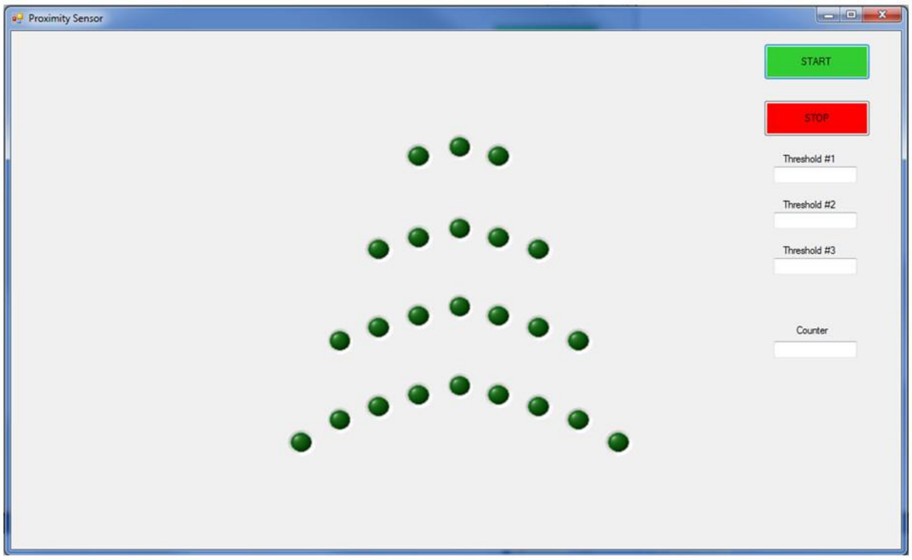

FIGURE A.2: Proximity GUI.

thresholds, the code switches on the LED stripes in relation with the TX-RX proximity. Figure A.2 shows the GUI.

The firmware code used for the MCU is the same presented in Paragraph A.1.

MCU FREQUENCY COUNTER AND WIFI TRANSMISSION

```
using System;
using System.Collections.Generic;
using System.Linq;
using System.Text;
using System.Net.Sockets;
using System.Threading;
using System.Net;

    public class StateObject
    {
        // Client socket.
        public Socket workSocket = null;
        // Size of receive buffer.
        public const int BufferSize = 256;
        // Receive buffer.
        public byte[] buffer = new byte[BufferSize];
        // Received data string.
        public StringBuilder sb = new StringBuilder();
    }
    public class AsynchronousClient
    {
        // The port number for the remote device.
        private const int port = 255;
```

```
        // ManualResetEvent instances signal completion.
        private static ManualResetEvent connectDone =
        new ManualResetEvent(false);
        private static ManualResetEvent sendDone =
        new ManualResetEvent(false);
        private static ManualResetEvent receiveDone =
        new ManualResetEvent(false);
        // The response from the remote device.
        private static String response = String.Empty;
        public static void StartClient()
        {

//----------------------------------------------
//Connect to a remote device

            try
            {
                // Establish the remote endpoint for the socket.
                // The name of the
                // remote device is "host.contoso.com".
                //IPHostEntry ipHostInfo = Dns.GetHostEntry("192.168.43.102:255");
                //IPAddress ipAddress = ipHostInfo.AddressList[0];
                //
                IPAddress ipAddress = IPAddress.Parse("192.168.43.102");
                IPEndPoint remoteEP = new IPEndPoint(ipAddress, port);

                // Create a TCP/IP socket.
                Socket client = new Socket(AddressFamily.InterNetwork,
                SocketType.Stream, ProtocolType.Tcp);

                // Connect to the remote endpoint.
                client.BeginConnect(remoteEP,
                new AsyncCallback(ConnectCallback), client);
                connectDone.WaitOne();

                // Send test data to the remote device.
                Send(client, "This is a test<EOF>");
                sendDone.WaitOne();

                // Receive the response from the remote device.
                Receive(client);
                receiveDone.WaitOne();

                // Write the response to the console.
                Console.WriteLine("Response received : {0}", response);

                // Release the socket.
                client.Shutdown(SocketShutdown.Both);
                client.Close();
            }
            catch (Exception e)
            {
```

```
            Console.WriteLine(e.ToString());
        }
    }
    private static void ConnectCallback(IAsyncResult ar)
    {
        try
        {
            // Retrieve the socket from the state object.
            Socket client = (Socket)ar.AsyncState;

            // Complete the connection.
            client.EndConnect(ar);
            Console.WriteLine("Socket connected to {0}",
            client.RemoteEndPoint.ToString());

            // Signal that the connection has been made.
            connectDone.Set();
        }
        catch (Exception e)
        {
            Console.WriteLine(e.ToString());
        }
    }
    private static void Receive(Socket client)
    {
        try
        {
            // Create the state object.
            StateObject state = new StateObject();
            state.workSocket = client;

            // Begin receiving the data from the remote device.
            client.BeginReceive(state.buffer, 0, StateObject.BufferSize, 0,
            new AsyncCallback(ReceiveCallback), state);
        }
        catch (Exception e)
        {
            Console.WriteLine(e.ToString());
        }
    }
    private static void ReceiveCallback(IAsyncResult ar)
    {
        try
        {
            // Retrieve the state object and the client socket
            // from the asynchronous state object.
            StateObject state = (StateObject)ar.AsyncState;
            Socket client = state.workSocket;

            // Read data from the remote device.
            int bytesRead = client.EndReceive(ar);
            if (bytesRead > 0)
```

```
            {
                // There might be more data, so store the data received so far.
                response = Encoding.ASCII.GetString(state.buffer, 0, bytesRead);
                Console.Write("{0}", response);
                state.sb.Append(response);

                // Get the rest of the data.
                client.BeginReceive(state.buffer, 0, StateObject.BufferSize, 0,
                new AsyncCallback(ReceiveCallback), state);
            }
            else
            {
                // All the data has arrived; put it in response.
                if (state.sb.Length > 1)
                {
                    response = state.sb.ToString();
                }
                // Signal that all bytes have been received.
                receiveDone.Set();

            }

        }
        catch (Exception e)
        {
            Console.WriteLine(e.ToString());
        }
    }


    public static String getCurrentData()
    {
        return response;
    }


    static void Send(Socket client, String data)
    {
        // Convert the string data to byte data using ASCII encoding.
        byte[] byteData = Encoding.ASCII.GetBytes(data);

        // Begin sending the data to the remote device.
        client.BeginSend(byteData, 0, byteData.Length, 0,
        new AsyncCallback(SendCallback), client);
    }
    private static void SendCallback(IAsyncResult ar)
    {
        try
        {
            // Retrieve the socket from the state object.
            Socket client = (Socket)ar.AsyncState;
```

```
                // Complete sending the data to the remote device.
                int bytesSent = client.EndSend(ar);
                Console.WriteLine("Sent {0} bytes to server.", bytesSent);
                sendDone.Set();
            }
            catch (Exception e)
            {
                Console.WriteLine(e.ToString());
            }
        }
    }
```

A.3 Appendix Chapter 5

The following paragraph describes in depth two firmware codes used with the ATmega32u4 for the load and stretch monitoring system respectively.

The first firmware code presented is able to read an ADC the voltage variation, due to the FSR value into the voltage divider, and to convert into a force.

Then, the firmware for the stretch monitoring system consists in a frequency counter, explained in Paragraph A.1, and a code for the Bluetooth communication.

LOAD MONITORING SYSTEM - $\Delta R - to - \Delta F$

```
//Project: Load Monitorin System with FSR
//Communication: Serial port
//Author: Matteo Stoppa - Istituto Italiano di Tecnologia

//Description: FSR measurements and R-to-F convertion

//MCU: ATmega32u4

#define NUMSAMPLES 50

int fsrPin1 = 0;     // the FSR and 10K pulldown are connected to a0
int fsrReading1;     // the analog reading from the FSR 1 resistor divider
int fsrVoltage;      // the analog reading converted to voltage 1
float fsrResistance; // The voltage converted to resistance 1,
 //can be very big so make "long"
float fsrConductance;
float fsrForce;      // Finally, the resistance converted to force 1

float average;
float samples1[NUMSAMPLES];

uint8_t i;

int LEDpin = 13;
```

```
int LEDbrightness;

void setup(void) {
  Serial.begin(9600);   //We'll send debugging information
   //via the Serial monitor.
}



void loop(void) {
  fsrReading = analogRead(fsrPin);
  //Serial.print("Sensor  = ");
  //Serial.println(fsrReading);

  // analog voltage reading ranges from about 0 to 1023
  // which maps to 0V to 5V (= 5000mV)

  fsrVoltage1 = map(fsrReading, 0, 1023, 0, 5000);
  //Serial.print("Sensor 1 in mV = ");
  //Serial.println(fsrVoltage1);

  LEDbrightness = map(fsrReading, 0, 1023, 0, 255);
  // LED gets brighter the harder you press
  analogWrite(LEDpin, LEDbrightness);

  if (fsrVoltage == 0 && fsrVoltage2 == 0) {
    Serial.println("No pressure");
  } else {

  // fsrVoltage is in millivolts so 5V
    fsrResistance = 5000 - fsrVoltage;

    // 10K resistor
    fsrResistance *= 10000;
    fsrResistance /= fsrVoltage;
    fsrResistance /= 1000;

    //Serial.print("FSR resistance in Kohms = ");
    //Serial.println(fsrResistance1,5);

    //Serial.println(fsrResistance);
    fsrConductance = 1 / (fsrResistance);
    //Serial.print("Conductance in Siemens: ");
    //Serial.println(fsrConductance1,5);
//

    //AVERAGE//
    // take N samples in a row, with a slight delay
   average = 0;
   for (i=0; i< NUMSAMPLES; i++) {
    samples[i] = fsrResistance;
```

```
    average += samples[i];  // average all the samples out

   delay(1);
  }
  average /= NUMSAMPLES;


  average = 0;
  for (i=0; i< NUMSAMPLES; i++) {
     samples[i] = fsrReading;
     delay(1);
  }
  for (i=0; i< NUMSAMPLES; i++) {
    average += samples[i];
  }

  average /= NUMSAMPLES;
  Serial.println(average);

    //Serial.print("FSR resistance in Kohms = ");
    //Serial.println(average,5);

    // Use the FSR guide graphs to approximate the force (see datasheet)
          if (fsrConductance <= 0.07) {
            average = fsrConductance * 555,556;
            //Serial.print("Force in grams Sensor1: ");
            Serial.println(average1/1000*9.8);

          } else if (fsrConductance > 0.07 && fsrConductance <= 0.27) {
                   average1 = fsrConductance1 * 833.33 - 16.667;
                   //Serial.print("Force in grams Sensor1: ");
                   Serial.println(average1/1000*9.8);

                  } else if (fsrConductance > 0.27 && fsrConductance <= 0.8) {
                           average1 = fsrConductance1 * 1515.152 - 208.33;
                           //Serial.print("Force in grams Sensor1: ");
                           Serial.println(average1/1000*9.8);

                         } else if (fsrConductance > 0.8 && fsrConductance <= 1.8) {
                                   average1 = fsrConductance1 * 1886.792 - 516.377;
                                   //Serial.print("Force in grams Sensor1: ");
                                   Serial.println(average1/1000*9.8);

                                 } else {
                                 average1 = fsrConductance * 2941.176 - 2409.6176;
                                 //Serial.print("Force in grams Sensor1: ");
                                 Serial.println(average1/1000*9.8);
                                 }
//

  delay(10);
```

```
}
```

LOAD MONITORING SYSTEM - BLUETOOTH COMMUNICATION

Following the source code able to stream the data via Bluetooth.

```
//Project: Skinsuit BT
//Communication: Bluetooth
//Author: Matteo Stoppa - Istituto Italiano di Tecnologia

//Description: frequency counter of Schmitt Trigger Oscillator signal.
//BT transmission to the GUI

//MCU: ATmega32u4

//Declaration libraries
#include <FreqCount.h>        //Frequency counter library
#include <SoftwareSerial.h>   //Import the serial library

// D11   >>>  Rx
// D10   >>>  Tx

SoftwareSerial Skinsuit(10, 11); //RX, TX


void setup(){
  Skinsuit.begin(9600);
  FreqCount.begin(1000); //Begin frequency counting.

  // GateInterval is the time in milliseconds for each
  // measurement. Using 1000 provides direct frequency
  // output without mulitplying or dividing by a scale factor.

  pinMode(4,INPUT);
  pinMode(6,INPUT);
  pinMode(8,INPUT);
  pinMode(12,INPUT);      //Pin Input

  digitalWrite(4,LOW);
  digitalWrite(6,LOW);
  digitalWrite(8,LOW);

  Serial.begin(9600);
}

void loop(){

  if (Skinsuit.available()) {

    if (FreqCount.available())
    // Returns true when a new measurement is available.
    // Only a single measurement is buffered, so it
```

```
    // must be read before the next gating interval.
    {


        unsigned long count = FreqCount.read();

       // Returns the most recent measurement, an unsigned long
       // containing the number of rising edges seen within the
       //gating interval.

         Skinsuit.println(count*1);
       //*10 because the GateInterval is 100. In this case is faster.

    }
      delay(1);
 }

}
```

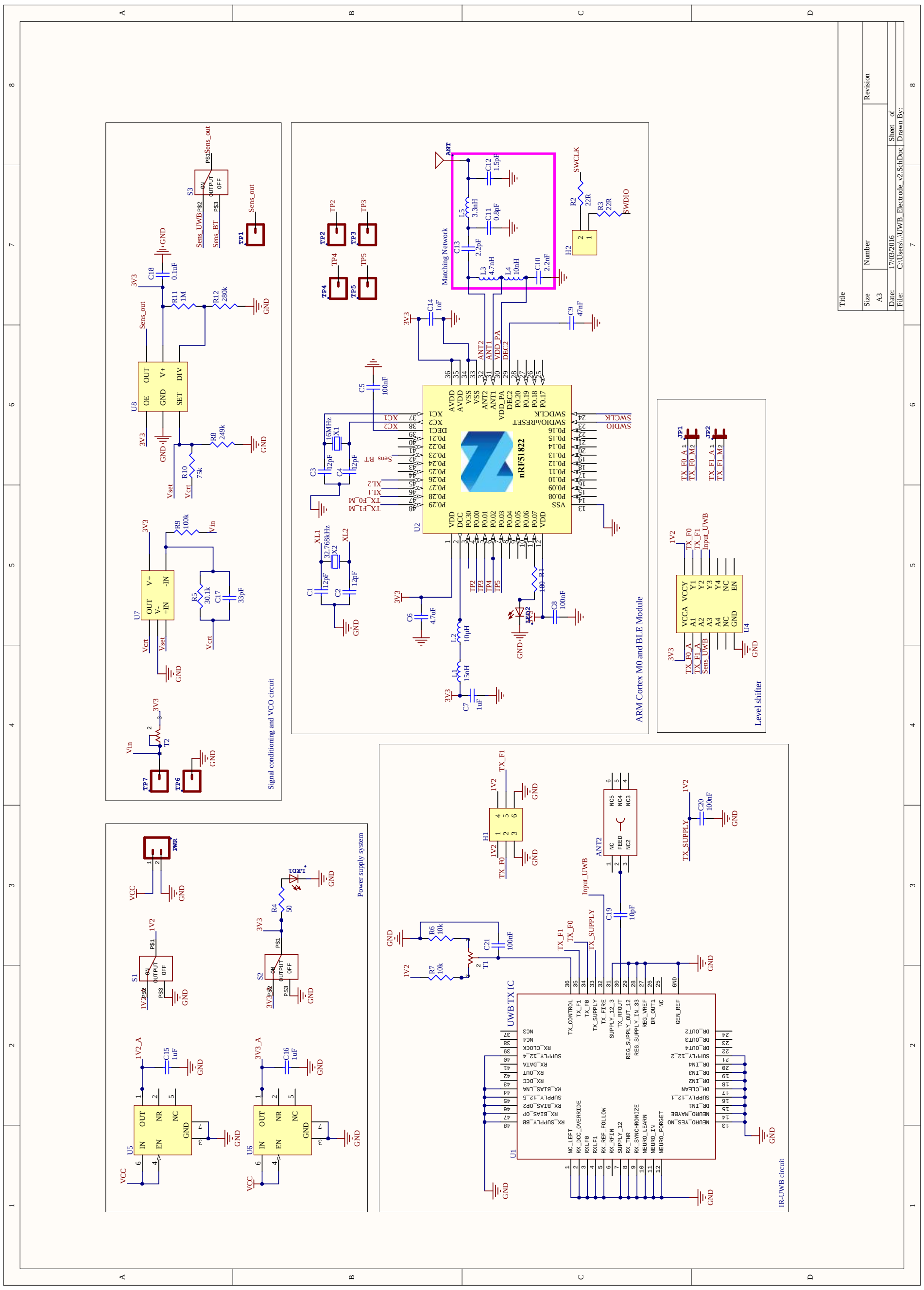

FIGURE A.3: SEM system schematic.

Bibliography

Abdul Razak, Abdul Hadi et al. (2012). “Foot plantar pressure measurement system: A review”. In: *Sensors* 12.7, pp. 9884–9912.

Agache, PG et al. (1980). “Mechanical properties and Young’s modulus of human skin in vivo”. In: *Archives of dermatological research* 269.3, pp. 221–232.

ALmassri, Ahmed M et al. (2014). “Real-time control for robotic hand application based on pressure sensor measurement”. In: *IEEE International Symposium on Robotics and Manufacturing Automation*, pp. 15–16.

Almassri, Ahmed M et al. (2015). “Pressure sensor: state of the art, design, and application for robotic hand”. In: *Journal of Sensors* 2015.

Angelopoulos, Constantinos Marios, Christofoulos Mouskos, and Sotiris Nikoletseas (2011). “Social signal processing: Detecting human interactions using wireless sensor networks”. In: *Proceedings of the 9th ACM international symposium on Mobility management and wireless access*. ACM, pp. 171–174.

Annis, JF (1978). “Anthropometric sourcebook (Vol. 1: Anthropometry for designers; NASA Reference Publication 1024, table 15)”. In: *Houston, TX: National Aeronautics and Space Administration*.

Arduino Board Yun. (accessed October 01, 2015). URL: `https://www.arduino.cc/en/Main/ArduinoBoardYun`.

Arduino Board Yun. (accessed July 01, 2015). URL: `https://www.sparkfun.com/datasheets/Sensors/Pressure/fsrguide.pdf`.

Ashley, Steven (2003). “Artificial muscles”. In: *Scientific American* 289.4, pp. 52–59.

Attias, Julia et al. (2013). “THE EFFECT OF THE GRAVITY LOADING COUNTERMEASURE SKIN SUIT(GLCS) UPON AEROBIC EXERCISE PERFORMANCE”. In: *Aviation, Space, and Environmental Medicine* 84.4.

Baqai, Farnaz P et al. (2009). “Effects of spaceflight on innate immune function and antioxidant gene expression”. In: *Journal of applied physiology* 106.6, pp. 1935–1942.

Bar-Cohen, Yoseph (2002). “Electroactive polymers: current capabilities and challenges”. In: *SPIE’s 9th Annual International Symposium on Smart Structures and Materials*. International Society for Optics and Photonics, pp. 1–7.

Bar-Cohen, Yoseph (2004). "EAP as artificial muscles: progress and challenges". In: *Smart Structures and Materials*. International Society for Optics and Photonics, pp. 10–16.

Barratt, Michael R and Sam Lee Pool (2008). *Principles of clinical medicine for space flight*. Springer Science & Business Media.

Barton, Richard J and Divya Rao (2008). "Performance capabilities of long-range UWB-IR TDOA localization systems". In: *EURASIP Journal on Advances in Signal Processing* 2008, p. 81.

Baughman, RH (1996). "Conducting polymer artificial muscles". In: *Synthetic metals* 78.3, pp. 339–353.

Belkin TuneCast-II. (accessed June 7 , 2015). URL: `http://www.belkin.com/support/785dl/f8v3080.pdf`.

Bikle, Daniel D, Takeshi Sakata, and Bernard P Halloran (2007). "The impact of skeletal unloading on bone formation". In: *Gravitational and Space Research* 16.2.

Binkley, Philip F (2003). "Predicting the potential of wearable technology". In: *Engineering in Medicine and Biology Magazine, IEEE* 22.3, pp. 23–27.

BIOTEX. (accessed November 03, 2014). URL: `http://www.biotex-eu.com/`.

Blaber, Elizabeth, Helder Marçal, and Brendan P Burns (2010). "Bioastronautics: the influence of microgravity on astronaut health". In: *Astrobiology* 10.5, pp. 463–473.

Bluetooth®. (accessed June 10 , 2015). URL: `https://www.bluetooth.org/en-us/`.

Bonato, Paolo (2005). "Advances in wearable technology and applications in physical medicine and rehabilitation". In: *Journal of NeuroEngineering and Rehabilitation* 2.1, p. 2.

Brady, Sarah et al. (2007). "Body sensor network based on soft polymer sensors and wireless communications". In: *Journal of Communications* 2.5, pp. 1–6.

Brochu, Paul and Qibing Pei (2010). "Advances in dielectric elastomers for actuators and artificial muscles". In: *Macromolecular rapid communications* 31.1, pp. 10–36.

Bungo, Michael W et al. (1987). "Results of the life sciences DSOs conducted aboard the space shuttle 1981-1986". In:

Cadogan, David P (2015). "The Past and Future Space Suit". In: *American Scientist* 103.5, p. 338.

Cannata, Giorgio and Marco Maggiali (2005). "An embedded tactile and force sensor for robotic manipulation and grasping". In: *Humanoid Robots, 2005 5th IEEE-RAS International Conference on*. IEEE, pp. 80–85.

Cannata, Giorgio et al. (2008). “An embedded artificial skin for humanoid robots”. In: *Multisensor Fusion and Integration for Intelligent Systems, 2008. MFI 2008. IEEE International Conference on*. IEEE, pp. 434–438.

Cardinali, Roberta et al. (2006). “UWB ranging accuracy in high-and low-data-rate applications”. In: *Microwave Theory and Techniques, IEEE Transactions on* 54.4, pp. 1865–1875.

Carosio, Stefano and Alessandra Monero (2004). “Smart and hybrid materials: perspectives for their use in textile structures for better health care”. In: *Stud Health Technol Inform* 108, pp. 335–43.

Carpi, Federico and D De Rossi (2005). “Improvement of electromechanical actuating performances of a silicone dielectric elastomer by dispersion of titanium dioxide powder”. In: *Dielectrics and Electrical Insulation, IEEE Transactions on* 12.4, pp. 835–843.

Carpi, Federico et al. (2011a). *Dielectric elastomers as electromechanical transducers: Fundamentals, materials, devices, models and applications of an emerging electroactive polymer technology*. Elsevier.

Carpi, Federico et al. (2011b). “Electroactive polymer actuators as artificial muscles: are they ready for bioinspired applications?” In: *Bioinspiration & biomimetics* 6.4, p. 045006.

Cattuto, Ciro et al. (2010). “Dynamics of person-to-person interactions from distributed RFID sensor networks”. In: *PloS one* 5.7, e11596.

Cavanagh, Peter R, Angelo A Licata, and Andrea J Rice (2007). “Exercise and pharmacological countermeasures for bone loss during longduration space flight”. In: *Gravitational and Space Research* 18.2.

Chakraborti, P et al. (2012). “A compact dielectric elastomer tubular actuator for refreshable Braille displays”. In: *Sensors and Actuators A: Physical* 179, pp. 151–157.

Choi, Seok H et al. (2004). “A new ultra-wideband antenna for UWB applications”. In: *Microwave and optical technology letters* 40.5, pp. 399–401.

Chong, Chia-Chin, Fujio Watanabe, and Hiroshi Inamura (2006). “Potential of UWB technology for the next generation wireless communications”. In: *Spread Spectrum Techniques and Applications, 2006 IEEE Ninth International Symposium on*. IEEE, pp. 422–429.

Christopher, JH Reed (2005). *An Introduction to Ultra Wideband Communication System*.

Conductive rubber cord. (accessed June 03 , 2015). URL: `https://www.adafruit.com/products/519`.

CONTEXT. (accessed November 03, 2014). URL: `http://www.context-project.org/`.

Convertino, VICTOR A (1996). “Exercise as a countermeasure for physiological adaptation to prolonged spaceflight.” In: *Medicine and science in sports and exercise* 28.8, pp. 999–1014.

Convertino, Victor A (2009). “Status of cardiovascular issues related to space flight: implications for future research directions”. In: *Respiratory physiology & neurobiology* 169, S34–S37.

Convidein ECG electrode. (accessed June 03 , 2015). URL: `http://www.covidien.com/imageServer.aspx/doc242691.pdf?contentID=31382&contenttype=application/pdf`.

Cooke, William H and Victor A Convertino (2007). “Sympathetic nervous system and spaceflight”. In: *Acta Astronautica* 60.4, pp. 223–233.

Cramer, Gregory D and Susan A Darby (2013). *Clinical anatomy of the spine, spinal cord, and ANS*. Elsevier Health Sciences.

Crepaldi, Marco et al. (2012). “A very low-complexity 0.3–4.4 GHz 0.004 mm all-digital ultra-wide-band pulsed transmitter for energy detection receivers”. In: *Circuits and Systems I: Regular Papers, IEEE Transactions on* 59.10, pp. 2443–2455.

Crepaldi, Marco et al. (2014). “A non-coherent IR-UWB receiver for high sensitivity short distance estimation”. In: *Circuits and Systems (ISCAS), 2014 IEEE International Symposium on*. IEEE, pp. 1905–1908.

Dai, Ching-Liang et al. (2009). “Capacitive micro pressure sensor integrated with a ring oscillator circuit on chip”. In: *Sensors* 9.12, pp. 10158–10170.

De Rossi, D, A Della Santa, and A Mazzoldi (1999). “Dressware: wearable hardware”. In: *Materials Science and Engineering: C* 7.1, pp. 31–35.

De Rossi, D et al. (2002). “5.1: Electroactive Fabrics for Distributed, Conformable and Interactive Systems”. In:

De Rossi, Danilo et al. (2003). *Active dressware: wearable kinesthetic systems*. Springer.

Debuse, Dorothée et al. (2013). “Low impact weight-bearing exercise in an upright posture increases the activation of two key local muscles of the lumbo-pelvic region”. In: *Physiotherapy theory and practice* 29.1, pp. 51–60.

DecaWave DW1000. (accessed October 01, 2015). URL: `http://www.decawave.com/products/evk1000-evaluation-kit`.

Denis, B, J Keignart, and N Daniele (2003). “Impact of NLOS propagation upon ranging precision in UWB systems”. In: *Ultra Wideband Systems and Technologies, 2003 IEEE Conference on*. IEEE, pp. 379–383.

DEPHOTEX. (accessed November 03, 2014). URL: `http://www.dephotex.com/`.

Eagle, Nathan and Alex Pentland (2006). “Reality mining: sensing complex social systems”. In: *Personal and ubiquitous computing* 10.4, pp. 255–268.

Eagle, Nathan, Alex Sandy Pentland, and David Lazer (2009). “Inferring friendship network structure by using mobile phone data”. In: *Proceedings of the national academy of sciences* 106.36, pp. 15274–15278.

Eberhardt, Robert T and Joseph D Raffetto (2014). “Chronic venous insufficiency”. In: *Circulation* 130.4, pp. 333–346.

Eckberg, DL (2003). “Bursting into space: alterations of sympathetic control by space travel”. In: *Acta physiologica scandinavica* 177.3, pp. 299–311.

Eckberg, Dwain L et al. (2010). “Human vagal baroreflex mechanisms in space”. In: *The Journal of physiology* 588.7, pp. 1129–1138.

Ewert, Michael K and Frank F Jeng (2015). “Will Astronauts Wash Clothes on the Way to Mars?” In: 45th International Conference on Environmental Systems.

Fitts, RH et al. (2010). “Prolonged space flight-induced alterations in the structure and function of human skeletal muscle fibres”. In: *The Journal of physiology* 588.18, pp. 3567–3592.

Foerster, Jeffrey R (2001). “The effects of multipath interference on the performance of UWB systems in an indoor wireless channel”. In: *Vehicular Technology Conference, 2001. VTC 2001 Spring. IEEE VTS 53rd*. Vol. 2. IEEE, pp. 1176–1180.

Forys, Andrzej et al. (2013). “WRENMining: large-scale data collection for human contact network research”. In: *Proceedings of First International Workshop on Sensing and Big Data Mining*. ACM, pp. 1–6.

Fregly, Christopher D et al. (2013). “Dynamic Simulation of Muscle Loading During ARED Squat Exercise on the International Space Station”. In: *ASME 2013 Summer Bioengineering Conference*. American Society of Mechanical Engineers, pp. 11–22.

Garnier, Francis et al. (1994). “All-polymer field-effect transistor realized by printing techniques”. In: *Science* 265.5179, pp. 1684–1686.

Ge, Lijia, Guangrong Yue, and Sofiene Affes (2002). “On the BER performance of pulse-position-modulation UWB radio in multipath channels”. In: *Ultra Wideband Systems and Technologies, 2002. Digest of Papers. 2002 IEEE Conference on*. IEEE, pp. 231–234.

Gefen, Amit (2007). “Pressure-sensing devices for assessment of soft tissue loading under bony prominences: technological concepts and clinical utilization.” In: *Wounds: a compendium of clinical research and practice* 19.12, pp. 350–362.

Gezici, Sinan et al. (2005). “Performance evaluation of impulse radio UWB systems with pulse-based polarity randomization”. In: *Signal Processing, IEEE Transactions on* 53.7, pp. 2537–2549.

Ghovanloo, Maysam and Khalil Najafi (2002). “A BiCMOS wireless stimulator chip for micromachined stimulating microprobes”. In: *Proceedings of the Second Joint EMBS/BMES Conference*, pp. 2113–2114.

Gibbs, Peter T and HHarry Asada (2005). “Wearable conductive fiber sensors for multi-axis human joint angle measurements”. In: *Journal of NeuroEngineering and Rehabilitation* 2.1, p. 1.

Gigl, Thomas et al. (2007). “Analysis of a UWB indoor positioning system based on received signal strength”. In: *Positioning, Navigation and Communication, 2007. WPNC'07. 4th Workshop on*. IEEE, pp. 97–101.

Golder, Scott A, Dennis M Wilkinson, and Bernardo A Huberman (2007). “Rhythms of social interaction: Messaging within a massive online network”. In: *Communities and technologies 2007*. Springer, pp. 41–66.

Gopalakrishnan, Raghavan et al. (2010). “Muscle volume, strength, endurance, and exercise loads during 6-month missions in space”. In: *Aviation, space, and environmental medicine* 81.2, pp. 91–104.

Grillet, Augustin et al. (2008). “Optical fiber sensors embedded into medical textiles for healthcare monitoring”. In: *Sensors Journal, IEEE* 8.7, pp. 1215–1222.

Grim, M. and D.E. Stroud (2011). *Bicycle helmet adjustment mechanism*. US Patent 8,015,625. URL: `https://www.google.it/patents/US8015625`.

Habibi, M et al. (1995). “A surface micromachined capacitive absolute pressure sensor array on a glass substrate”. In: *Sensors and Actuators A: Physical* 46.1, pp. 125–128.

Hannah, Richard L and Stuart E Reed (1992). *Strain gage users' handbook*. Springer Science & Business Media.

Hanson, AM et al. (2014). “Evaluation of the XSENS Force Shoe on ISS”. In:

Hargens, Alan R, Roshmi Bhattacharya, and Suzanne M Schneider (2013). “Space physiology VI: exercise, artificial gravity, and countermeasure development for prolonged space flight”. In: *European journal of applied physiology* 113.9, pp. 2183–2192.

Harsányi, Gábor (2000). “Polymer films in sensor applications: a review of present uses and future possibilities”. In: *Sensor Review* 20.2, pp. 98–105.

Hermann, David et al. (2004). “Low-power implementation of the Bluetooth subband audio codec”. In: *Acoustics, Speech, and Signal Processing, 2004. Proceedings.(ICASSP'04). IEEE International Conference on*. Vol. 5. IEEE, pp. V–365.

Hoffmann, T, B Eilebrecht, and S Leonhardt (2011). “Respiratory monitoring system on the basis of capacitive textile force sensors”. In: *Sensors Journal, IEEE* 11.5, pp. 1112–1119.

Huang, Ching-Tang, Chien-Fa Tang, and Chien-Lung Shen (2006). “A wearable textile for monitoring respiration, using a yarn-based sensor”. In: *Wearable Computers, 2006 10th IEEE International Symposium on*. IEEE, pp. 141–142.

Huang, William et al. (2014). “Opo: A wearable sensor for capturing high-fidelity face-to-face interactions”. In: *Proceedings of the 12th ACM Conference on Embedded Network Sensor Systems*. ACM, pp. 61–75.

Hui, Pan et al. (2005). “Pocket switched networks and human mobility in conference environments”. In: *Proceedings of the 2005 ACM SIGCOMM workshop on Delay-tolerant networking*. ACM, pp. 244–251.

Hui, Zhang et al. (2006). “Pressure sensing fabric”. In: *MRS Proceedings*. Vol. 920. Cambridge Univ Press, 0920–S05.

Isella, Lorenzo et al. (2011). “Close encounters in a pediatric ward: measuring face-to-face proximity and mixing patterns with wearable sensors”. In: *PloS one* 6.2, e17144.

Johnston, Richard S and Lawrence F Dietlein (1977). “Biomedical results from Skylab. NASA SP-377”. In: *Biomedical Results from Skylab*. Vol. 377.

Johnston, Smith L et al. (2010). “Risk of herniated nucleus pulposus among US astronauts”. In: *Aviation, space, and environmental medicine* 81.6, pp. 566–574.

Jovanov, Emil et al. (2005). “A wireless body area network of intelligent motion sensors for computer assisted physical rehabilitation”. In: *Journal of NeuroEngineering and rehabilitation* 2.1, p. 6.

Jovanov, Emil et al. (2006). “A WBAN system for ambulatory monitoring of physical activity and health status: applications and challenges”. In: *Engineering in Medicine and Biology Society, 2005. IEEE-EMBS 2005. 27th Annual International Conference of the*. IEEE, pp. 3810–3813.

Kendrick, Dustin P and Dava J Newman (2014). “Modeling the Gravity Loading Countermeaure Skinsuit”. In: 44th International Conference on Environmental Systems.

Kerstman, Eric L et al. (2012). “Space adaptation back pain: a retrospective study”. In: *Aviation, space, and environmental medicine* 83.1, pp. 2–7.

Khan, Azam et al. (2013). “Harvesting piezoelectric potential from zinc oxide nanoflowers grown on textile fabric substrate”. In: *physica status solidi (RRL)-Rapid Research Letters* 7.11, pp. 980–984.

Kistler. (accessed June 03 , 2015). URL: `http://www.kistler.com/gb/en/products/components/force-sensors/`.

Kozlovskaya, Inessa B et al. (2015). “Russian Countermeasure Systems for Adverse Effects of Microgravity on Long-Duration ISS Flights”. In: *Aerospace medicine and human performance* 86.12, A24–A31.

Lackner, James R and Paul DiZio (2006). “Space motion sickness”. In: *Experimental Brain Research* 175.3, pp. 377–399.

Lang, Thomas et al. (2004). “Cortical and trabecular bone mineral loss from the spine and hip in long-duration spaceflight”. In: *Journal of bone and mineral research* 19.6, pp. 1006–1012.

Lansford, Jim and David Shoemaker (2007). “Technology tradeoffs for a worldwide UWB transceiver”. In: *Ultra-Wideband, 2007. ICUWB 2007. IEEE International Conference on*. IEEE, pp. 259–263.

Latré, Benoît et al. (2011). “A survey on wireless body area networks”. In: *Wireless Networks* 17.1, pp. 1–18.

Laukhina, E et al. (2014). “Conductive fabric responding to extremely small temperature changes”. In: *Procedia Engineering* 87, pp. 144–147.

Lehmann, W et al. (2001). “Giant lateral electrostriction in ferroelectric liquid-crystalline elastomers”. In: *Nature* 410.6827, pp. 447–450.

Liem, Karel F et al. (2001). *Functional anatomy of the vertebrates: an evolutionary perspective*. 596 FUN. Harcourt College Publishers New York.

Liu, Huaping (2003). “Error performance of a pulse amplitude and position modulated ultra-wideband system over lognormal fading channels”. In: *Communications Letters, IEEE* 7.11, pp. 531–533.

Liu, Shu, Yingxin Jiang, and Aaron Striegel (2014). “Face-to-Face Proximity EstimationUsing Bluetooth On Smartphones”. In: *Mobile Computing, IEEE Transactions on* 13.4, pp. 811–823.

Liu, Yiming et al. (2005). “Investigation of electrostrictive polymers for energy harvesting”. In: *Ultrasonics, Ferroelectrics, and Frequency Control, IEEE Transactions on* 52.12, pp. 2411–2417.

Lorwongtragool, Panida et al. (2014). “A novel wearable electronic nose for healthcare based on flexible printed chemical sensor array”. In: *Sensors* 14.10, pp. 19700–19712.

Lumelsky, Vladimir, Michael S Shur, and Sigurd Wagner (2000). *Sensitive skin*. Vol. 18. World Scientific.

Majidi, Carmel (2014). “Soft robotics: a perspective—current trends and prospects for the future”. In: *Soft Robotics* 1.1, pp. 5–11.

Mandal, MK and BC Sarkar (2010). “Ring oscillators: Characteristics and applications”. In: *Indian journal of pure & applied physics* 48, pp. 136–145.

Mazzoldi, A et al. (1998). “Actuative properties of polyaniline fibers under electrochemical stimulation”. In: *Materials Science and Engineering: C* 6.1, pp. 65–72.

Measurement Specialties. (Accessed July 10 , 2015). URL: `http://www.meas-spec.com/`.

Melnykowycz, Mark et al. (2014). “Comparison of Piezoresistive Monofilament Polymer Sensors”. In: *Sensors* 14.1, pp. 1278–1294.

MICROFLEX. (accessed November 03, 2014). URL: `http://microflex.ecs.soton.ac.uk`.

Mirfakhrai, Tissaphern, John DW Madden, and Ray H Baughman (2007). “Polymer artificial muscles”. In: *Materials today* 10.4, pp. 30–38.

Monica, Stefania and Giorgio Ferrari (2014). “An experimental model for UWB distance measurements and its application to localization problems”. In: *Ultra-WideBand (ICUWB), 2014 IEEE International Conference on*. IEEE, pp. 297–302.

Monkman, Gareth et al. (2005). "Universal frequency-to-digital converter for quasi-digital and smart sensors: specifications and applications". In: *Sensor Review* 25.2, pp. 92–99.

Moon, Hangil et al. (2015). "Low latency audio coder design for bluetooth and bluetooth low energy". In: *Consumer Electronics (ICCE), 2015 IEEE International Conference on*. IEEE, pp. 138–141.

MyHeart. (accessed November 03, 2014). URL: `projects.com/euprojects/myheart/`.

Najafi, Bijan, David G Armstrong, and Jane Mohler (2013). "Novel wearable technology for assessing spontaneous daily physical activity and risk of falling in older adults with diabetes". In: *Journal of diabetes science and technology* 7.5, pp. 1147–1160.

Nikookar, Homayoun and Ramjee Prasad (2008). *Introduction to ultra wideband for wireless communications*. Springer Science & Business Media.

Norimatsu, Takayasu et al. (2007). "A UWB-IR transmitter with digitally controlled pulse generator". In: *Solid-State Circuits, IEEE Journal of* 42.6, pp. 1300–1309.

Novel Quality in Measurement. (accessed July 10 , 2015). URL: `http://www.novel.de/`.

OFSETH. (accessed November 03, 2014). URL: `http://www.ofseth.org/`.

Oliva-Avilés, AI, F Avilés, and V Sosa (2011). "Electrical and piezoresistive properties of multi-walled carbon nanotube/polymer composite films aligned by an electric field". In: *Carbon* 49.9, pp. 2989–2997.

Onwubolu, Godfrey (2005). *Mechatronics: principles and applications*. Butterworth-Heinemann.

Organization, World Health et al. (2002). *Guidelines on prevention and control of hospital associated infections*. The Organization.

Osada, Yoshihito and Danilo E De Rossi (2013). *Polymer sensors and actuators*. Springer Science & Business Media.

Otis, Brian P and Jan M Rabaey (2003). "A 300-μW 1.9-GHz CMOS oscillator utilizing micromachined resonators". In: *Solid-State Circuits, IEEE Journal of* 38.7, pp. 1271–1274.

Padgett, Jay E (2003). "The power spectral density of a UWB signal with Pulse Repetition Frequency (PRF) modulation". In: *Ultra Wideband Systems and Technologies, 2003 IEEE Conference on*. IEEE, pp. 15–20.

Page, Tom (2015). "Barriers to the Adoption of Wearable Technology". In: *i-Manager's Journal on Information Technology* 4.3, p. 1.

Paradiso, Rita et al. (2005). "WEALTHY-a wearable healthcare system: new frontier on e-textile". In: *Journal of Telecommunications and Information Technology*, pp. 105–113.

Park, Sungmee and Sundaresan Jayaraman (2003). “Enhancing the quality of life through wearable technology”. In: *Engineering in Medicine and Biology Magazine, IEEE* 22.3, pp. 41–48.

Paromed. (Accessed July 10 , 2015). URL: `http://www.paromed.de/`.

Patel, Shyamal et al. (2012). “A review of wearable sensors and systems with application in rehabilitation”. In: *Journal of neuroengineering and rehabilitation* 9.1, p. 1.

PCB Piezotronics, Inc. (Accessed July 10 , 2015). URL: `http://www.pcb.com/`.

Pelrine, Ron et al. (2000). “High-speed electrically actuated elastomers with strain greater than 100%”. In: *Science* 287.5454, pp. 836–839.

Pelrine, Ronald et al. (2008). “Variable stiffness mode: devices and applications”. In: *Dielectric elastomers as electromechanical transducers*, pp. 141–145.

Pelrine, Ronald E, Roy D Kornbluh, and Jose P Joseph (1998). “Electrostriction of polymer dielectrics with compliant electrodes as a means of actuation”. In: *Sensors and Actuators A: Physical* 64.1, pp. 77–85.

Phan, Tuan-Anh et al. (2007). “A 18-pJ/pulse OOK CMOS transmitter for multiband UWB impulse radio”. In: *Microwave and Wireless Components Letters, IEEE* 17.9, pp. 688–690.

PISCATAWAY, NJ (1996). “Wireless LAN medium access control (MAC) and physical layer (PHY) specifications”. In: *IEEE P802. 11 D3*.

PLACE-it. (accessed November 03, 2014). URL: `http://www.place-it-project.eu/`.

PLUS Location System. (accessed October 01, 2015). URL: `http://www.timedomain.com/plus.php/`.

Pomalaza-Ráez, Carlos and Attaphongse Taparugssanagorn (2012). *The UWB Channel in Medical Wireless Body Area Networks (WBANs)*. INTECH Open Access Publisher.

Produino XL-DM01 2.4 GHz Bluetooth. (accessed June 7 , 2015). URL: `http://www.dx.com/it/p/produino-xl-dm01-2-4g-wireless-digital-audio-transceiver-module-army-green`.

PROETEX. (accessed November 03, 2014). URL: `http://www.proetex.org/`.

PulsON 410®. (accessed October 01, 2015). URL: `http://www.timedomain.com/datasheets/TD_DS_P410_RCM_FA.pdf`.

Punning, Andres, Maarja Kruusmaa, and Alvo Aabloo (2007). “Surface resistance experiments with IPMC sensors and actuators”. In: *Sensors and Actuators A: Physical* 133.1, pp. 200–209.

Raskovic, Dejan, Thomas Martin, and Emil Jovanov (2004). “Medical monitoring applications for wearable computing”. In: *The computer journal* 47.4, pp. 495–504.

Reschke, Millard F et al. (2009). “Postural reflexes, balance control, and functional mobility with long-duration head-down bed rest”. In: *Aviation, space, and environmental medicine* 80.Supplement 1, A45–A54.

Robson, Karen et al. (2016). “Wearable Technology: Trends and Opportunities for Organizations”. In: *Celebrating America's Pastimes: Baseball, Hot Dogs, Apple Pie and Marketing?* Springer, pp. 801–801.

ROHM BH1417 Stereo PLL FM Transmitter. (accessed June 15 , 2015). URL: `http://www.alldatasheet.com/view.jsp?Searchword=BH1417`.

Rosset, Samuel and Herbert R Shea (2013). “Flexible and stretchable electrodes for dielectric elastomer actuators”. In: *Applied Physics A* 110.2, pp. 281–307.

Ryckaert, Julien et al. (2005). “Ultra-wide-band transmitter for low-power wireless body area networks: design and evaluation”. In: *Circuits and Systems I: Regular Papers, IEEE Transactions on* 52.12, pp. 2515–2525.

Sahinoglu, Zafer, Sinan Gezici, and Ismail Guvenc (2008). “Ultra-wideband positioning systems”. In: *Cambridge, New York*.

Sayson, Jojo V et al. (2013). “Back pain in space and post-flight spine injury: Mechanisms and countermeasure development”. In: *Acta Astronautica* 86, pp. 24–38.

Schoch, Karl F and Howard E Saunders (1992). “Conducting polymers”. In: *Spectrum, IEEE* 29.6, pp. 52–55.

Scilingo, Enzo Pasquale et al. (2003). “Strain-sensing fabrics for wearable kinaesthetic-like systems”. In: *Sensors Journal, IEEE* 3.4, pp. 460–467.

Senesky, Debbie G et al. (2009). “Harsh environment silicon carbide sensors for health and performance monitoring of aerospace systems: A review”. In: *Sensors Journal, IEEE* 9.11, pp. 1472–1478.

Shiga, Tohru and Toshio Kurauchi (1990). “Deformation of polyelectrolyte gels under the influence of electric field”. In: *Journal of Applied Polymer Science* 39.11-12, pp. 2305–2320.

Shishoo, Roshan (2005). *Textiles in sport*. Elsevier.

Shu, Lin et al. (2010). “In-shoe plantar pressure measurement and analysis system based on fabric pressure sensing array”. In: *Information Technology in Biomedicine, IEEE Transactions on* 14.3, pp. 767–775.

Shu, Yi et al. (2015). “A Pressure Sensing System for Heart Rate Monitoring with Polymer-Based Pressure Sensors and an Anti-Interference Post Processing Circuit”. In: *Sensors* 15.2, pp. 3224–3235.

Sippola, Clayton B and Chong H Ahn (2006). “A thick film screen-printed ceramic capacitive pressure microsensor for high temperature applications”. In: *Journal of Micromechanics and Microengineering* 16.5, p. 1086.

Smith, Scott M et al. (2005). "The nutritional status of astronauts is altered after long-term space flight aboard the International Space Station". In: *The Journal of nutrition* 135.3, pp. 437–443.

Smith, Scott M et al. (2012). "Benefits for bone from resistance exercise and nutrition in long-duration spaceflight: evidence from biochemistry and densitometry". In: *Journal of Bone and Mineral Research* 27.9, pp. 1896–1906.

Smith, Scott M et al. (2014). "Men and women in space: bone loss and kidney stone risk after long-duration spaceflight". In: *Journal of Bone and Mineral Research* 29.7, pp. 1639–1645.

Stein, TP (2013). "Weight, muscle and bone loss during space flight: another perspective". In: *European journal of applied physiology* 113.9, pp. 2171–2181.

STELLA. (accessed November 03, 2014). URL: `http://www.stella-project.de/`.

Stenger, Michael B et al. (2010). "Gradient compression garments as a countermeasure to post-spaceflight orthostatic intolerance". In: *Aviation, space, and environmental medicine* 81.9, pp. 883–887.

Stoppa, M, D Demarchi, and M Crepaldi (2015). "Live demonstration: An ultra-low power PFM IR-UWB system for short-range audio streaming". In: *Circuits and Systems (ISCAS), 2015 IEEE International Symposium on*. IEEE, pp. 1896–1896.

Stoppa, M. and P. Freni (2015). *Deformable actuating device with coaxial configuration*. WO Patent App. PCT/IT2015/000,077. URL: `https://www.google.it/patents/WO2015145476A1?cl=en`.

Stoppa, Matteo and Alessandro Chiolerio (2014). "Wearable electronics and smart textiles: a critical review". In: *Sensors* 14.7, pp. 11957–11992.

Styf, Jorma R et al. (1997). "Height Increase, Neuromuscular Function, and Back Pain During 6 Head-Down Tilt With Traction". In: *Aviation Space and Environmental Medicine* 68, pp. 24–29.

Styf, JR, P Kalebo, and AR Hargens (1994). "Lumbar intervertebral disc heights as measured by sonography". In: *Aviat Space Environ Med* 65, p. 450.

Tao, Hu et al. (2012). "Implantable, multifunctional, bioresorbable optics". In: *Proceedings of the National Academy of Sciences* 109.48, pp. 19584–19589.

Taponecco, Lorenzo, AA D'Amico, and Umberto Mengali (2011). "Joint TOA and AOA estimation for UWB localization applications". In: *Wireless Communications, IEEE Transactions on* 10.7, pp. 2207–2217.

Thornton, William E, G Wyckliffe Hoffler, and John A Rummel (1977). "Anthropometric changes and fluid shifts". In:

Ubisense 7000. (accessed October 01, 2015). URL: `http://ubisense.net/en`.

UWB Federal Communications Commission. (accessed June 15 , 2015). URL: https://transition.fcc.gov/Bureaus/Engineering_Technology/Orders/2002/fcc02048.pdf.

Vaganov, Vladimir (2010). "Challenges of complete CMOS/MEMS systems integration". In: *Advanced Materials and Technologies for Micro/Nano-Devices, Sensors and Actuators*. Springer, pp. 17–30.

Van Langenhove, Lieva (2007). *Smart textiles for medicine and healthcare: materials, systems and applications*. Elsevier.

Van Langenhove, Lieva et al. (2007). "Textile sensors for healthcare". In: *Smart Textiles for Medicine and Healthcare: Materials, Systems and Applications. Cambridge and Boca Raton, FL: Woodhead Publishing Limited and CRC Press* 200, pp. 106–122.

Verheyden, Bart et al. (2009). "Adaptation of heart rate and blood pressure to short and long duration space missions". In: *Respiratory physiology & neurobiology* 169, S13–S16.

Vicente, Nadjejda and Carl Walker (2015). "IRISS The'sprint'mission of Andreas Mogensen". In: *ESA BULLETIN-EUROPEAN SPACE AGENCY* 162, pp. 20–31.

Wacker ELASTOSIL. (Accessed October 10 , 2015). URL: http://www.wacker.com/.

Wahab, Yufridin et al. (2008). "Design of MEMS biomedical pressure sensor for gait analysis". In: *Semiconductor Electronics, 2008. ICSE 2008. IEEE International Conference on*. IEEE, pp. 166–169.

Waldie, James M and Dava J Newman (2011). "A gravity loading countermeasure skinsuit". In: *Acta Astronautica* 68.7, pp. 722–730.

Warach, SJ12 et al. (2015). "Assessment of the feasibility of using wearable technology as an innovative tool for telestroke services: Initial results of Google Glass evaluation". In: *INTERNATIONAL JOURNAL OF STROKE*. Vol. 10. WILEY-BLACKWELL 111 RIVER ST, HOBOKEN 07030-5774, NJ USA, pp. 135–135.

Wealthy. (accessed November 03, 2014). URL: http://www.wealthy-ist.com/.

WearIT@Work. (accessed November 03, 2014). URL: http://www.wearitatwork.com/.

West, John B (2000). "Historical perspectives: Physiology in microgravity". In: *Journal of applied Physiology* 89.1, pp. 379–384.

White, Ronald J and Maurice Averner (2001). "Humans in space". In: *Nature* 409.6823, pp. 1115–1118.

Windmiller, Joshua Ray and Joseph Wang (2013). "Wearable electrochemical sensors and biosensors: a review". In: *Electroanalysis* 25.1, pp. 29–46.

Wing, PC et al. (1991). “Back pain and spinal changes in microgravity.” In: *The Orthopedic Clinics of North America* 22.2, pp. 255–262.

Xsens Force Shoes. (accessed June 03 , 2015). URL: `https://www.xsens.com/news/evaluation-xsens-force-shoe-iss/`.

Xu, Jun, Maode Ma, and Choi Look Law (2006). “Position estimation using UWB TDOA measurements”. In: *Ultra-Wideband, The 2006 IEEE 2006 International Conference on*. IEEE, pp. 605–610.

Xu, MG et al. (1993). “Optical in-fibre grating high pressure sensor”. In: *Electronics letters* 29.4, pp. 398–399.

Yang, Depeng et al. (2013). “Compressive sensing based sub-mm accuracy UWB positioning systems: A space–time approach”. In: *Digital Signal Processing* 23.1, pp. 340–354.

Yang, Guang-Zhong and Magdi Yacoub (2006). “Body sensor networks”. In:

Yoneki, Eiko and Jon Crowcroft (2014). “EpiMap: Towards quantifying contact networks for understanding epidemiology in developing countries”. In: *Ad Hoc Networks* 13, pp. 83–93.

Young, KS and S Rajulu (2011). “The effects of microgravity on seated height (Spinal Elongation)”. In:

Young, Laurence R (1999). “Artificial gravity considerations for a Mars exploration mission”. In: *Annals of the New York Academy of Sciences* 871.1, pp. 367–378.

Young, Laurence R et al. (2001). “Artificial gravity: head movements during short-radius centrifugation”. In: *Acta Astronautica* 49.3, pp. 215–226.

Yurish, Sergey Y (2007). “Extension of IEEE 1451 standard to quasi-digital sensors”. In: *Sensors Applications Symposium, 2007. SAS’07. IEEE*. IEEE, pp. 1–6.

Zhang, Honggang et al. (2006). “Multiple signal waveforms adaptation in cognitive ultra-wideband radio evolution”. In: *Selected Areas in Communications, IEEE Journal on* 24.4, pp. 878–884.

Zhou, Min-Xin et al. (2005). “A novel capacitive pressure sensor based on sandwich structures”. In: *Microelectromechanical Systems, Journal of* 14.6, pp. 1272–1282.